Dissertation

MIMO Feeder Links for Very High Throughput Satellite Systems

Thomas Delamotte

der Bundeswehr
Universität München

Faculty of Electrical Engineering and Information Technology
Institute of Information Technology
Chair of Signal Processing

Supervisor and first reviewer	Professor Dr.-Ing. Andreas Knopp, MBA
Second reviewer	Professor Dr. Carlos Mosquera
Third reviewer	Professor Dr.-Ing. Gerhard Bauch

December 2019

UNIVERSITÄT DER BUNDESWEHR MÜNCHEN

MIMO Feeder Links for Very High Throughput Satellite Systems

Thomas Delamotte

Vollständiger Abdruck der von der Fakultät für Elektrotechnik und Informationstechnik der Universität der Bundeswehr München zur Erlangung des akademischen Grades eines

Doktor-Ingenieurs

genehmigten Dissertation.

Promotionsausschuss

Vorsitzender:	Universitätsprofessor Dr.-Ing. Rainer Marquardt
1. Prüfer:	Universitätsprofessor Dr.-Ing. Andreas Knopp, MBA
2. Prüfer:	Professor Dr. Carlos Mosquera
3. Prüfer:	Universitätsprofessor Dr.-Ing. Gerhard Bauch

Die Dissertation wurde am 08.04.2019 bei der Universität der Bundeswehr München eingereicht und durch die Fakultät für Elektrotechnik und Informationstechnik am 02.09.2019 angenommen. Die mündliche Prüfung fand am 19.12.2019 statt.

Abstract

With sum throughputs exceeding 1 Tbit/s, next-generation high throughput satellites will play a key role in integrated satellite-terrestrial 5G networks for applications including backhauling or broadband internet access in rural areas, planes and vessels. Such satellites require the deployment of tens of Ka- and/or Q/V-band feeder links to provide enough uplink bandwidth. Meanwhile, geographical restrictions as well as cost and quality-of-service considerations significantly constrain the search for gateway deployment sites. Diversity strategies are also necessary to cope with strong rain fades. In this thesis, multiple-input-multiple-output (MIMO) feeder links are proposed to address these challenges. Using two active gateway antennas per feeder link, a MIMO-based solution enables to support twice the data traffic per feeder link compared to the state-of-the-art. The optimization of the backbone network design and the interference isolation between the different links can easily be achieved thanks to a reduction of the number of gateway sites. Moreover, a better robustness against adverse weather conditions can be guaranteed. On-ground and on-board processing strategies for such MIMO links are introduced to enable the reliable spatial multiplexing of different data streams. Furthermore, advanced smart diversity schemes are presented to guarantee a sufficient system availability. A thorough analysis in terms of achievable uplink carrier to interference plus noise ratio (CINR) emphasizes the advantages of the proposed concept and provides guidelines for an efficient design.

Supervisor: Professor Dr.-Ing. Andreas Knopp, MBA

Kurzfassung

Geostationäre Satellitensysteme mit einem Datendurchsatz von über einem Terrabit pro Sekunde werden in zukünftigen 5G-Netzen eine wesentliche Rolle spielen. So sollen breitbandige Internet-Zugänge für entlegene Gebiete, Flugzeuge und Schiffe als auch Anwendungen wie Backhauling unterstützt werden. Durch die Satelliten soll die begrenzte Reichweite terrestrischer 5G-Netze kompensiert werden. Solche Satellitensysteme benötigen hierfür eine große Anzahl von Ka- und/oder Q/V-Band Feeder Links, um eine ausreichende Bandbreite im Uplink zu gewährleisten. Geographische Beschränkungen sowie Kosten- und QoS-Betrachtungen grenzen die Suche nach Bodenstationsstandorten ein. Außerdem sind Diversitätsverfahren nötig, damit eine starke Regendämpfung kompensiert werden kann und es zu keinem Verbindungsabbruch kommt. Der in dieser Arbeit vorgeschlagene Ansatz löst die aufgeführten Herausforderungen mit einer sogenannten Multiplen-Input-Multiplen-Output (MIMO) Feeder Links Strategie. Die Verwendung von zwei aktiven Bodenstationen pro Feeder Link ermöglicht eine Verdoppelung der Datenrate im Vergleich zum Stand der Technik. Die daraus resultierende Reduzierung der Anzahl von weit entfernten Bodenstationsstandorten vereinfacht die Optimierung des Backbone-Netzwerkes und ermöglicht die Vermeidung von Interferenzen. Eine erhöhte Robustheit gegen schlechte Wetterbedingungen kann hierdurch ebenfalls erzielt werden. On-ground und on-board Signalverarbeitungslösungen für die vorgeschlagenen MIMO Links werden in dieser Arbeit eingeführt, um ein zuverlässiges Raummultiplexing von unabhängigen Datenströmen zu ermöglichen. Zudem werden fortgeschrittene Diversitätsverfahren entwickelt, sodass eine ausreichende Systemverfügbarkeit garantiert werden kann. Eine ausführliche Analyse hinsichtlich des erreichbaren Uplink Carrier to Interference plus Noise Ratio (CINR) veranschaulicht die Vorteile des vorgeschlagenen Konzeptes und liefert einen Leitfaden für ein effizientes Systemdesign.

Betreuer: Universitätsprofessor Dr.-Ing. Andreas Knopp, MBA

Acknowledgments

A doctoral thesis is not only the fruit of several years research work of a single scientist. Preparing this manuscript and defending it successfully would not have been possible without the support of all those who have accompanied me in one way or another to the doctor title. Now the time has come for me to thank them all.

First, I am greatly indebted to my PhD supervisor, Prof. Dr.-Ing. Andreas Knopp, who did everything to encourage my scientific career. The chance he gave me to broaden and deepen my skills, his careful reviews of my work, his advices have definitely been of a great value. Andreas, thank you. I am also very grateful to my colleagues for the wonderful working atmosphere. Robert, Christian, you were there from the beginning, and your doors were always open for scientific discussions. Your fruitful suggestions have helped me to go the right way. Kai-Uwe, I would not have understood the practical constraints in MIMO satellite systems so good without you. I owe you a lot! Tony, the space enthusiast, it was a great pleasure to have these fascinating conversations with you. Inquiring into the past, the present and the future of space exploration and the aerospace industry have kept my motivation high. Doing research in the domain of satellite communications and contributing to some extent to the development of technologies that will further foster innovation in space is a real privilege. Finally, I would like to thank Florian for his remarkable involvement in the scientific life of our institute. I will of course not forget the valuable help of Constanze, Mr. Dochtermann and the "Wolfgangs" while solving the numerous administrative and technical issues that have popped up on my way.

This work would have obviously not be the same without the continuous support of my family. Who would I actually be without my parents, Anne and José, who raised me with all the love a child can dream about? My grand-father, André, also played a major role in the development of the scientist I became. Thank you and rest in peace, pépé. I would have not achieved so much either without the unconditional support of my beloved wife, Luba, and my lovely son, Antoine, especially during the painstaking writing process of this thesis. I am not exaggerating, my life with

them is a dream. I should also deeply thank my sister, Florence, her partner, René, and my three nephews, Alice, Baptiste and Amélie, for all these nice moments we spent together when I came back to France in order to relax for a few days. The acknowledgments to my family would of course be only half complete if I would not warmly thank Irina, Petko, Niki, Lubo and baba Niki for always making me feel like a full family member even though I am still not able to speak Bulgarian.

Let me now come to the last very important pillar of a successful PhD: the friends. This PhD time would not have been so enjoyable without innumerable moments of joy and laughter with my friends. Be it traveling together abroad, hiking in the Alps, sharing a beer in a *Biergarten* or playing theater, all these activities have been for me a perfect way to take a breath. Arnaud, you deserve here a special thank since you are by far the one with whom I spent most of this free time. Delphine, Céline, Gregor, Mathieu, Anne-Laure, Uli, Eva, Antoine, Lisa, Sandrine, Caroline, Julia, I will also never forget these precious moments together. I will finish with a dedication to the french improv group, *les Bavards Rois*. Mouton, 3T, La Mite, Gouin Gouin, Snark, Guelu, Souris, Coco l'Asticot, La Loutre, Mariole...my life in Munich would not have had the same taste without our *improvised* trainings and shows.

Let me conclude these acknowledgments by thanking Prof. Dr.-Ing. Rainer Marquardt, the chairman of the doctoral board, as well as Prof. Dr. Carlos Mosquera (University of Vigo) and Prof. Dr.-Ing. Gerhard Bauch (Hamburg University of Technology), my second and third examiner, respectively. It has been a great honor for me to defend my work in your presence!

Thank you very much to all of you!

Thomas Delamotte,

Munich, May 2020

Contents

List of Figures

List of Tables

Acronyms

CDF cumulative distributive function

CINR carrier to interference plus noise ratio

CIR carrier to interference ratio

CSI channel state information

DFT discrete Fourier transform

DSP digital signal processor

DVB-S Digital Video Broadcasting - Satellite

DVB-S2 DVB-S second generation

DVB-S2X DVB-S2 extensions

ECEF Earth centered, Earth fixed

ECI Earth centered inertial

EIRP effective isotropic radiated power

ESA European Space Agency

GEO geostationary earth orbit

Ground-P ground-limited processing

HTS high throughput satellite

ISI inter-symbol interference

Joint-P joint ground/on-board processing

LHCP left-handed circular polarization

LOS line-of-sight

MIMO multiple-input-multiple-output

MSE mean squared error

MU-MIMO multiuser MIMO

NASA National Aeronautics and Space Administration

QoS quality-of-service

RF radio frequency

RHCP right-handed circular polarization

SISO single-input-single-output

SWM spherical wave model

UCA uniform circular array

ULA uniform linear array

V/HTS very high throughput satellite

ZF zero-forcing

Nomenclature

Operators

$|\cdot|$ Absolute value of a scalar

$\det(\cdot)$ Determinant of a square matrix

$\mathrm{diag}(\cdot)$ Block diagonal matrix whose diagonal entries are the operator inputs

$\mathbb{E}[.]$ Expected value of a random variable

$\|\cdot\|_{\mathrm{F}}$ Frobenius norm of a matrix

$(\cdot)^{\mathrm{H}}$ Matrix hermitian transpose

$(.)^{+}$ Moore-Penrose pseudoinverse of a matrix

$P(.)$ Probability distribution of a random variable

$\mathrm{Re}(\cdot)$ real part of a complex number

$(\cdot)^{\mathrm{T}}$ Matrix transpose

$\mathrm{tr}(\cdot)$ Trace of a square matrix

Symbols

a Orbital semimajor axis

$\alpha_n^{\nu}(t)$ Time-varying amplitude fading due to the tropospheric propagation of the signal transmitted by the n-th antenna in the ν-th MIMO feeder link

$A_n^{\nu}(t)$ Time-varying attenuation due to the tropospheric propagation of the signal transmitted by the n-th antenna in the ν-th MIMO feeder link

$\beta^{\nu}_{\mathrm{R},n}(t)$ Extra delay of the signal from the n-th gateway antenna in the ν-th MIMO feeder link due to the tropospheric refraction

$b^{\nu'\nu}_{n}$ Normalized receive antenna gain for the signal transmitted by the n-th antenna in the ν-th MIMO feeder link when detected by the feeds allocated to the ν'-th link

$\mathbf{B}^{\nu}$ $K \times K$ precoding matrix for the ν-th MIMO feeder link

B Bandwidth per user beam

$\mathbb{C}$ Set of complex numbers

c^{ν}_{A} Correlation of the rain attenuations in the ν-th MIMO feeder link

c_0 Speed of light in free-space

c^{ν}_{R} Correlation of the rain events in the ν-th MIMO feeder link

$d^{\nu}_{n}(t)$ Baseband signal transmitted from the n-th gateway antenna in the ν-th feeder link

d^{ν}_{E} Distance between the gateway antennas of the ν-th MIMO feeder link

$\delta^{\nu}_{\mathrm{E}}$ Orientation of the gateway antenna array in the ν-th MIMO feeder link

$\Delta t^{\nu}_{\mathrm{D}}$ Differential propagation delay in the ν-th MIMO feeder link

Δ_{a} Diameter of the circular aperture

$\tilde{d}^{\nu}_{n}(t)$ Passband signal transmitted from the n-th gateway antenna in the ν-th feeder link

D Mean longitude drift rate

$\Delta r^{\nu}(t;\Delta t)$ Differential variation of the path lengths in the ν-th MIMO feeder link between time instants t and $t+\Delta t$

d_{S} Distance between the satellite antennas

e Orbital eccentricity

$\mathbf{e}_k$ $K \times 1$ vector containing only zeros except for its k-th entry which is equal to one

$f_{\mathrm{c},l}$ Carrier frequency of the l-th frequency channel

ϕ^{ν}_{E} Latitude of the center of the gateway antenna array for the ν-th MIMO feeder link

$\phi_{\mathrm{S}}(t)$ Latitude of the center of the satellite antenna array

g_e Maximum antenna gains and losses due to imperfections of the front-ends

$h_{mn}^{\nu'\nu}(t)$ Time-varying baseband channel coefficient between the n-th antenna in the ν-th MIMO feeder link and the feed allocated to the ν'-th MIMO feeder link on the m-th satellite antenna

$\mathbf{H}_l^{\nu'\nu}$ 2×2 MIMO channel matrix at the l-th uplink frequency between the gateway antennas of the ν-th MIMO feeder link and the satellite antenna feeds allocated to the ν'-th MIMO feeder link

$\bar{\mathbf{H}}^{\nu'\nu}$ $K \times K$ block diagonal MIMO channel matrix between the gateway antennas of the ν-th MIMO feeder link and the satellite antenna feeds allocated to the ν'-th MIMO feeder link

$\mathbf{h}_n^{\nu\nu}$ n-th column of the MIMO channel matrix $\mathbf{H}^{\nu\nu}$

$\tilde{h}_{mn}^{\nu'\nu}(t)$ Time-varying passband channel coefficient between the n-th antenna in the ν-th MIMO feeder link and the feed allocated to the ν'-th MIMO feeder link on the m-th satellite antenna

$\mathbf{I}_N$ $N \times N$ identity matrix

i Orbital inclination

k Index of the considered data stream

K Number of supported user beams per feeder link and polarization state

l Index of the considered frequency channel

L Number of frequency channels per feeder link

N Number of active feeder links

ν Index of the considered MIMO feeder link

$\boldsymbol{\eta}_\mathrm{I}^\nu$ Vector of interference noise in the ν-th MIMO feeder link

$\boldsymbol{\eta}_\mathrm{T}^\nu$ Vector of thermal noise in the ν-th MIMO feeder link

ω Argument of perigee

$\boldsymbol{\Omega}$ $K \times K$ DFT matrix

Ω Right ascension of the ascending node

$\mathbf{p}_{\mathrm{E},n}^\nu$ Earth-centered Earth-fixed coordinates vector of the n-th gateway antenna in the ν-th MIMO feeder link

$p_{\mathrm{o},p}^{\nu}$ Outage probability of the p-th virtual transmitter in the ν-th feeder link

$P_{\mathrm{I},l}^{\nu}$ Interference noise power in the l-th frequency channel of the ν-th MIMO feeder link

$P_{\mathrm{T},l}^{\nu}$ Thermal noise power in the l-th frequency channel of the ν-th MIMO feeder link

$P_{\mathrm{u},l}^{\nu}$ Maximum transmit power per gateway antenna in the l-th frequency channel of the ν-th MIMO feeder link

P Number of redundant feeder links

$\mathbf{p}_{\mathrm{S},m}(t)$ Earth-centered Earth-fixed coordinates vector of the m-th satellite antenna

ψ Angular velocity of the Earth

$p(t)$ Nyquist pulse shaping filter

$\mathbf{q}_{mn}^{\nu}(t)$ Vector pointing from the n-th gateway antenna in the ν-th MIMO feeder link to the m-th satellite antenna

Q Number of virtual transmitters in outage

$\mathbf{R}_{\mathbf{v}}$ Autocorrelation matrix of vector $\mathbf{v}$

$\rho_{\mathrm{u},k}^{\nu}$ Post-processing carrier to interference plus noise ratio for the k-th data stream in the ν-th feeder link

R_{E} Mean Earth radius

$\mathbb{R}$ Set of real numbers

$\mathbb{R}_{\geq 0}$ Set of non-negative real numbers

$R_{\mathrm{S}}(t)$ Distance from the Earth's center to the satellite reference point in the equatorial plane

$r_{mn}^{\nu}(t)$ Distance between the n-th gateway antenna in the ν-th MIMO feeder link and the m-th satellite antenna

$s(t)$ Sidereal angle

$\mathbf{s}^{\nu}$ Vector of transmit symbols in the ν-th MIMO feeder link

$\theta_{\mathrm{E}}^{\nu}$ Longitude of the center of the gateway antenna array for the ν-th MIMO feeder link

T_{e} Edge taper

$\theta_{\mathrm{S}}(t)$ Longitude of the center of the satellite antenna array

T_{symb} Symbol duration

$\mathbf{v}_{\mathrm{S}}(t)$ Velocity vector of the satellite relative to the rotating Earth

$\mathbf{V}^{\nu}$ $K \times K$ block diagonal matrix containing the eigenvectors of $\left(\bar{\mathbf{H}}^{\nu\nu}\right)^{\mathrm{H}} \bar{\mathbf{H}}^{\nu\nu}$

W_{u} Uplink bandwidth per polarization state

$\mathbf{W}^{\nu}$ $K \times K$ on-board processing matrix for the ν-th MIMO feeder link

$\mathbf{y}^{\nu}$ Vector of receive symbols in the ν-th MIMO feeder link

$\mathbf{0}_N$ $N \times N$ zero matrix

$\mathbf{z}^{\nu}$ Vector of symbols at the output of the on-board processor for the ν-th MIMO feeder link

Chapter 1

Introduction

This chapter starts with a brief history of satellite communications. The current trend in the satellite industry that consists in deploying multibeam geostationary satellites to provide broadband services is also discussed. A particular focus is set on the engineering challenges associated to the design of feeder links for such satellite systems. Based on the weaknesses of the current solutions, the advantages of the multiple-input-multiple-output (MIMO)-based feeder link architecture proposed in this thesis are shortly emphasized. The state-of-the-art of MIMO line-of-sight (LOS), the concept on which MIMO feeder links are based, is then presented. The structure of the presented work is finally outlined.

1.1 The Development of Satellite Communications

Even though launching man-made communication relays into orbit was already envisioned before 1945 [1], the formalization of this idea is attributed to Arthur C. Clarke. He published in October 1945 a paper entitled *Extra-Terrestrial Relays: Can Rocket Stations Give World Wide Radio Coverage?* [2]. In this work, he underlined the interest of the geostationary orbit, 35 870 km above the Earth surface, to achieve a worldwide coverage with only three satellites. However, Clarke thought that his concept could only be realized in a very long-term perspective. He thus didn't patent his idea [3]. The decades that followed proved him wrong. The satellite communications

industry became profitable within 20 years.

The era of satellite communications began on 4 October 1957 with the launch of the first artificial satellite *Sputnik* by the Soviet Union. This event appears as one of the most important milestones in the space race that opposed at that time the United States of America (USA) to the Soviet Union. This space competition, together with scientific advances inherited from the Second World War, triggered a tremendous development of the satellite technology and revolutionized global communications. The *Sputnik* satellite was only able to send a pulse signal back to Earth but it demonstrated that using an artificial satellite to broadcast signals from space was technically feasible. A year later, on 18 December 1958, the satellite *SCORE* (Signal Communications by Orbiting Relay Equipment) was launched by the USA and was the first satellite to broadcast an audio message from space. The first test satellite allowing two-way live communications was launched on 12 August 1960 and was denominated *Echo 1*. This satellite was actually a passive reflector which simply echoed back the uplink signal to Earth. A second test satellite, called *Echo 2*, was also launched on 25 January 1964. Even though the passive reflection of signals was successfully tested with both *Echo 1* and *Echo 2*, this solution was not retained due to the low achievable capacity [3]. On 4 October 1960, the first active repeater satellite, the *Courier 1B*, was put into orbit. It used a store-and-forward transmission architecture and could only reach a transmission rate of 55 kbit/s [4]. A further step was reached when the *Telstar* (Atlantic communications) and *Relay 1* (Pacific communications) satellites, launched by the National Aeronautics and Space Administration (NASA) [3] on 10 July 1962 and 22 November 1963, enabled for the first time a direct relaying of signals between continents.

All the satellites used for experimentation from 1957 to 1963 were put into low Earth orbits ($\approx$ 200 km–2000 km). It was on 19 August 1964 that the first geostationary earth orbit (GEO) communication satellite, the *Syncom 3*, was successfully launched. This represents a milestone in the history of commercial worldwide communications. Following this conclusive experimentation, the era of commercial satellite communications indeed started with the launch on 6 April 1965 of the first satel-

lite of the Intelsat series, *Intelsat 1*, nicknamed *Early Bird*. It provided transatlantic telecommunications services and was rapidly followed by more powerful satellites (*Intelsat 2, 3*, etc...) which offered significantly higher capacity than submarine cables at that time [3], [5]. However, due to their low gain antennas and low transmit power, these satellites required large antennas ($\approx 30\,\mathrm{m}$ diameter) on Earth to detect the extremely weak signals. In the very first years of satellite communications, only point-to-point intercontinental communications were possible. Meanwhile, the rapid technological evolution enabled the satellite industry to extend its consumer base [1], [6]. In 1972, the first domestic system using a geostationary satellite, known as *Anik A1*, was for example deployed in Canada. With point-to-multipoint communications, satellites brought significant advantages compared to terrestrial networks especially in regions where geographical constraints and/or low population density make terrestrial solutions too expensive. Moreover, whereas satellites of the first generation were operated in the C-band (4–8 GHz) and used frequency modulation, the introduction of new frequency bands (X-band: 8–12 GHz/Ku-band: 12-18 GHz) and the advent of digital communications allowed a further increase of the supported data rates. In the 80s, satellite communications services included the distribution of TV programs, teleconferencing or maritime communications. The demand for even higher data rates kept increasing since then.

Nowadays, a large number of satellite communications systems use the Digital Video Broadcasting (DVB) open standards. The first release, the DVB-S standard, was published in 1995. It was followed, ten years later, by the DVB-S2 standard. An extension of this latter standard, known as DVB-S2X, was released in March 2014. Through the use of powerful channel coding, higher-order constellations and reduced roll-off factors for the pulse shaping, an efficient exploitation of the limited spectral resources is enabled. Satellite technology is now part of our everyday life, and the world satellite industry generates an annual revenue of more than $250 billion [7]. While the broadcasting of data on large regions of Earth (country or continent) has long been one of the main drivers for the development of satellite communications, the delivery of broadband services has become a promising market in the last decade.

Such services are enabled by multibeam satellites, known as high throughput satellites (HTSs), where frequency resources are reused. In this way, the sum throughput is significantly increased, and the cost per bit is further reduced to offer a competitive alternative to terrestrial networks for the delivery of services with high data rate requirements. In the following section, the architecture and the design challenges of next-generation HTS systems are discussed.

1.2 The Advent of High Throughput Satellites

Contrary to conventional satellites used for signal broadcasting on vast areas of the Earth (country or continent), HTSs use a large number of spot beams where frequency resources are reused. The technological advances in the design of Ka-band multifeed antennas with large apertures have especially favored the development of this new generation of satellites. The typical architecture of a HTS system is illustrated in Fig. 1-1. Nowadays, half power beamwidths[1] as low as 0.2° are envisioned

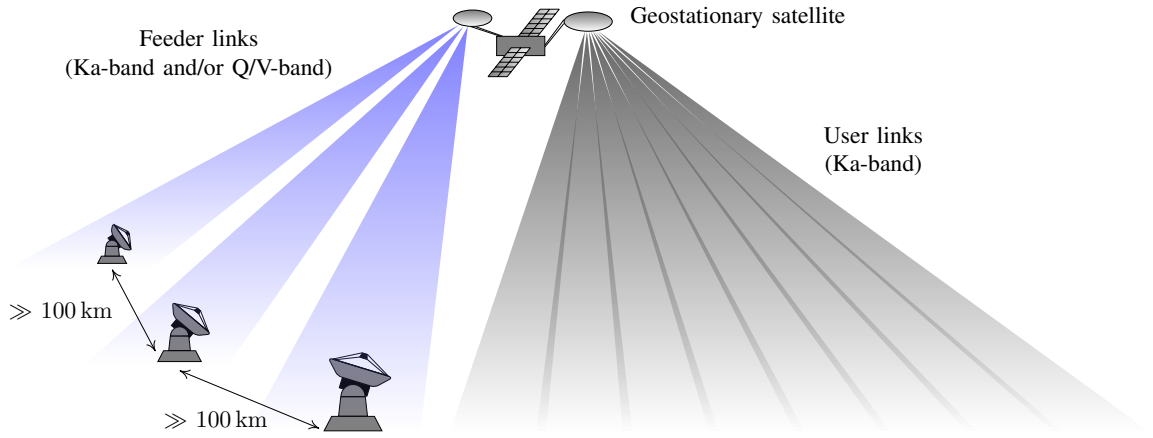

Figure 1-1: Typical architecture of a HTS system

for user links in the Ka-band (20/30 GHz) [8], [9]. This results in a beam diameter[2] of less than 150 km. As a consequence, power can be concentrated on very localized regions, and hundreds of spot beams can be deployed on a continent like Europe. A

[1] In antenna theory, the half power beamwidth characterizes the region of the radiation pattern for which the transmit power does not fall to more than half its maximum value.

[2] The beam diameter is the diameter of the satellite antenna footprint.

few examples of HTSs that have been launched since 2005 are provided in Table 1.1. The general trend towards the increase of the number of spot beams and, thus, of the

Table 1.1: Non-exhaustive list of high throughput satellites

Name	*Launch year*	*Coverage*	*Spot beams*	*Throughput*
Thaicom 4 (iPSTAR)	2005	Asia, India, Australia	87 Ku-band / 10 Ka-band	45 Gbit/s
KA-SAT	2010	Europe, North Africa, Middle East	82 Ka-band	90 Gbit/s
Viasat 1	2011	North America	72 Ka-band	140 Gbit/s
Jupiter 1 (Echostar XVII)	2012	North America	60 Ka-band	120 Gbit/s
Jupiter 2 (Echostar XIX)	2016	North America	120 Ka-band	220 Gbit/s
Viasat 3 Americas	Planned for 2019	North, Central and South America	+1000 Ka-band	1 Tbit/s
Konnect VHTS	Planned for 2021	Europe	+200 Ka-band	500 Gbit/s

achievable sum throughput per satellite is clearly observable. With capacities of up to 1 Tbit/s, future HTSs are commonly called very high throughput satellites (V/HTSs). Following the progress of radiation-hardened electronics, most of these satellites will embark a digital processor. In this way, the beam, power and frequency resources can be flexibly allocated according to the traffic demands [10]. V/HTS systems will play an important role in integrated satellite-terrestrial networks to extend the range of applications supported by 5G, which is the latest standard for mobile communications specified by the Third Generation Partnership Project (3GPP). Backhauling or broadband internet access in planes, vessels and remote locations without fiber connection belong to some of the most promising enhanced mobile broadband (eMBB) use cases for satellites [11].

A key technological evolution to cope with the ever growing demand for higher data rates in bandwidth-limited V/HTS systems is to shift their feeder links to the Q/V-band (40/50 GHz). This especially enables to free up the whole Ka-band spectrum for the user links. Even though up to 5 GHz of bandwidth is available in the Q/V-band, tens of spatially separated feeder links with a full re-use of the uplink frequency resources are required to support the aggregated user link bandwidth. An example of system dimensioning is provided in Table 1.2. The case of a transparent payload is considered i.e., that the signals are simply converted to the downlink frequency and amplified before their transmission in the downlink[3]. As illustrated in

[3]If a digital on-board processor is available, a sample-based processing of the signals such as digital filtering can also be performed. The payload is in this case a *digital transparent payload*. The interest of such payloads will be discussed in Chapter 2.

Table 1.2: Example of V/HTS system dimensioning

	User links	***Feeder links***
Payload characteristics	Transparent payload and single feed per beam (SFPB)	
Bandwidth per beam	1.45 GHz in Ka-band	4 GHz in Q/V-band
Polarizations per beam	1	2
Spatially separated beams	275	50

Fig. 1-1, a separation of several hundreds of kilometers must be ensured between the ground equipment of each feeder link to guarantee a sufficient beam isolation. The search for tens of gateway deployment sites fulfilling this constraint in a given region of Earth (e.g., Western Europe) is actually a challenging engineering problem, and the costs of the ground segment represent a non-negligible part of the total costs of a V/HTS system. The following issues have indeed to be considered:

Backbone architecture: The costs of a network of ground stations seamlessly integrated into the terrestrial 5G broadband access architecture are influenced by the length of the peering links and the distance to the internet service provider points of presence [11], [12]. Moreover, the gateways locations influence the quality-of-service (QoS) of data delivery from the terrestrial network. To guarantee certain latency and/or reliability requirements, the geographical location of the ground stations should be carefully optimized [13].

Regulatory coordination: The use of frequency bands requires a complex coordination among governments around the world. The aim is to keep interference between different systems operated in the same radio-frequency spectrum below a specific limit. These harmonization efforts are conducted by the International Telecommunications Union (ITU) [14]. In order to comply with the ITU rules, satellite operators might for example be constrained to avoid the installation of gateways in certain countries.

Tropospheric impairments: Tropospheric impairments, including especially rain, can significantly impact the availability of links in higher frequency bands like the Ka- or the Q/V-band. As a consequence, an operator will privilege the

deployment of gateways in regions where the probability of experiencing severe impairments is lower. To further improve the system availability, smart diversity strategies are also required [15], [16].

To partly address the two first challenges, new candidate technologies like the resort to W-band (81–86 GHz) [17] or optical links [18] are considered for future systems. Due to the larger available bandwidth, the number of gateway sites can be drastically reduced compared to an architecture limited to Ka- and/or Q/V-band feeder links. However, the tropospheric impairments become an ever more challenging issue in terms of link availability. In particular, optical links are in outage as soon as clouds are present on the signal propagation path, and optical ground stations can only be installed in regions with a low probability of cloud coverage (e.g. Southern Europe, Africa). Moreover, advanced diversity strategies are necessary which influences the system costs. Finally, the ground and space hardware for W-band and optical links is less mature. As a consequence, an innovative architecture for the feeder links of V/HTS systems is presented in this doctoral thesis. This new design, which is based on the MIMO LOS concept, enables satellite operators to handle the feeder link bottleneck with existing Ka- and/or Q/V-band hardware products. The state-of-the-art of the MIMO LOS technology is presented in the following.

1.3 MIMO LOS: A State-of-the-Art

In this section, a short survey about the pioneering investigations on MIMO systems is provided. The state-of-the-art of MIMO LOS for terrestrial and satellite application scenarios is then thoroughly reviewed, and a basic example for the optimization of a single-satellite MIMO LOS system is considered. To clearly demarcate the proposed MIMO LOS strategy from other MIMO over satellite schemes, the literature of this field of research is also briefly discussed.

1.3.1 Background

A MIMO communication system use several antennas at the transmitter and at the receiver. If T transmit and R receive antennas are deployed, a $R \times T$ MIMO link is obtained. At the end of the nineties, the very first investigations on the capacity of such systems were conducted using independent and identically distributed Gaussian random variables to model the channel coefficients between each transmit and receive antenna [19], [20]. Such an assumption corresponds to a Rayleigh fading channel model. It is appropriate to represent propagation channels with a rich scattering environment. On the other hand, the independence of the channel coefficients is considered as valid as long as the separation of the array elements is larger than the half-wavelength. In this case, a linear scaling of the link capacity with the minimum of the number of inputs and outputs is obtained. This significant capacity gain, known as spatial multiplexing gain, is enabled by the exploitation of independent spatial paths. The space dimension is thus a new degree of freedom in addition to time, frequency and polarization. Rich multipath environments are for example observed in urban cellular networks where signals are reflected by numerous scatterers such as buildings. As a consequence, the MIMO technology is nowadays a key enabler to reach high data rates with terrestrial communication standards like LTE-advanced [21] or the new 5G [22]. However, the Rayleigh fading model assumption for which MIMO gains were first predicted is not accurate to represent channels with LOS propagation. Research works were hence conducted to comprehensively analyze MIMO LOS channels as reported in the sequel.

1.3.2 MIMO LOS for Terrestrial Communications

If strong LOS components are present in the propagation channel, the capacity of MIMO systems becomes strongly influenced by the geometrical arrangement of the antennas. The positioning of the antennas indeed influences the phase of the channel coefficients in a LOS environment. Using a ray-tracing approach, it was shown in 1999 that antenna configurations can be found to achieve maximum capacity [23].

This work was followed by further studies which analyze the feasibility of MIMO LOS for indoor wireless local area networks [24]–[26] and outdoor broadband wireless applications [27], [28]. Relying on a 3-D geometrical model, general design rules were formulated in [29], [30] to optimize the inter-element spacings if uniform linear arrays (ULAs) are used on both sides of the MIMO link. The optimal antenna arrangement depends on the distance between the arrays, their spatial orientation and the carrier frequency. Channel measurements in indoor [30]–[34] and outdoor scenarios [35] at carrier frequencies around 2.5 GHz or 5.5 GHz confirmed the theoretical predictions. All the previously mentioned works on MIMO LOS adopted a spherical wave model (SWM) instead of the more common plane wave model (PWM) to represent the propagation channel between the antenna arrays. The importance of the SWM to model MIMO LOS channels was extensively discussed in [36].

Whereas the concept of MIMO LOS was originally studied for terrestrial networks, the channel measurements from [30]–[35] revealed, however, that a pure LOS channel is never fully obtained due to the presence of a few scatterers. Moreover, most of terrestrial communication scenarios envisioned a communication link between an access point and a mobile terminal. Designing the system under the assumption of a static antenna arrangement is then not practical. The very first application of MIMO in a pure and fixed LOS propagation environment was actually proposed in 2008 for satellite communication systems. Research works on MIMO LOS over satellite are addressed in the following section. Interestingly enough, MIMO LOS was later investigated for high-throughput millimeter wave backhaul links in terrestrial 5G networks [37]. In this case, the use of a 60 GHz carrier frequency and the static position of the front-ends also offer the desired propagation conditions.

1.3.3 MIMO LOS over Satellite

The first works on MIMO LOS over satellite [38], [39] focused on satellite services with frequency bands above 10 GHz. At these higher frequencies, links to geostationary satellites indeed use highly directional antennas [6], [40] such that strong LOS connections are established. Therefore, a capacity-optimum MIMO satellite channel can

be obtained by an appropriate positioning of the transmit and receive antennas. The basic architecture of a 2×2 MIMO LOS system with a single satellite is for example illustrated in Fig. 1-2. In the original works, an arbitrary number of elements arranged

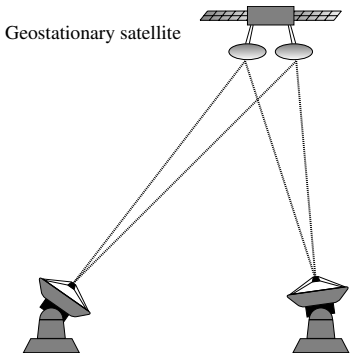

Figure 1-2: 2×2 MIMO LOS satellite system with a single satellite

as a ULA on Earth and two antennas on the geostationary orbit were considered. The antennas in space were installed either on the same satellite (single-satellite scenario) as already shown in Fig. 1-2 or on different satellites with an angular separation of a few degrees (dual-satellite scenario). The position of the antenna elements on ground were fully characterized by the coordinates of the array center, its orientation (e.g. East-West direction) and the inter-antenna spacing. On the other hand, the antennas in space were assumed to be in the equatorial plane, and their locations were defined by their longitude. Based on this description, a closed-form expression for the optimal antenna separation on Earth was derived for the case where the other parameters are known. The validity of this result was verified through numerical simulations. With a single satellite, an antenna separation of several kilometers on Earth is required to achieve maximum capacity. Conversely, the ground antennas must only be separated by a few tens of centimeters in the dual-satellite scenario. The Earth antenna array can in this case be installed on a moving platform like a plane or a car. Antenna designs were thus introduced in [38] to guarantee a high channel capacity for MIMO satellite links with a mobile Earth antenna array. In [41], the analytical analysis of this mobile scenario was extended to uniform circular arrays (UCAs) and carrier frequencies below 10 GHz[4].

[4]The L-band (1–2 GHz) or the S-band (2–4 GHz) are generally used for mobile satellite services.

The preliminary investigations on the feasibility of MIMO LOS over satellite also concentrated on the robustness of the links against phase and/or amplitude impairments due to station-keeping maneuvers [39], [42] or atmospheric degradations [43], [44]. A theoretical analysis especially showed that the capacity of a MIMO satellite link is not impacted by a phase impairment common to all propagation paths originating from a given antenna. Using interferometric measurements, this property was later proven to be accurately verified for a dual-satellite scenario which is the most sensitive setup to phase perturbations in the atmosphere [45]–[47]. In [48], [49], a frequency domain equalization (FDE) was proposed to mitigate at the receiver the inter-symbol interference (ISI) caused by path delay differences. Moreover, the performance degradations entailed by the presence of nonlinear power amplifiers in a system with MIMO pre-processing was assessed in [50], [51], and it was shown that MIMO strategies are still practically viable in this context.

All the theoretical studies on MIMO LOS over satellite relied on a SWM which, as already mentioned in the previous section, is more appropriate to model the physical propagation channel in a LOS environment. Its accuracy was confirmed in 2016 with a proof-of-concept setup in which the access to two geostationary satellites from Eutelsat enabled to build a Ku-band MIMO channel [52]. Other measurement results were also reported in [53]. A perfect agreement between the channel measurements and the theoretical model was every time obtained, and the design rules first formulated in [38], [39] were hence validated.

Based on the results obtained since 2008, the MIMO LOS technology for satellite communications has especially been investigated for the following use cases:

Secure communications: The antenna geometry required for a high capacity MIMO link can be exploited to secure data transmission [54]. Using an information-theoretic framework, the system can be designed such that an eavesdropper located outside an authorized area is unable to retrieve data.

UHF military communications: In [55], two geostationary satellites separated by tens of degrees and operating in the ultra high frequency (UHF) band were con-

sidered to transmit data to an array with non-directional antennas on a mobile terminal (e.g. rooftop of a military vehicle). The MIMO channel was modeled in this case with a Ricean flat fading to take the presence of multipath components into account. Even though a pure LOS propagation environment is not obtained here, the impact of the antenna geometry on the system capacity was emphasized. Channel measurements presented in [56] confirmed these conclusions, and highlighted again the advantage of UCAs to achieve high capacity in mobile scenarios.

Multibeam downlink: In [57], the multireflector architecture of typical satellite payloads motivated the application of the MIMO LOS concept in the multibeam downlink of a HTS system with full frequency reuse. A user scheduling algorithm, known as *multiple antenna downlink orthogonal clustering* (MADOC), was especially proposed to build groups of users served in common time-frequency resource blocks. Moreover, MIMO pre-processing was introduced to mitigate spatial interference and ensure throughput fairness between the users.

Feeder links: The design of MIMO feeder links for V/HTS systems is going to be thoroughly discussed in this work. As already underlined in Section 1.2, this innovative feeder link architecture enables to tackle challenges encountered in the conception of the ground segment of next-generation satellite systems.

1.3.4 Example: Optimized 2×2 Single-Satellite System

The structure of MIMO feeder links that will be introduced in Chapter 2 must respect the design rules formulated in [38], [39]. Hence, an example for the antenna geometry optimization of a 2×2 MIMO system with a single satellite is provided in Table 1.3 to get a first insight into the basic design trade-offs. A separation of 3 m between the satellite antennas is assumed. Moreover, the considered satellite longitude of 9° E corresponds to an orbital position that enables an efficient coverage of Europe (e.g. KA-SAT). This orbital slot will be used for all the results presented in this thesis. In this example, the optimal Earth antenna separations were determined for an array

Table 1.3: Optimization example of a single-satellite 2×2 MIMO system

Satellite orbital position	9° E			
Satellite antenna separation	3 m			
Center of the Earth antenna array	Luxembourg City (49.61° N, 6.13° E)			
Orientation of the arrays	East-West direction			
Carrier to noise ratio (CNR) per path	20 dB			
Carrier frequency	20 GHz	30 GHz	40 GHz	50 GHz
Min. Earth antenna separation for max. capacity	96 km	64 km	48 km	38.4 km
Tolerance region for a capacity loss $\leq 5\,\%$	$\pm$42.8 km	$\pm$28.5 km	$\pm$21.4 km	$\pm$17 km

located in Luxembourg. However, quasi-identical distances would be obtained for any array positioned in Europe and oriented in the East-West direction. The values in Table 1.3 clearly show that the optimal antenna separation decreases when the carrier frequency is increased. The inter-antenna distance error that can be accepted without entailing a capacity loss higher than 5 % is also displayed. Whereas the minimum optimal antenna distances are for example 48 km at 40 GHz and 38.4 km at 50 GHz, tolerance regions of $\pm$21.4 km and $\pm$17 km are allowed with the considered link budget, respectively. It thus becomes obvious that a MIMO LOS satellite link can be reliably operated even though carrier frequencies several GHz apart are used. This is a fundamental property that will facilitate the deployment of MIMO feeder links. The optimization of the antenna positions and the acceptable margin of errors will again be discussed in a more thorough manner in Chapter 3 to provide design guidelines. In particular, the impact of the Earth array orientation, which has not been discussed here, will be included.

1.3.5 Disambiguation: Other MIMO over Satellite Schemes

The MIMO LOS approach considered in this thesis should not be mistaken with other MIMO over satellite strategies which have been thoroughly studied in the literature [58]. These latter MIMO schemes, whose state-of-the-art is going to be briefly reviewed, can be classified as follows:

Interbeam interference mitigation: Considerable research efforts have been put in the last decade on the development of interference mitigation schemes for the user links of multibeam satellites with full frequency reuse. The literature on

this topic relies on a modelization of the channel between the satellite transmit feeds and the users on Earth as a MIMO channel. However, it is always assumed that the feeds are installed on the same reflector antenna. As predicted by the MIMO LOS theory, a sufficient separation of the transmit elements is in this case not guaranteed to obtain a maximum spatial multiplexing gain, and interference cannot be exploited constructively as in [57]. Studies on interbeam interference mitigation strategies considered nonlinear [59], [60] as well as linear approaches [61]–[64]. Initially, all the signals were assumed to be pre-processed and transferred to the satellite from a single gateway. This latter solution is however impractical due to the large data rate requirements of multibeam satellites and the limited uplink frequency resources. Thus, further research works on interference mitigation approaches for system with a multi-gateway architecture [65]–[68] were conducted. In [69], [70], other implementation constraints were also scrutinized to assess the feasibility of the proposed concept in a practical system. These additive constraints especially include the fact that, in the DVB-S2 standard, several users are embedded in a single frame to increase the coding gain. Using a multicast approach, different publications proposed MIMO pre-processing and user scheduling strategies adapted to this specific frame structure [71], [72].

Space-time codes for dual-polarized channels: Following the promising results of studies on dual-polarization for wireless terrestrial systems, the applicability of this approach was also investigated in the context of the land mobile satellite (LMS) channel. In this latter scenario, a dual-polarized communication link between one or two satellites and a mobile terminal with a non-directional antenna is established. Due to multipath propagation, significant depolarization effects are observed, and cross-polarized components carry a non-negligible part of the receive power. MIMO techniques can in this case exploit the cross-coupling between the polarizations. A MIMO channel is here used to take both the co-polar and cross-polar components of the receive signal into account. This

obviously represents a complete different approach than the MIMO LOS concept discussed in the previous section. Results of measurement campaigns and modeling approaches of the dual-polarized MIMO LMS channel at frequencies around 2.5 GHz are reported in the literature [73]–[76]. Space-time codes were also developed to exploit the multiplexing and diversity gains of MIMO LMS channels [77]–[79].

1.4 Contributions of this Thesis

1.4.1 Summary

In the following chapters, the design of MIMO-based feeder links for V/HTS system is thoroughly detailed. With the proposed architecture, an alternative to W-band and optical feeder links is introduced to solve the engineering challenges that have been listed in Section 1.2 while still using the Ka- and/or the Q/V-band. It relies on the use of two time- and phase-synchronized gateway antennas and two receive feeds per feeder link to create a MIMO LOS link. The presence of several gateway antennas separated by several tens of kilometers within the footprint of a feeder beam is a solution that has been envisioned for diversity purposes [80]. Products allowing the exploitation of such single-site diversity systems are even commercially available. However, these solutions only consider the activation of one of the gateway antennas whereas the other remains idle, which is not a cost-effective approach due to the unused redundant hardware. Here, the innovation lies in the simultaneous activation of the antennas to double the amount of supported user link bandwidth per feeder link. In this way, the number of gateway deployment sites[5] can be reduced in comparison to a state-of-the-art architecture. Therefore, the interference isolation of the feeder links, the integrated satellite-terrestrial network design and the robustness against rain fades can all be improved. The rest of this thesis is structured as follows:

Chapter 2: The system architecture, the hardware requirements and the time-varying

[5] A gateway site corresponds to an area of approximately 1000 km^2 centered at a beam boresight. Antennas deployed in this area belong to the same site.

channel characteristics of MIMO feeder links are discussed. A prediction method of the MIMO channel state to compensate for inherent delays in its estimation is also introduced.

Chapter 3: On-ground and on-board MIMO processing strategies are introduced to spatially multiplexed different data streams in a MIMO feeder link. The performance in terms of achievable uplink carrier to interference plus noise ratio (CINR) is analyzed. It is shown that there exists a large range of gateway antenna separations for which a close-to-optimal CINR can be reached in a MIMO feeder link. Moreover, the superiority of a joint ground/on-board processing in the case of a rain fade is highlighted. Finally, it is pointed out that a given set of MIMO gateway antennas can provide data to satellites positioned on different orbital slots.

Chapter 4: A smart diversity approach exploiting the specific architecture of MIMO-based feeder links is presented in Chapter 4 to guarantee a sufficient robustness against strong rain attenuations. To this end, a degraded mode, called a diversity mode, is first introduced to still support part of the traffic when a heavy rain event takes place at the location of one of the gateway antennas in a MIMO feeder link. Possible strategies for the allocation of the resources at a system level are then presented to fulfill the availability requirements of a V/HTS system. They consist in an extension of the $N + 0$ and $N + P$ smart diversity schemes to a MIMO-based system architecture.

Chapter 5: The research challenges addressed in this work are restated, and the main contributions are summarized. Moreover, perspectives for future research and development activities are provided.

Part of the results presented in the Chapters 3 and 4 have been published in conference proceedings and journals. The references to these works are listed below.

1.4.2 Conferences

- T. Delamotte, R. T. Schwarz, K. U. Storek, and A. Knopp, "MIMO feeder links for high throughput satellites", in *Proc. International ITG/IEEE Workshop on Smart Antennas (WSA'18)*, Invited paper, Mar. 2018, pp. 1–8

- T. Delamotte and A. Knopp, "Outage analysis of a MIMO-based smart gateway architecture", in *Proc. IEEE International Conference on Communications (ICC'18)*, May 2018, pp. 1–6

1.4.3 Journals

- T. Delamotte and A. Knopp, "Smart diversity through MIMO satellite Q/V-band feeder links", *IEEE Trans. Aerosp. Electron. Syst.*, vol. 56, no. 1, pp. 285–300, Feb. 2020

- R. T. Schwarz, T. Delamotte, K. Storek, and A. Knopp, "MIMO applications for multibeam satellites", *IEEE Trans. Broadcast.*, vol. 65, no. 4, pp. 664–681, Dec. 2019

Chapter 2

Basics of MIMO Feeder Links

Relying on studies about the applicability of MIMO for satellite communications which have been discussed in Chapter 1, the concept of MIMO feeder links is detailed. The required hardware for the gateways and the satellite payload design is especially assessed. A thorough description of the time-varying characteristics of MIMO feeder link channels is also presented. Finally, a method to predict the MIMO channel state using the knowledge of the small movements of a geostationary satellite around its orbital slot is described. This channel state prediction is essential to avoid an aging of the channel state information (CSI).

2.1 System Architecture

In this section, the architecture of MIMO-based feeder links is thoroughly described. First, an overview of the system is provided. The ground infrastructure of a single MIMO feeder link and the satellite payload design are then addressed in detail.

2.1.1 Overview

The forward link of a V/HTS system with a satellite payload positioned on a geostationary earth orbit is considered. To support the large aggregate bandwidth required for its multibeam downlink, N spatially separated 2×2 MIMO feeder links with a

full re-use of the available uplink frequency resources in the Ka-band (27.5–29.5 GHz) and/or the Q/V-band (42.5–43.5 GHz and 47.2–50.2 GHz) are deployed. An index

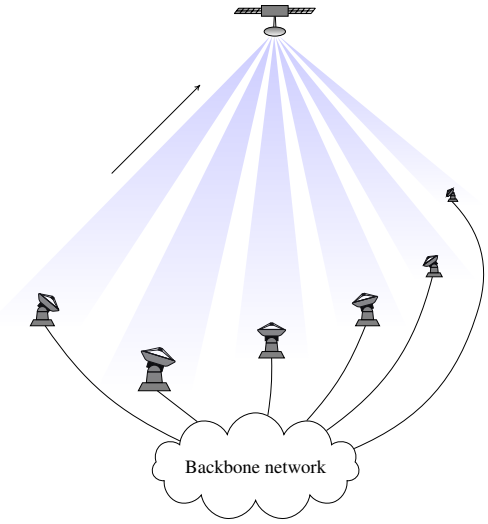

(a) State-of-the-art SISO feeder links

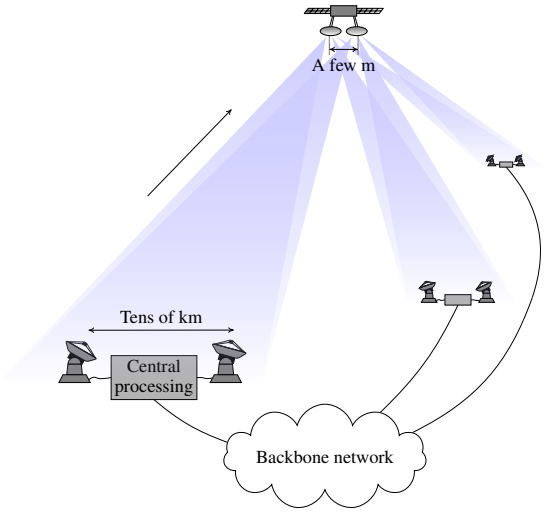

(b) Proposed MIMO feeder links

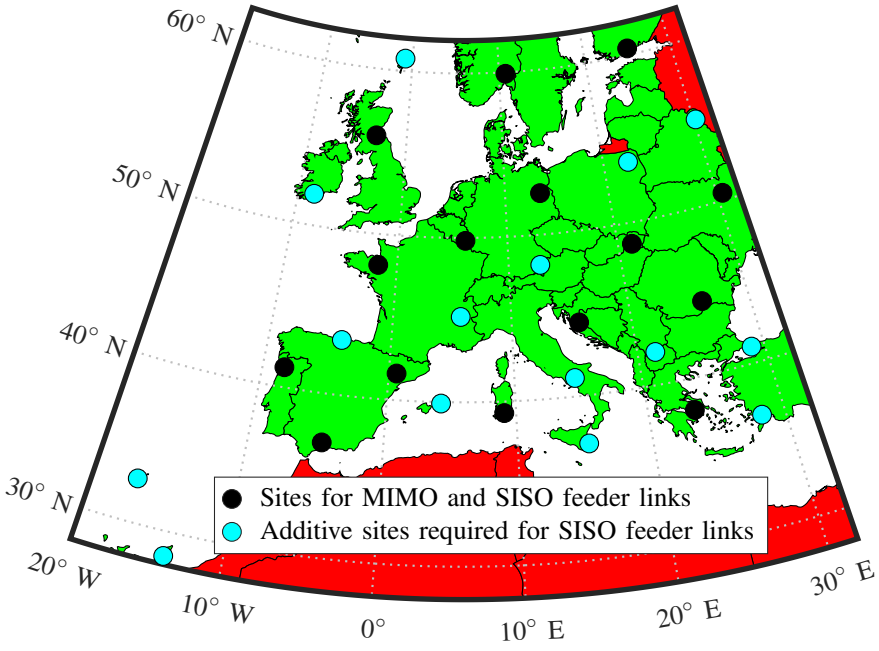

(c) Example of deployment in Europe

Figure 2-1: Feeder links for very high throughput satellites

ν, $1 \leq \nu \leq N$, will be used in the sequel to distinguish the different feeder links in the mathematical notations. A separation of several hundreds of kilometers between

the ground equipment of the different links is necessary to guarantee a sufficient interference isolation. The proposed architecture and a state-of-the-art configuration with single-input-single-output (SISO) links are illustrated in Fig. 2-1[1]. An example of sites selection for a ground segment composed of 15 MIMO feeder links or 30 SISO feeder links in Europe is also provided. The points stand here for the chosen deployment sites[2]. Contrary to the state-of-the-art, two active gateway antennas separated by a few tens of kilometers are installed in each site in the case of MIMO feeder links. In the illustrative example of Fig. 2-1, only the uplink part of the system is considered. The specific design adopted for the downlink is indeed not in the focus of this work. The four color scheme or a full frequency re-use [85] are for example popular approaches for the allocation of the downlink frequency resources. We note that the design of a comprehensive end-to-end solution using the MIMO LOS approach in the feeder links and in the user links is principally feasible [84].

Here, transparent payload architectures will be used. This especially implies that the bandwidths of the frequency channels in the uplink and in the downlink are identical. This bandwidth is denoted by B, and the assumption is made that it is a factor of the available uplink bandwidth W_{u} per feeder link and polarization state. Hence, with two antennas at each link end, a MIMO feeder link can support up to $K = 2 \times W_{\mathrm{u}}/B$ data streams per polarization state. For this purpose, a segmentation of the uplink band into $L = K/2$ frequency channels of bandwidth B combined with the resort to spatial multiplexing in each of them is used. A possible uplink

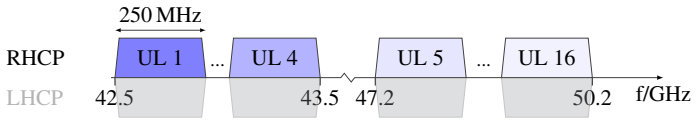

Figure 2-2: Frequency plan in the Q/V-band for $B = 250\,\mathrm{MHz}$ and $W_{\mathrm{u}} = 4\,\mathrm{GHz}$

frequency plan is shown in Fig. 2-2 for $B = 250\,\mathrm{MHz}$ and $W_{\mathrm{u}} = 4\,\mathrm{GHz}$ of bandwidth

[1] In Fig. 2-1a and Fig. 2-1b, a set of 3 MIMO links (or 6 SISO links) is displayed. However, next-generation V/HTS systems will require more than 15 MIMO feeder links (or 30 SISO feeder links).

[2] A gateway site corresponds to an area of approximately $1000\,\mathrm{km}^2$ at the center of a beam footprint. Antennas deployed in this area belong to the same site.

in the Q/V-band. The design of MIMO transmit/receive processing strategies for the transmission of two different data streams per uplink frequency channel is addressed in Chapter 3.

MIMO feeder links present several advantages for the design of V/HTS systems. First, by dividing the required number of gateway sites by two, they enable to relax the geographical, political and regulatory constraints that make the deployment of state-of-the-art ground infrastructures challenging. On the other hand, MIMO feeder links can also be advantageous in terms of robustness against strong rain fades. These advantages will be emphasized in Chapters 3 and 4.

2.1.2 Ground Infrastructure

The Earth portion of the ν-th MIMO feeder link consists of an array with two gateway antennas separated by a distance d_{E}^{ν} of a few tens of kilometers (generally, 20 km to 50 km). This distance is optimized according to the antenna arrangement on ground and in space. The orientation $\delta_{\mathrm{E}}^{\nu}$ characterizes the angle between the east-west direction and the antenna array. The location of the ground antennas is then perfectly defined with the knowledge of the array center coordinates i.e., its longitude $\theta_{\mathrm{E}}^{\nu}$ and its latitude ϕ_{E}^{ν} [38].

The antennas are connected to a central processing unit which is itself linked to the terrestrial backbone network. This unit receives the traffic that should be transferred to the satellite, and performs a MIMO pre-processing (or MIMO precoding) of the data streams to enable spatial multiplexing. The precoded signals are then transmitted to the antenna front-ends. A time and phase synchronized distribution is required to guarantee that a coherent transmission is realized. A radio-over-fiber solution can be used for this purpose [86]. It is for example state-of-the-art in the NASA deep space network where widely separated antennas must be synchronized for deep space communications, tracking and navigation functions or ground-based astronomical radar imaging operations. Originally, antenna arrays have only been used for downlink applications (e.g. reception of weak signals from interplanetary spacecrafts, very long baseline interferometry). Uplink arrays are indeed more chal-

lenging to design due to the need to precisely calibrate the array elements. The troposphere, the fiber-optic links connecting the antenna reflectors or the eletronics introduce phase perturbations that must be tracked and corrected. Meanwhile, the potential of uplink arrays to replace very large aperture reflectors has been investigated during the last decade [87]–[89]. In this case, the same signal is transmitted by the phase aligned array elements with the objective to maximize the effective isotropic radiated power (EIRP) at a desired target point in space. This technique is known as coherent combining. It has the advantage of being more cost-effective than a single very large antenna reflector with stringent hardware requirements and maintenance costs. Uplink arraying has been demonstrated in 2010 for X-band communication with a geosynchronous satellite [87]. Moreover, on-going works at NASA concentrate on the design of a Ka-band uplink array [89]. Whereas the goal of MIMO feeder links is not to perform coherent combining, the gateway antennas require a similar calibration. Here, different signals are radiated by the gateway antennas, and the coherent transmission ensures that a given phase relationship between these signals is fulfilled at the satellite antennas. This phase relationship is determined by the MIMO precoding. Finally, we observe that, since the slant path lengths between the antennas and the satellite can differ by several kilometers, the transmission of data symbols from the antenna with the shortest slant path must be delayed by a few microseconds. This ensures that symbols from the same time slot are received simultaneously at the satellite and, hence, that ISI from other slots is avoided. This need for a time alignment of the transmit antennas is illustrated in Section 2.2.1. The accuracy of the alignment must be within a negligible fraction of a symbol duration which is on the order of a few nanoseconds for typical V/HTS scenarios. With current technology, antenna arrays can be time-aligned with a precision of even a few picoseconds [88].

2.1.3 Satellite Payload

At the receive end of the feeder link, the satellite is equipped with two multifeed reflector antennas which are separated by a distance d_{S} of a few meters. The attitude control of the satellite i.e., the stabilization of its yaw, roll and pitch axes, is done

with a high precision [6] such that the antennas can be assumed to be fixed with respect to the center of mass of the satellite. In this work, the satellite antenna array is oriented in the east-west direction. The exact location of the antennas in a Earth centered, Earth fixed (ECEF) coordinate system can be determined from the position of the center of the antenna array. Even though a geostationary satellite is considered, this reference point will slightly move over time due to orbit perturbations. The characteristics of the satellite motion around its desired orbital position and the mathematical modeling of the antenna positions are detailed in Section 2.2.1.

For each antenna, an element of the multifeed network is used to form a beam pointing towards the center of a gateway antenna array on Earth. As a consequence, the ground equipment of a MIMO feeder link is illuminated by two beams. A set of overlapping beams formed by the satellite antennas is denominated as a *MIMO feeder beam*. Its beamwidth is sufficiently large such that depointing losses remain small [6]. This aspect is illustrated in Section 2.2.3. It is worth mentioning that, in a complete system, the total number of receive radio frequency (RF) chains is identical for a MIMO-based architecture and a state-of-the-art SISO solution. The difference is that, for SISO feeder links, all the receive feeds could be installed on the same reflector whereas, with the proposed MIMO scheme, the feeds are distributed between two reflectors. However, we note that the manufacturing of antenna sub-systems with a large number of feeds is a challenging task [9], [90]. Even with SISO links, more than one reflector may be necessary to enable the practical feasibility of the antenna assembly by reducing the size of the multifeed network per reflector. Hence, the need for a second payload antenna is not a constraint which is only encountered in the design of MIMO feeder links. Once received by the RF front ends, the signals are either frequency-converted and directly forwarded to the downlink or processed in a digital signal processor (DSP). The main building blocks of the payload for the feeder link part are shown in Fig. 2-3. Relying on the advancement of radiation tolerant DSPs, very high throughput satellites embark such equipment in their payloads to perform digital transparent processing (DTP). It is a form of on-board processing (OBP) where a sampled version of the signals is accessed to perform tasks such as flexible filter-

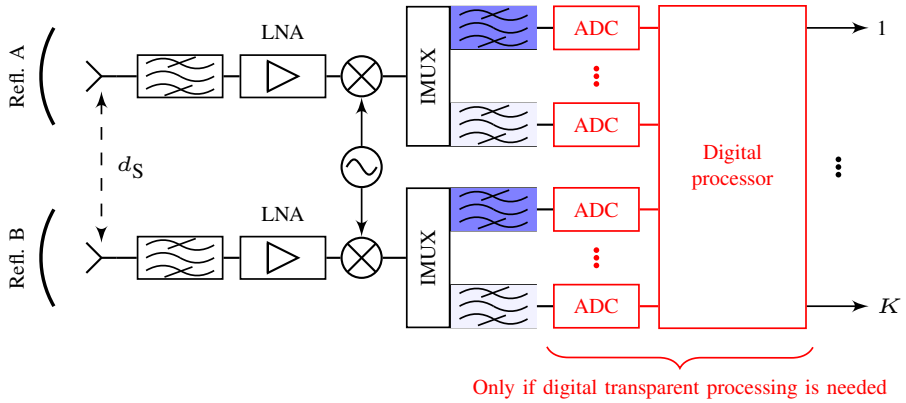

Figure 2-3: Feeder link part of the payload architecture

ing or downlink beamforming [10], [91]. For these architectures, also known as *digital bent-pipes*, field programmable gate arrays (FPGAs) or application specific integrated circuits (ASICs) are used. FPGAs have the advantage to be reconfigurable and to allow an adaptation of the processing to the evolution of the market needs during the satellite lifetime ($\approx$ 15 years for GEO satellites). Examples of V/HTS with flexible digital payloads are Konnect VHTS and SES-17, both expected to be launched in 2021. Based on their design, i.e. a multireflector architecture combined with a fully flexible beam-to-beam connectivity, these satellites could actually support the MIMO LOS technology. In Chapter 3, on-board digital processing capabilities will be exploited to perform non-regenerative MIMO processing. To this end, the phase coherence of the signals at the input of the DSP must be guaranteed. As shown in Fig. 2-3, a local oscillator gives a common reference to the frequency downconverters such that phase offsets remain identical in both RF paths. The distribution of a stable frequency reference can already be realized in systems supporting digital beamforming or multiuser multiple-input-multiple-output (MU-MIMO) precoding [70], [92]. Finally, the DSP must support matrix operations on wideband signals which is feasible with radiation tolerant systems-on-a-chip (SoCs) that are commercially available [93]. Regenerative digital payload architectures, where demodulation and decoding of the uplink signals are performed, represent another alternative of on-board processing. They especially enable to improve the link quality by isolating the uplink and the downlink [6]. However, regenerative payloads are significantly more complex than

transparent architectures. Moreover, they lack flexibility due to their dependence on the considered communication standard (e.g. symbols constellations, code rate,...). Even though the advent of software defined radio (SDR) brought new opportunities for the conception of flexible regenerative satellites, the significant amount of data that should be processed shifts the feasibility of such complex payloads to the long term [10], [94].

2.2 Channel Characteristics

The characterization of a MIMO feeder link channel requires to take several parameters into account. They include the slant paths geometry, which defines the LOS coefficients, the atmospheric impairments and the antenna radiation patterns. All these aspects are discussed in the sequel before the time-varying MIMO channel model is introduced in Section 2.3.

2.2.1 Slant Paths Geometry

The path lengths between each transmit-receive antenna pair influence the propagation delays and the phase shifts experienced by the signals. Even though a GEO satellite is considered, these distances are not perfectly constant over time. These variations are due to perturbations that slightly modify the orbit of the satellite such that it cannot be assumed to be a perfect circular geosynchronous orbit in the equatorial plane anymore. Orbit perturbations are due to the solar radiation pressure, the asymmetric Earth gravitational potential and the gravity of the Sun and of the Moon. The time-dependent distances between the gateway antennas and the satellite antennas can be determined with the knowledge of the orbital elements. These parameters are used to describe the orbit of the satellite in an Earth centered inertial (ECI) referential. They are defined as follows [95]:

Semimajor axis a: It represents the mean of the maximum r_{a} and the minimum r_{p} of the orbital radius i.e., $a = (r_{\mathrm{a}} + r_{\mathrm{p}})/2$.

Eccentricity e**:** This parameter, whose value is in the interval $[0, 1[$, characterizes, together with the semimajor axis, the shape of the orbit. It can be determined as $e = (r_\mathrm{a} - r_\mathrm{p}) / (r_\mathrm{a} + r_\mathrm{p})$. An eccentricity equal to 0 corresponds to a perfect circular orbit, whereas an elliptic orbit is obtained when $e > 0$.

Inclination i**:** The angle between the orbit plane and the equatorial plane is known as the orbital inclination.

Right ascension of the ascending node Ω**:** With this parameter, the angle measured eastwards in the equatorial plane from the direction of the First Point of Aries to the ascending node is defined. The ascending node is the intersection between the equatorial plane and the orbit section where the satellite travels north through this plane.

Argument of perigee ω**:** It corresponds to the angle measured in the orbit plane between the ascending node and the direction of the perigee which is the point where the orbital radius is minimum.

All these parameters are represented in Fig. 2-4. A sixth parameter, known as the true anomaly, allows to define the position of the satellite on its orbit at a specific time. However, this parameter will not be explicitly used in the sequel. As soon as the eccentricity e and/or the inclination i are not equal to zero, the satellite appears to librate around its desired orbital position. Using chemical or electric thrusters, regular corrections are required to guarantee that the perturbations affecting the orbital parameters are compensated. The objective is to restrict the motion of the satellite within a predefined region around its assigned orbital location. It is known as the station-keeping box, and its typical dimensions are $75\,\mathrm{km} \times 75\,\mathrm{km} \times 35\,\mathrm{km}$ [6]. Given a set of orbital parameters, the position of the satellite at time instant t for a fixed observer on Earth is determined with the longitude $\theta_\mathrm{S}(t)$ and the latitude $\phi_\mathrm{S}(t)$ of the subsatellite point. For the sake of convenience, the center of the antenna array is chosen as the reference point. The distance $R_\mathrm{S}(t)$ between the Earth's center and the projection of this reference point in the equatorial plane enables to fully characterize

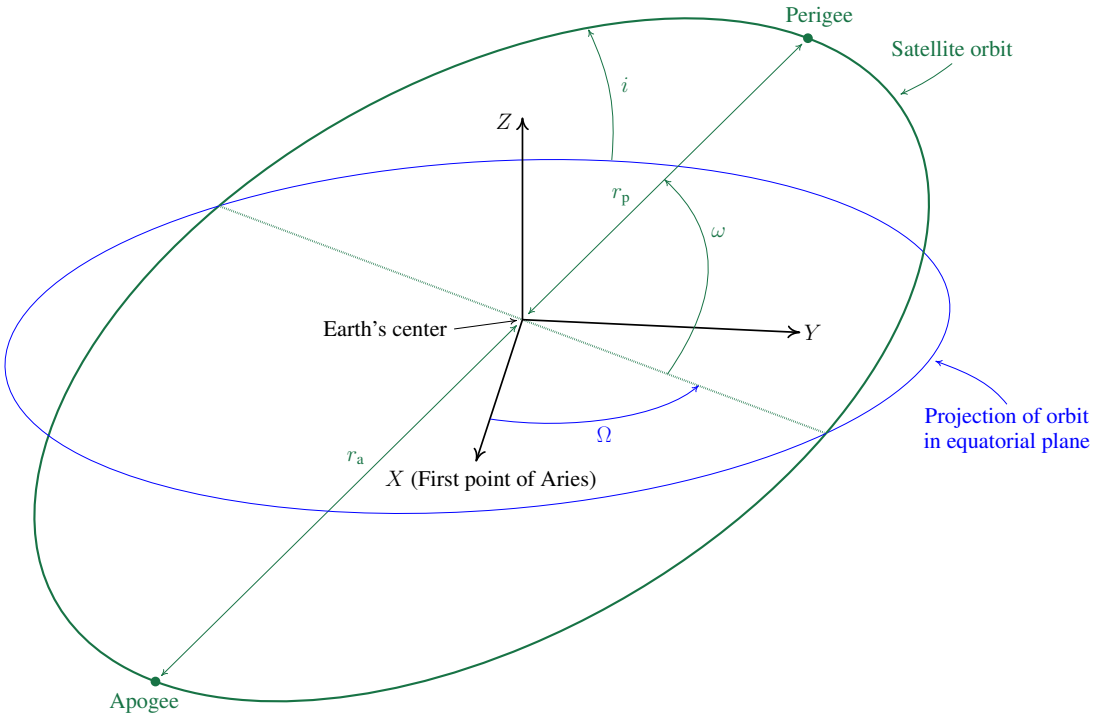

Figure 2-4: Parameters of the satellite orbit in an Earth centered inertial (ECI) coordinate system.

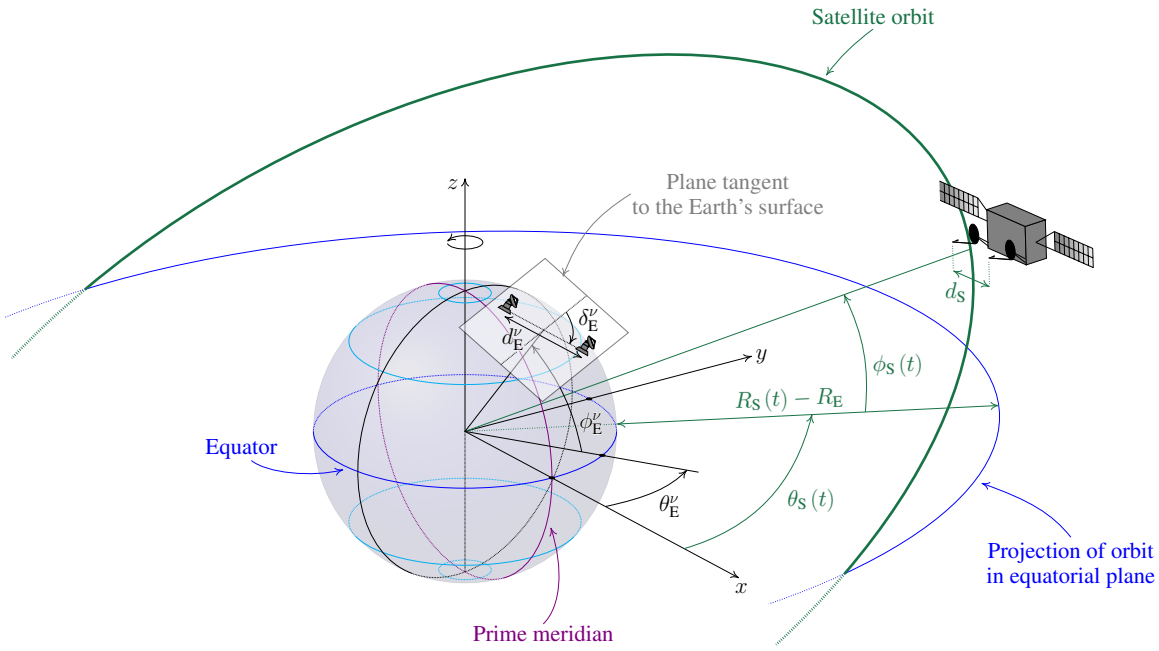

Figure 2-5: Parametric characterization of the antennas positions in an Earth centered, Earth fixed (ECEF) coordinate system.

the location of the antennas in an ECEF referential as illustrated in Fig. 2-5. In the sequel, $t = 0$ is arbitrarily defined as the time instant of the passage of the satellite at the orbit perigee. To express $\theta_{\mathrm{S}}(t)$, $\phi_{\mathrm{S}}(t)$ and $R_{\mathrm{S}}(t)$ in closed-form, the following intermediate variables are first defined [95]:

$$\mathbf{e} = [e_{\mathrm{x}},\ e_{\mathrm{y}}] = [e \cdot \cos(\Omega + \omega),\ e \cdot \sin(\Omega + \omega)] \quad \text{(Eccentricity vector)}\ , \tag{2.1}$$

$$\mathbf{i} = [i_{\mathrm{x}},\ i_{\mathrm{y}}] = [i \cdot \sin(\Omega),\ -i \cdot \cos(\Omega)] \quad \text{(Inclination vector)}\ , \tag{2.2}$$

$$s(t) = \Omega + \omega + \psi \cdot t \quad \text{(Sidereal angle of the satellite)}\ , \tag{2.3}$$

$$D = -1.5 \cdot \frac{a - A}{A} \quad \text{(Mean longitude drift rate)}\ , \tag{2.4}$$

with $\psi = 360.985\,647\,^{\circ}/\mathrm{d}$ and $A = 42\,164.2 \times 10^{3}\,\mathrm{m}$, the angular speed of the Earth rotation and the radius of the ideal circular geosynchronous orbit, respectively. The mean longitude drift rate D is a dimensionless variable which can be converted to a variable in $^{\circ}/\mathrm{d}$ by multiplying it with ψ. The position of the satellite in an ECEF referential at time instant t is then described by [95]:

$$\theta_{\mathrm{S}}(t) = \theta_{\mathrm{S}}(0) + D \cdot \{s(t) - s(0)\} + 2e_{\mathrm{x}} \cdot \sin\{s(t)\} - 2e_{\mathrm{y}} \cdot \cos\{s(t)\}\ , \tag{2.5}$$

$$\phi_{\mathrm{S}}(t) = -i_{\mathrm{x}} \cdot \cos\{s(t)\} - i_{\mathrm{y}} \cdot \sin\{s(t)\}\ , \tag{2.6}$$

$$R_{\mathrm{S}}(t) = A \cdot \left[1 - \frac{D}{1.5} - e_{\mathrm{x}} \cdot \cos\{s(t)\} - e_{\mathrm{y}} \cdot \sin\{s(t)\}\right]\ . \tag{2.7}$$

A differentiation of $\theta_{\mathrm{S}}(t)$, $\phi_{\mathrm{S}}(t)$ and $R_{\mathrm{S}}(t)$ also allows to express the velocity of the satellite relative to the rotating Earth in the tangential (longitude), orthogonal (latitude) and radial directions as [95]:

$$V_{\mathrm{t}}(t) = V \cdot \left[D + 2e_{\mathrm{x}} \cdot \cos\{s(t)\} + 2e_{\mathrm{y}} \cdot \sin\{s(t)\}\right]\ , \tag{2.8}$$

$$V_{\mathrm{o}}(t) = V \cdot \left[i_{\mathrm{x}} \cdot \sin\{s(t)\} - i_{\mathrm{y}} \cdot \cos\{s(t)\}\right]\ , \tag{2.9}$$

$$V_{\mathrm{r}}(t) = V \cdot \left[e_{\mathrm{x}} \cdot \sin\{s(t)\} - e_{\mathrm{y}} \cdot \cos\{s(t)\}\right]\ , \tag{2.10}$$

where $V = A \cdot \psi$ is the velocity required for a satellite in an ECI referential to remain on the ideal geostationary orbit. The dimensional unit of the velocity components is

m/s if the value of ψ is converted to rad/s whereas i_{x} and i_{y} are expressed in radian. For the sake of illustration, the values taken by $V_{\mathrm{t}}(t)$, $V_{\mathrm{o}}(t)$ and $V_{\mathrm{r}}(t)$ are plotted

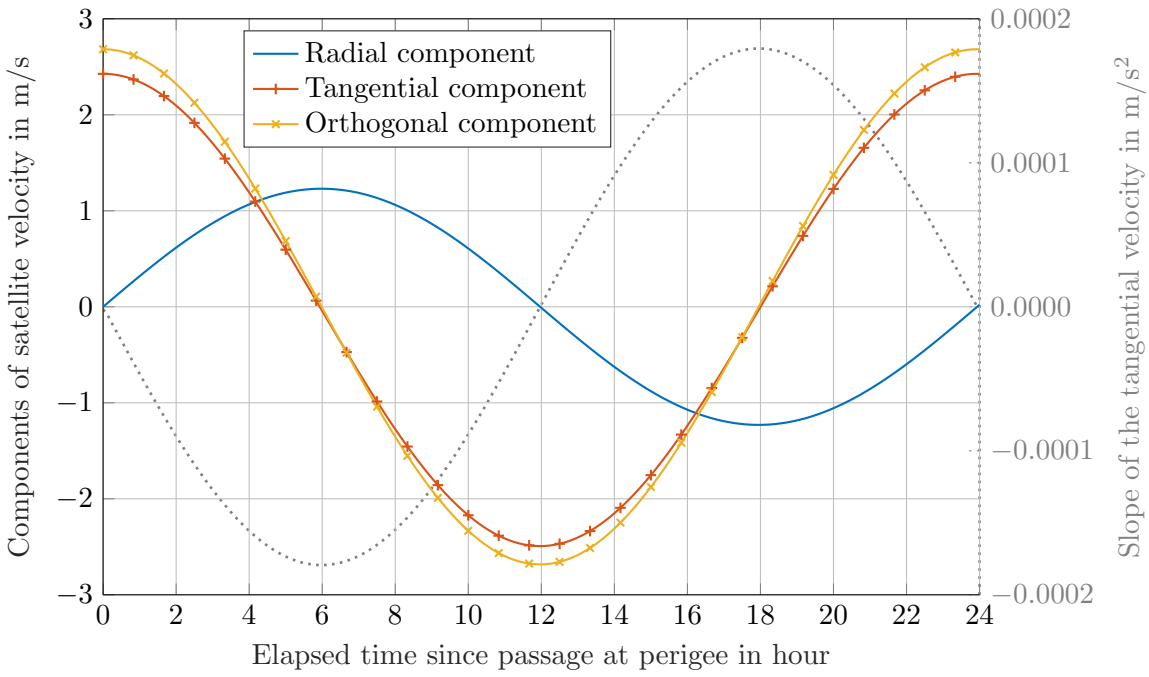

Figure 2-6: Components of the satellite velocity relative to the rotating Earth as a function of time.

in Fig. 2-6 as a function of time for $a = 42\,164.5 \times 10^3\,\mathrm{m}$, $e = 0.0004$, $i = 0.05°$, $\Omega = 90°$ and $\omega = 0°$. The eccentricity and the inclination have been chosen such that the pattern followed by the satellite around its desired orbital location reaches the bounds of a typical station-keeping box [6]. The results show that the velocity of the satellite with respect to a fixed observer on Earth can reach a few m/s in each direction. The values vary with a 24 h period, and the satellite velocity can be assumed constant over an observation period of a few seconds. For example, as shown in Fig. 2-6, the slope of the tangential component of the satellite velocity reaches a maximum of only $\pm 1.8 \times 10^{-4}\,\mathrm{m/s^2}$ in the considered configuration.

Relying on the closed-form characterization of the satellite position at a given instant t, the time-dependent distance between the n-th gateway antenna of the ν-th MIMO feeder link and the m-th satellite antenna is expressed as:

$$r_{mn}^{\nu}(t) = \left\| \mathbf{p}_{\mathrm{S},m}(t) - \mathbf{p}_{\mathrm{E},n}^{\nu} \right\|_2 , \tag{2.11}$$

with

$$\mathbf{p}_{\mathrm{S},m}(t) = \begin{bmatrix} R_{\mathrm{S}}(t)\cos\{\theta_{\mathrm{S}}(t)\} - \Delta_{\mathrm{S},m}\sin\{\theta_{\mathrm{S}}(t)\} \\ R_{\mathrm{S}}(t)\sin\{\theta_{\mathrm{S}}(t)\} + \Delta_{\mathrm{S},m}\cos\{\theta_{\mathrm{S}}(t)\} \\ R_{\mathrm{S}}(t)\tan\{\phi_{\mathrm{S}}(t)\} \end{bmatrix} , \tag{2.12}$$

$$\mathbf{p}^{\nu}_{\mathrm{E},n} = \begin{bmatrix} R_{\mathrm{E}}\cos\{\phi^{\nu}_{\mathrm{E}}\}\cos\{\theta^{\nu}_{\mathrm{E}}\} - \Delta^{\nu}_{\mathrm{E},n}\big[\sin\{\theta^{\nu}_{\mathrm{E}}\}\cos\{\delta^{\nu}_{\mathrm{E}}\} + \sin\{\phi^{\nu}_{\mathrm{E}}\}\cos\{\theta^{\nu}_{\mathrm{E}}\}\sin\{\delta^{\nu}_{\mathrm{E}}\}\big] \\ R_{\mathrm{E}}\cos\{\phi^{\nu}_{\mathrm{E}}\}\sin\{\theta^{\nu}_{\mathrm{E}}\} + \Delta^{\nu}_{\mathrm{E},n}\big[\cos\{\theta^{\nu}_{\mathrm{E}}\}\cos\{\delta^{\nu}_{\mathrm{E}}\} - \sin\{\phi^{\nu}_{\mathrm{E}}\}\sin\{\theta^{\nu}_{\mathrm{E}}\}\sin\{\delta^{\nu}_{\mathrm{E}}\}\big] \\ R_{\mathrm{E}}\sin\{\phi^{\nu}_{\mathrm{E}}\} + \Delta^{\nu}_{\mathrm{E},n}\cos\{\phi^{\nu}_{\mathrm{E}}\}\sin\{\delta^{\nu}_{\mathrm{E}}\} \end{bmatrix} . \tag{2.13}$$

The variables $\Delta_{\mathrm{S},m} = d_{\mathrm{S}} \cdot (m - 1.5)$ and $\Delta^{\nu}_{\mathrm{E},n} = d^{\nu}_{\mathrm{E}} \cdot (n - 1.5)$ are the signed distances between the array centers and the antennas on the satellite and on Earth, respectively. Here, the distance between the Earth's center and any point on its surface is set equal to the Earth's mean radius $R_{\mathrm{E}} = 6378.1\,\mathrm{km}$. Moreover, since the gateway antennas are separated by only a few tens of kilometers, the Earth's curvature is neglected.

The evolution of the path lengths within a short period of time Δt can also be analytically described. This will later be used in Section 2.3 to formulate requirements for a reliable exploitation of CSI at the transmitter. Since a satellite does not move in its station-keping box faster than a few meters per second whereas the values of interest for Δt will not exceed more than a few seconds, a first-order Taylor series expansion can be used to express $r^{\nu}_{mn}(t + \Delta t)$ as a function of $r^{\nu}_{mn}(t)$. It is given by:

$$r^{\nu}_{mn}(t + \Delta t) = r^{\nu}_{mn}(t) + \frac{d}{du} r^{\nu}_{mn}(u)\bigg|_{u=t} \cdot \Delta t \, , \tag{2.14}$$

where

$$\frac{d}{du} r^{\nu}_{mn}(u)\bigg|_{u=t} = \frac{\mathbf{v}^{\mathrm{T}}_{\mathrm{S}}(t) \cdot \left\{\mathbf{p}_{\mathrm{S},m}(t) - \mathbf{p}^{\nu}_{\mathrm{E},n}\right\}}{r^{\nu}_{mn}(t)} = \mathbf{v}^{\mathrm{T}}_{\mathrm{S}}(t) \cdot \mathbf{q}^{\nu}_{mn}(t) \ . \tag{2.15}$$

The vector $\mathbf{v}_{\mathrm{S}}(t)$ is the velocity vector of the satellite relative to the rotating Earth at time instant t. Moreover, $\mathbf{q}^{\nu}_{mn}(t)$ is a unit vector pointing from the n-th gateway antenna to the m-th satellite antenna. Since the distance between a transmit antenna

and the satellite is large, it can be assumed that $\mathbf{q}_{m1}^{\nu}(t) = \mathbf{q}_{m2}^{\nu}(t) = \mathbf{q}_{m}^{\nu}(t)$. As a consequence, the variations of the path lengths between the m-th gateway antenna and the two satellite antennas are equal. On the other hand, the path lengths from different gateway antennas vary unevenly. The differential path length variation between a signal transmitted from the first ground antenna and a signal transmitted from the second one is defined as:

$$\Delta r^{\nu}(t;\Delta t) = \mathbf{v}_{\mathrm{S}}^{\mathrm{T}}(t) \cdot \Delta\mathbf{q}^{\nu} \cdot \Delta t \ , \tag{2.16}$$

with $\Delta\mathbf{q}^{\nu} = \mathbf{q}_{2}^{\nu}(t) - \mathbf{q}_{1}^{\nu}(t)$ a time-independent vector originating at the first gateway antenna and pointing to the second one. Obviously, $\Delta r^{\nu}(t;\Delta t)$ is maximum if $\Delta\mathbf{q}^{\nu}$ and $\mathbf{v}_{\mathrm{S}}(t)$ are collinear i.e., that the satellite moves in a direction parallel to the direction of the gateway antenna array. Conversely, it is zero if $\Delta\mathbf{q}^{\nu}$ and $\mathbf{v}_{\mathrm{S}}(t)$ are orthogonal to each other. The contribution of the radial, tangential and orthogonal components of the satellite motion to $\Delta r^{\nu}(t;\Delta t)$ are obtained by using the following decomposition of the velocity vector:

$$\mathbf{v}_{\mathrm{S}}(t) = V_{\mathrm{r}}(t) \cdot \mathbf{u}_{\mathrm{r}} + V_{\mathrm{t}}(t) \cdot \mathbf{u}_{\mathrm{t}} + V_{\mathrm{o}}(t) \cdot \mathbf{u}_{\mathrm{o}} \tag{2.17}$$

The vectors of the orthonormal basis $\{\mathbf{u}_{\mathrm{r}}, \mathbf{u}_{\mathrm{t}}, \mathbf{u}_{\mathrm{o}}\}$ point in the radial, tangential and orthogonal direction, respectively. The decomposition of the satellite movement in these three directions is illustrated in Fig. 2-7. The differential path length variation is finally given by:

$$\Delta r^{\nu}(t;\Delta t) = \Delta r_{\mathrm{r}}^{\nu}(t;\Delta t) + \Delta r_{\mathrm{t}}^{\nu}(t;\Delta t) + \Delta r_{\mathrm{o}}^{\nu}(t;\Delta t) \ , \tag{2.18}$$

with

$$\Delta r_{\mathrm{x}}^{\nu}(t;\Delta t) = \mathbf{u}_{\mathrm{x}}^{\mathrm{T}} \cdot \Delta\mathbf{q}^{\nu} \cdot V_{\mathrm{x}}(t) \cdot \Delta t \ , \quad \text{x = r, t or o} \ . \tag{2.19}$$

In Section 2.3, the result from (2.19) will enable to analyze the relative phase shifts of the MIMO channel coefficients due to the satellite movement.

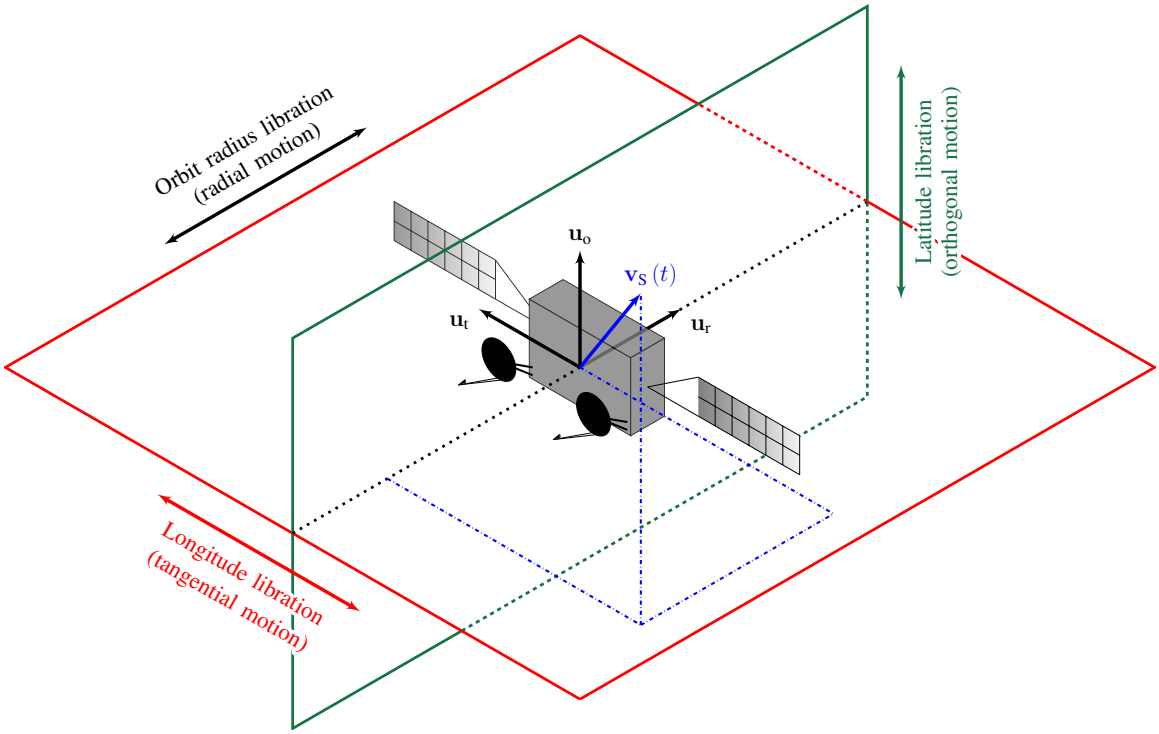

Figure 2-7: Decomposition of the satellite motion relative to the rotating Earth in three components: radial, tangential and orthogonal

2.2.2 Atmospheric Impairments

In the frequency bands of interest i.e., the Ka- and/or Q/V-bands, the lowest layer of the atmosphere, known as the troposphere, entails amplitude and phase distortions of the signals transmitted by the gateway antennas [16], [96]. The impairments are the consequence of different phenomena occurring in the propagation medium. For links with a sufficiently high elevation angle (e.g.,$\geq 30°$), the effects to be considered are:

Gaseous absorption: Water vapor and oxygen are dominant contributors to the gaseous absorption of millimeter waves. The attenuation induced by other atmospheric gases can be neglected [97]. The total gaseous absorption does not exceed a few decibels, and it only slowly varies over time due to daily and seasonal changes of the water vapor content. The absorption caused by oxygen, on the other hand, remains constant [17]. The statistics of the attenuation due to gases can be determined with the ITU-R recommendation P.676 [98].

Cloud attenuation: Liquid water droplets contained in clouds interact with the electromagnetic waves. The resulting attenuation increases with the carrier frequency, and it can reach a few decibels in the Q/V-band [99]. Changes in the strength of cloud attenuation are linked to variations of the liquid water content and of temperature [17]. Such fluctuations occur generally on timescales ranging from a few seconds to a few minutes. The ITU-R recommendation P.840 provides tools for the determination of the cloud attenuation statistics [100].

Rain attenuation: Raindrops can lead to a significant loss of the signal power. They are the main source of attenuation when a rain event occurs. The strength of the attenuation is a growing function of the frequency, and losses of more than 10 dB can be observed. Smart diversity strategies have been proposed in the literature to cope with strong rain fades in the feeder links of V/HTS systems [15], [16]. The rain attenuation statistics can be modelled using the ITU-R recommendation P.618 [96]. Concerning the rate of change of the attenuation, fade slopes of a few tenths of decibel can be reached under severe weather conditions. For example, values of ± 0.4 dB/s have been measured at 50 GHz in Madrid when the attenuation reaches 10 dB as reported in [101].

Variations of the refractive index: Water vapor, water droplets and raindrops cause a variation of the refractive index. This influences the effective path length of the electromagnetic waves which are consequently delayed by up to some tens of picoseconds. The phenomenon can be categorized in large-scale and small-scale effects.

Large-scale effects Atmospheric parameters, including pressure, temperature and humidity, affect the mean value of the refractive index in a given region. As a matter of fact, the effective path length varies with the weather conditions [102], [103]. During a rain event, the extra propagation delay due to the troposphere can be related to the rain attenuation value as explained in [102].

Small-scale effects The inhomogeneous distribution of water in the atmosphere, and the presence of turbulent airflows lead to a small-scale variation of the refractive index. It results in a multipath effect and, hence, a distortion of the wavefront. A rapid fluctuation of the amplitude and phase of the signal received at the antenna feed is then observed. It is known as the scintillation effect [104]–[112]. To distinguish scintillation impairments in rainy/cloudy and clear-air environments, the terms of wet scintillation and dry scintillation are generally used in the literature [109], [110]. Amplitude and phase scintillation has a coherence time on the order of one second [107], [113]. Peak-to-peak variations increase with frequency [108], [109], [114]. On the contrary, they decrease with the diameter of the ground antenna thanks to an aperture averaging effect [105], [107], [112].

All the atmospheric impairments discussed in this section must be included in the channel model of MIMO feeder links to appropriately describe the propagation environment. As further detailed in Chapter 3, their evolution over time has to be tracked to obtain an accurate CSI and be able to perform MIMO processing. Here, the fastest varying tropospheric impairments are the scintillation and, in case of a heavy rain event, the rain attenuation. The update rate of a CSI acquisition scheme must ensure that the fluctuations of these atmospheric effects is precisely monitored.

2.2.3 Antenna Radiation Pattern

The radiation pattern of an antenna models the amount of power transmitted/received in/from a given angle. With directive antennas, it consists of a main lobe, concentrating most of the power, and of side lobes that radiate or capture signals in undesired directions. The antenna boresight, which is the direction in the main lobe for which the power is maximum, constitutes the axis of reference. For the ground stations, it is pointed towards the satellite. Operators use precise tracking strategies to follow the movement of the satellite in its station-keeping box and, hence, minimize pointing errors. The accuracy of closed-loop automatic tracking, where the antenna pointing

is adjusted by following a beacon signal from the satellite, is generally on the order of some thousands of a degree. This level of precision enables to maintain the depointing loss of the ground stations smaller than a few hundreds of a decibel [6]. In this work, it is thus assumed that the gain of the gateway antennas is maximum. Even though some minor transmit depointing losses are present, they are similar for MIMO feeder links and for state-of-the-art SISO links such that a comparison between them will not be impacted. On the other hand, the radiation pattern of the satellite antennas must be thoroughly considered. First, the design of MIMO feeder links is such that the boresights of the receive antennas are pointed towards the center of the gateway antenna arrays. This is a fundamental difference with respect to the state-of-the-art where the beams are directed to a gateway antenna in each feeder link. The receive depointing loss of MIMO feeder links must hence be analyzed. Moreover, the interference between the different feeder links of a V/HTS system must be known to determine their link budgets. To this end, the interference power captured in the main lobe or in the side lobes of the radiation pattern should be taken into account. For circular aperture antennas, it is symmetrical about the boresight. In this case, the normalized radiation pattern at frequency f_c can be determined as follows [115]:

$$\Psi(\epsilon) = \left|\Gamma(\epsilon)/\Gamma(0)\right|^2, \tag{2.20}$$

with

$$\Gamma(\epsilon) = 2\pi \int_0^{\frac{\Delta_\mathrm{a}}{2}} \gamma(r) \cdot J_0\left\{\frac{2\pi f_\mathrm{c}}{c_0} r \sin(\epsilon)\right\} \cdot r\, dr\ . \tag{2.21}$$

The variable ϵ stands for the off-axis angle, i.e. the angle with respect to the boresight direction, whereas Δ_a is the aperture diameter. Furthermore, the functions J_0 and γ are the zero order Bessel function of first kind and the aperture amplitude distribution, respectively. Here, the following raised cosine distribution[3] for $0 \leq r \leq \Delta_\mathrm{a}/2$ is

[3]Other aperture amplitude distributions could be used [116]. However, some of these distributions actually lead to a radiation pattern which is very similar to the one obtained with a raised cosine distribution. The generality of conclusions drawn from results obtained with this latter distribution is thus not violated.

considered [117]:

$$\gamma(r) = \frac{1}{2} \cdot \left(1 + \frac{1}{\sqrt{T_\mathrm{e}}}\right) + \frac{1}{2} \cdot \left(1 - \frac{1}{\sqrt{T_\mathrm{e}}}\right) \cdot \cos\left(\frac{2\pi r}{\Delta_\mathrm{a}}\right) \ . \tag{2.22}$$

The ratio of the power collected by a feed from the center of the reflector to the power collected from the edge is known as the edge taper T_e. This parameter can be used to control the width of the main lobe and the sidelobe level of the radiation pattern. It should be known that the edge taper also influences in a practical system the efficiency and, as a consequence, the maximum gain of the antenna. A trade-off between spillover efficiency and illumination efficiency must be found to fulfill specific system requirements [118]. For example, an edge taper of 0 dB means that power is captured uniformly from all the reflector surface. The illumination efficiency is then maximized. Meanwhile, unwanted radiation coming beyond the edge of the aperture is also collected by the feed, and the spillover efficiency is minimal. Conversely, a high edge taper leads to a decrease of the illumination efficiency but to an increase of the spillover efficiency. Generally, a edge taper value between 10 dB and 20 dB is used [119].

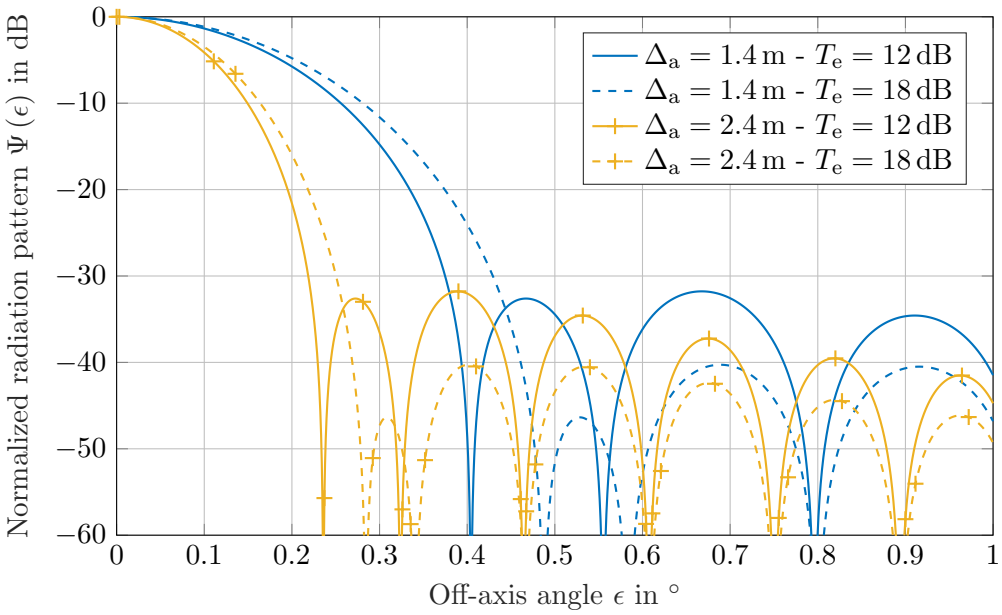

Figure 2-8: Normalized radiation pattern at 50 GHz

Normalized radiation patterns for aperture diameters of $\Delta_a = 1.4\,\text{m}$ and $\Delta_a = 2.4\,\text{m}$ are shown in Fig. 2-8 at $f_c = 50\,\text{GHz}$ for $T_e = 12\,\text{dB}$ and $T_e = 18\,\text{dB}$. The considered values of Δ_a are typical for satellite Q/V-band antennas [9], [120]. As expected, the width of the main lobe decreases if Δ_a is increased. Moreover, it can be observed that a larger edge taper value has the advantage of reducing the sidelobe level at the expense of a wider main lobe. The same behavior would be obtained for lower (or higher) frequencies with the difference that the main lobes would be wider (or narrower). For a given radiation pattern and boresight direction, the corresponding footprint on the Earth's surface can be determined using the approach from [117]. This is of interest to analyze the receive depointing loss and the interference level in a given feeder link based on the coordinates of the desired and interfering ground antennas, respectively. A thorough interference analysis will be conducted later in Chapter 3. Here, the footprint calculation is first used to evaluate the depointing loss in MIMO feeder links. The result is illustrated in Fig. 2-9 for $\Delta_a = 1.4\,\text{m}$,

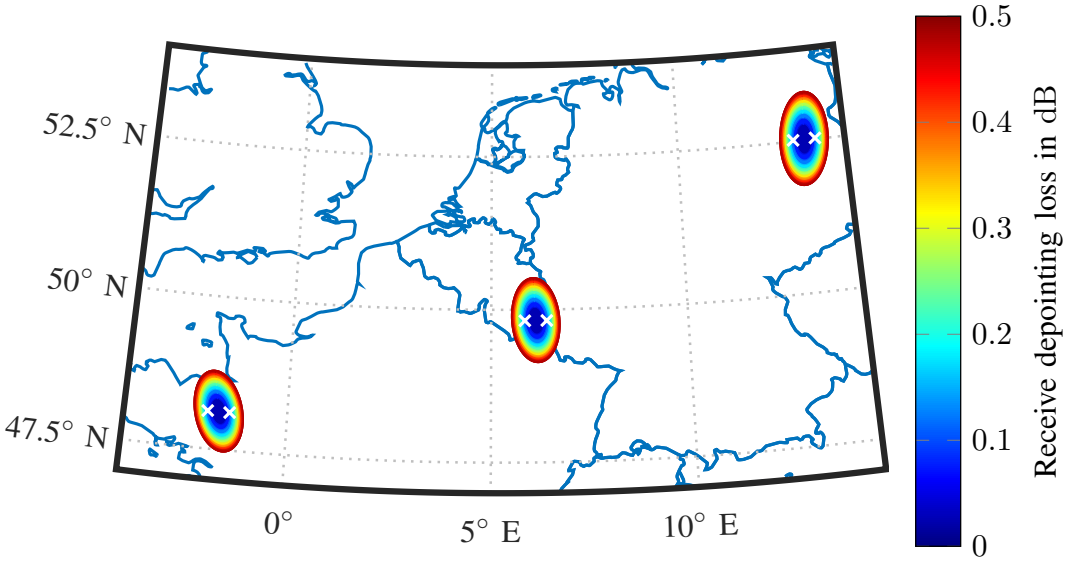

Figure 2-9: Receive depointing loss for beams pointed towards Rennes (France), Luxembourg and Berlin (Germany) for $f_c = 50\,\text{GHz}$, $\Delta_a = 1.4\,\text{m}$ and $T_e = 12\,\text{dB}$

$T_e = 12\,\text{dB}$ and $f_c = 50\,\text{GHz}$. The satellite orbital position is 9° E. The white crosses within each beam represent the antennas of a gateway array oriented in the east-west direction i.e., $\delta_E = 0°$, with an inter-antenna distance $d_E = 40\,\text{km}$. Obviously, the

receive depointing loss of MIMO feeder links remains limited even though the antenna boresights point towards the center of the gateway antenna arrays. In Fig. 2-10, the

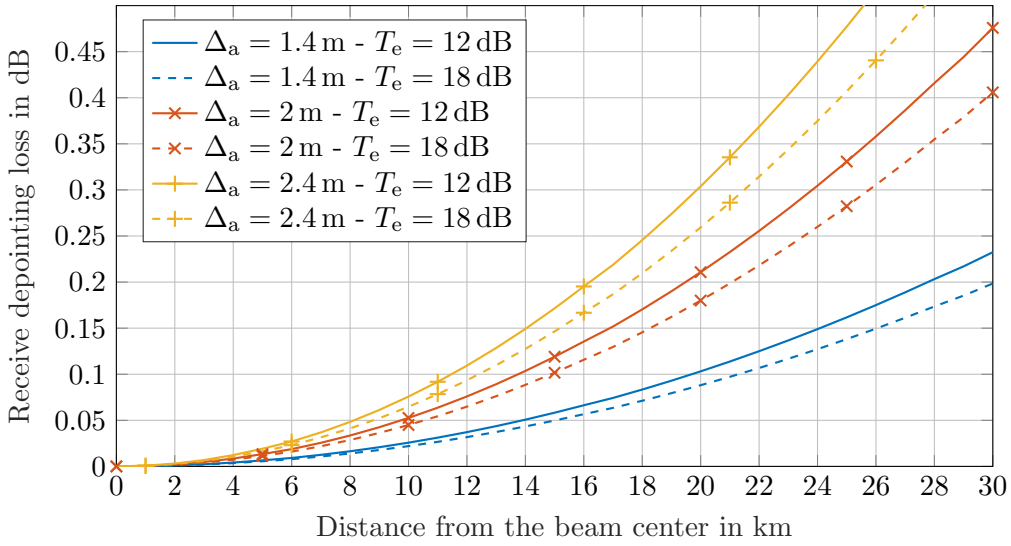

Figure 2-10: Receive depointing loss as a function of the distance in the east-west direction from a beam center located in Luxembourg for $f_c = 50\,\text{GHz}$

depointing loss is shown for different values of Δ_a and T_e as a function of the distance in the east-west direction from the beam center located in Luxembourg. For example, at a distance of 25 km from the beam center, the loss is equal to 0.16 dB for $\Delta_a = 1.4\,\text{m}$ and $T_e = 12\,\text{dB}$. It increases to 0.48 dB with $\Delta_a = 2.4\,\text{m}$. In the numerical results that will be presented in Chapters 3 and 4, a 0.5 dB higher depointing loss will be assumed for MIMO feeder links in comparison to SISO links. In view of the results from Fig. 2-10, it is a rather pessimistic scenario. However, it will be shown that, even in this case, MIMO feeder links significantly outperform the state-of-the-art.

2.3 Time-Varying MIMO Channel

Based on the propagation impairments discussed in the previous section, the model of the 2×2 MIMO link in a given channel of the uplink frequency plan can now be determined. The prediction of the MIMO channel at a given time instant from the knowledge of its state at a previous time instant is also analyzed at the end of this section.

2.3.1 Channel Model

Let's $\{x_n^\nu(\xi)\}_{\xi=-\infty}^{+\infty}$ be a sequence of symbols to be transmitted in a frequency channel centered at frequency f_c from the n-th gateway antenna in the ν-th feeder link[4]. The symbols have a duration T_{symb}, and they are normalized such that $\mathbb{E}[x_n^\nu(\xi)] \leq P_u^\nu$ where P_u^ν is the maximum EIRP that can be exploited for their transmission. The design of the symbols through the resort to MIMO precoding will be thoroughly discussed in Chapter 3. The time-alignment of the sequences received at the satellite from the two gateway antennas of a MIMO feeder link must be guaranteed. It can be achieved by controlling the pulse-shaping of the baseband signals as follows:

$$d_1^\nu(t) = \sum_{\xi=-\infty}^{+\infty} x_1^\nu(\xi) \cdot p(t - \Delta t_D^\nu - \xi \cdot T_{\text{symb}}) \ , \tag{2.23}$$

$$d_2^\nu(t) = \sum_{\xi=-\infty}^{+\infty} x_2^\nu(\xi) \cdot p(t - \xi \cdot T_{\text{symb}}) \ , \tag{2.24}$$

where $p(t)$ is a Nyquist pulse shaping filter. A raised cosine filter is for example used in the DVB-S2 standard[5] [121]. The variable Δt_D^ν enables to adjust the time-alignment of the symbol sequences $\{x_1^\nu(\xi)\}_{\xi=-\infty}^{+\infty}$ and $\{x_2^\nu(\xi)\}_{\xi=-\infty}^{+\infty}$. It will be expressed later in this section as a function of the path lengths between the gateway antennas and the satellite. After the pulse shaping, the baseband signals are used to modulate a carrier wave at frequency f_c such that the passband signal to be radiated by the n-th antenna is given by [122]:

$$\tilde{d}_n^\nu(t) = \sqrt{2} \cdot \text{Re}\left\{ d_n^\nu(t) \, e^{j2\pi f_c t} \right\} \ . \tag{2.25}$$

[4]Only one frequency channel is considered here. However, a feeder link uses in practice several frequency channels as illustrated in the frequency plan of Fig 2-2. A complete model of a MIMO feeder link should include the 2×2 MIMO links for all the available frequency channels. This will be done in Chapter 3.

[5]In practice, the filtering operation is actually split between the transmitter and the receiver. The pulse shaping and the matched filtering are then realized with a square-root raised cosine filter.

At the m-th satellite antenna, the noiseless part of the passband signal captured from feeder link ν by the feed allocated to feeder link ν' can be expressed as:

$$\tilde{y}_m^{\nu'\nu}(t) = \tilde{h}_{m1}^{\nu'\nu}(t) \cdot \tilde{d}_1^{\nu}\left(t - \frac{r_{m1}^{\nu}(t)}{c_0} - \beta_{\mathrm{R},1}^{\nu}(t)\right) + \tilde{h}_{m2}^{\nu'\nu}(t) \cdot \tilde{d}_2^{\nu}\left(t - \frac{r_{m2}^{\nu}(t)}{c_0} - \beta_{\mathrm{R},2}^{\nu}(t)\right), \tag{2.26}$$

where

$$\tilde{h}_{mn}^{\nu'\nu}(t) = \frac{c_0}{4\pi f_c r_{mn}^{\nu}(t)} \cdot \alpha_n^{\nu}(t) \cdot \sqrt{g_{\mathrm{e}} \cdot b_n^{\nu'\nu}}\,. \tag{2.27}$$

The variable $\beta_{\mathrm{R},n}^{\nu}(t)$ represents the extra time delay experienced by the signal from the n-th gateway antenna due to refraction in the troposphere. It includes the effects of the large-scale and small-scale variations of the refractive index discussed in Section 2.2.2. The tropospheric amplitude attenuation of the signal received at time instant t from the n-th transmit antenna is represented by $\alpha_n^{\nu}(t)$. In this work, this fading coefficient $\alpha_n^{\nu}(t)$ will be assumed to be identical in all the uplink frequency channels of the considered feeder link. This comes down to implicitly assuming that an uplink power control scheme balances the differences between the tropospheric attenuations in different frequency channels. The attenuation in dB is defined as $A_n^{\nu}(t) = -20 \cdot \log_{10}\{\alpha_n^{\nu}(t)\}$, and its statistics can be modeled using ITU-R recommendations. These statistics will be introduced in Chapter 3 to analyze the outage probability of the proposed system architecture [96]. The maximum gains of the transmit and receive antennas as well as the losses due to imperfections of the front-ends are included in g_{e}. Finally, $b_n^{\nu'\nu}$ is the normalized receive antenna gain. Its value depends on the position of the considered gateway antenna in the beam footprint of the ν'-th feeder link. If this antenna is not associated to the feeder link, it actually creates interference either at the edge of the main lobe or in the sidelobes of the radiation pattern. The equivalent baseband representation $y_m^{\nu'\nu}(t)$ of the receive passband signal $\tilde{y}_m^{\nu'\nu}(t)$ is obtained from (2.25), (2.26) and the following relation:

$$\tilde{y}_m^{\nu'\nu}(t) = \sqrt{2} \cdot \mathrm{Re}\left\{y_m^{\nu'\nu}(t)\, e^{j2\pi f_c t}\right\}\,. \tag{2.28}$$

After equating (2.28) and (2.26), it is easily established that:

$$y_m^{\nu'\nu}(t) = h_{m1}^{\nu'\nu}(t) \cdot d_1^{\nu}\left(t - \frac{r_{m1}^{\nu}(t)}{c_0} - \beta_{\mathrm{R},1}^{\nu}(t)\right) + h_{m2}^{\nu'\nu}(t) \cdot d_2^{\nu}\left(t - \frac{r_{m2}^{\nu}(t)}{c_0} - \beta_{\mathrm{R},1}^{\nu}(t)\right), \tag{2.29}$$

with

$$h_{mn}^{\nu'\nu}(t) = \frac{c_0}{4\pi f_{\mathrm{c}} r_{mn}^{\nu}(t)} \cdot \alpha_n^{\nu}(t) \cdot \sqrt{g_{\mathrm{e}} \cdot b_n^{\nu'\nu}} \cdot e^{-j2\pi f_{\mathrm{c}}\left(\frac{r_{mn}^{\nu}(t)}{c_0} + \beta_{\mathrm{R},n}^{\nu}(t)\right)}. \tag{2.30}$$

Using (2.23) and (2.24), the result from (2.29) can be reformulated as:

$$\begin{aligned} y_m^{\nu'\nu}(t) &= h_{m1}^{\nu'\nu}(t) \cdot \sum_{\xi=-\infty}^{+\infty} x_1^{\nu}(\xi) \cdot p\left(t - \Delta t_{\mathrm{D}}^{\nu} - \frac{r_{m1}^{\nu}(t)}{c_0} - \beta_{\mathrm{R},1}^{\nu}(t) - \xi \cdot T_{\mathrm{symb}}\right) \\ &\quad + h_{m2}^{\nu'\nu}(t) \cdot \sum_{\xi=-\infty}^{+\infty} x_2^{\nu}(\xi) \cdot p\left(t - \frac{r_{m2}^{\nu}(t)}{c_0} - \beta_{\mathrm{R},2}^{\nu}(t) - \xi \cdot T_{\mathrm{symb}}\right) \\ &= h_{m1}^{\nu'\nu}(t) \cdot \sum_{\xi=-\infty}^{+\infty} x_1^{\nu}(\xi) \cdot p\left(t - \Delta t_{\mathrm{D}}^{\nu} - \frac{r_{m1}^{\nu}(t)}{c_0} - \xi \cdot T_{\mathrm{symb}}\right) \\ &\quad + h_{m2}^{\nu'\nu}(t) \cdot \sum_{\xi=-\infty}^{+\infty} x_2^{\nu}(\xi) \cdot p\left(t - \frac{r_{m2}^{\nu}(t)}{c_0} - \xi \cdot T_{\mathrm{symb}}\right). \end{aligned} \tag{2.31}$$

The fact that $\beta_{\mathrm{R},n}^{\nu}(t)$ only reaches up to some tens of picoseconds whereas T_{symb} will be on the order of a few nanoseconds i.e., $\beta_{\mathrm{R},n}^{\nu}(t) \ll T_{\mathrm{symb}}$, has been used to obtain the last line of (2.31). To guarantee the time-alignment of the symbol sequences, it is then obvious that the delay $\Delta t_{\mathrm{D}}^{\nu}$ must be set equal to the differential propagation delay between the gateway antennas and the satellite which is given by:

$$\Delta t_{\mathrm{D}}^{\nu} = \frac{r_{m2}^{\nu}(t) - r_{m1}^{\nu}(t)}{c_0}. \tag{2.32}$$

For the sake of illustration, the evolution over time of the differential propagation delay between a gateway array in Mandra (Greece) and a satellite at 9° E is shown in Fig. 2-11. The gateway array is oriented in the east-west direction, and the inter-antenna distance is 40 km. Due to the movement of the satellite in its station-keeping

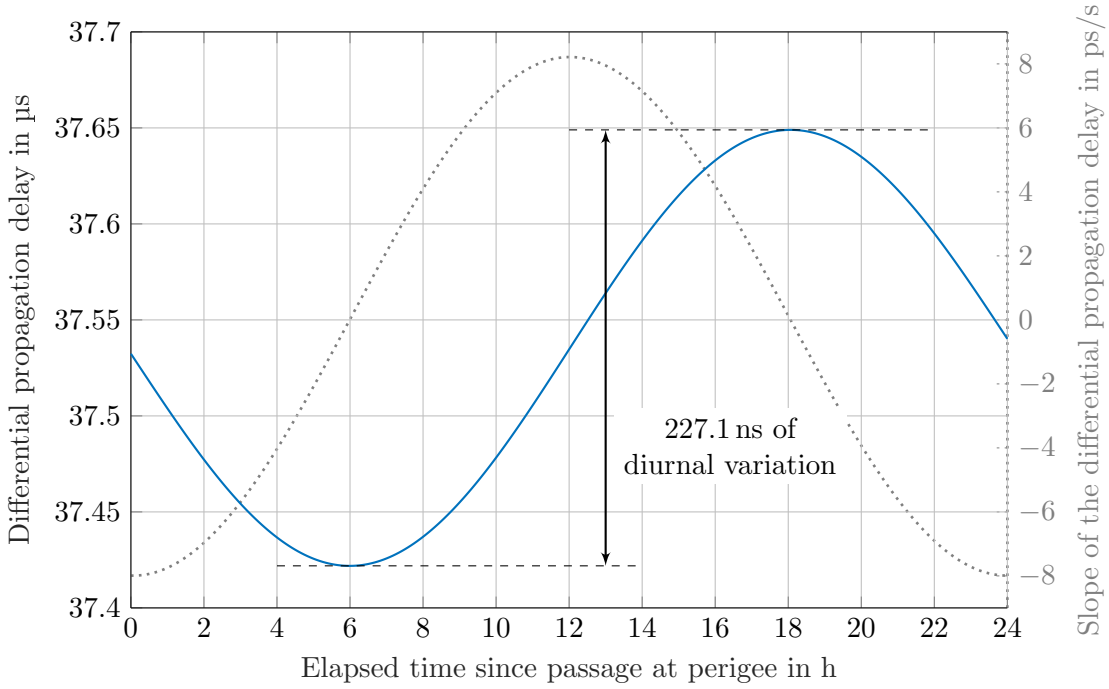

Figure 2-11: Differential propagation delay as a function of time for a gateway array positioned in Mandra (Greece) with $\delta_{\mathrm{E}} = 0°$ and $d_{\mathrm{E}} = 40\,\mathrm{km}$

box, the differential delay is not constant. However, its rate of change is only a few picoseconds per second such that it can be regularly estimated and compensated at the transmitter to avoid inter-symbol interference. It has also to be noted that, due to the small separation between the satellite antennas, the differential propagation delay is identical for all of them i.e., that the value of $\Delta t_{\mathrm{D}}^{\nu}$ in (2.32) is equal for $m = 1$ and $m = 2$. Based on (2.31) and (2.32), the noiseless part of the received signal at the m-th satellite antenna of a time-aligned MIMO feeder link writes in the equivalent baseband as:

$$y_m^{\nu'\nu}(t) = \sum_{\xi=-\infty}^{+\infty} \left\{ h_{m1}^{\nu'\nu}(t) \cdot x_1^{\nu}(\xi) + h_{m2}^{\nu'\nu}(t) \cdot x_2^{\nu}(\xi) \right\} \cdot p\left(t - \frac{r_{m2}^{\nu}(t)}{c_0} - \xi \cdot T_{\mathrm{symb}} \right) . \tag{2.33}$$

Since the filter $p(t)$ guarantees that a detection of the symbols at their optimal sampling instant will avoid the occurrence of ISI in time domain, the MIMO channel can be modeled on a per-symbol basis. The channel between the gateway antennas of the ν-th MIMO feeder link and the feeds of the satellite antennas allocated to the

ν'-th link can then be described by the following matrix:

$$\mathbf{H}^{\nu'\nu}(t) = \begin{bmatrix} h_{11}^{\nu'\nu}(t) & h_{12}^{\nu'\nu}(t) \\ h_{21}^{\nu'\nu}(t) & h_{22}^{\nu'\nu}(t) \end{bmatrix} . \tag{2.34}$$

The matrices with $\nu' \neq \nu$ will be used in Chapter 3 to model and analyze the interference between the different feeder links. Here, the following discussion first concentrates on the case $\nu' = \nu$ i.e., the matrix that represents the channel used to perform spatial multiplexing in the ν-th link. In practice, the transmission of the data symbols is done blockwise. With the DVB-S second generation (DVB-S2) standard, a block transmission requires for example a maximum of a few milliseconds which is well below the coherence time of the tropospheric impairments as discussed in Section 2.2.2. Therefore, it can be assumed to be a block-fading channel i.e., that the channel coefficients remain constant during the transmission of a block [123]. If I_{B} is the index set of symbols belonging to the same block, and t_{B} is the time instant at which the reception of this block starts, the desired received symbols in the ν-th link are determined as:

$$\mathbf{w}^{\nu}(\xi) = \begin{bmatrix} w_1^{\nu}(\xi) \\ w_2^{\nu}(\xi) \end{bmatrix} = \mathbf{H}^{\nu\nu}(t_{\mathrm{B}}) \cdot \begin{bmatrix} x_1^{\nu}(\xi) \\ x_2^{\nu}(\xi) \end{bmatrix} = \mathbf{H}^{\nu\nu}(t_{\mathrm{B}}) \cdot \mathbf{x}^{\nu}(\xi) \ , \quad \xi \in I_{\mathrm{B}} \tag{2.35}$$

In Chapter 3, the design of the sequences of transmit symbols $\{x_1^{\nu}(\xi)\}_{\xi \in I_{\mathrm{B}}}$ and $\{x_2^{\nu}(\xi)\}_{\xi \in I_{\mathrm{B}}}$ will require the knowledge of the channel matrix $\mathbf{H}^{\nu\nu}(t_{\mathrm{B}})$ at the transmitter. The accurate prediction of the CSI is addressed in the following section.

2.3.2 Channel State Prediction

Different strategies such as a looping back of an uplink signal from the satellite to the gateway or the exploitation of a modulated beacon can be envisioned to estimate the CSI. Meanwhile, the objective of this section is not to discuss the design of a specific CSI acquisition scheme. This aspect is addressed in more detail in Chapter 3. Here, the impact of a delay Δt between the estimation of the MIMO channel at a

time instant t_{CSI} and its exploitation for the design of blocks of symbols received by the satellite at time instant $t_{\mathrm{B}} = t_{\mathrm{CSI}} + \Delta t$ is discussed. Because of the propagation delays between the gateway antennas and the satellite, which reach a little bit more than 100 ms, such a latency cannot be avoided. Scintillation, which is the weather impairment that varies the fastest, can be reasonably assumed constant over a period of a few hundreds of milliseconds. As a consequence, the accuracy of the estimated weather impairments will not be strongly degraded due to channel aging provided that the refreshment rate of the CSI is sufficient. On the contrary, the movement of the satellite in its station-keeping box entails a non-negligible modification of the phase relationships between the LOS channel coefficients i.e., the coefficients depending on the path length geometry. To analyze the impact of this phenomenon, the results from Section 2.2.1 are used. Under the assumption that the time delay Δt does not exceed a few hundreds of milliseconds, the time-varying tropospheric impairments i.e., the attenuation $\alpha_n^{\nu}(t)$ and the phase shift $\varphi_n^{\nu}(t) = -2\pi f_{\mathrm{c}} \beta_{\mathrm{R},n}^{\nu}(t)$ in (2.30), do not change significantly. In this case, the following relation can be established:

$$\mathbf{H}^{\nu\nu}\left(t_{\mathrm{B}} = t_{\mathrm{CSI}} + \Delta t\right) = e^{j\kappa_2^{\nu}(t_{\mathrm{CSI}};\Delta t)} \cdot \mathbf{H}^{\nu\nu}\left(t_{\mathrm{CSI}}\right) \cdot \begin{bmatrix} e^{j\delta\kappa^{\nu}(t_{\mathrm{CSI}};\Delta t)} & 0 \\ 0 & 1 \end{bmatrix}, \tag{2.36}$$

with

$$\delta\kappa^{\nu}\left(t_{\mathrm{CSI}};\Delta t\right) = 2\pi f_{\mathrm{c}} \cdot \frac{\Delta r^{\nu}\left(t_{\mathrm{CSI}};\Delta t\right)}{c_0} = 2\pi f_{\mathrm{c}} \cdot \frac{\mathbf{v}_{\mathrm{S}}^{\mathrm{T}}\left(t_{\mathrm{CSI}}\right) \cdot \Delta\mathbf{q}^{\nu} \cdot \Delta t}{c_0}. \tag{2.37}$$

The phase shift $\kappa_2^{\nu}(t_{\mathrm{CSI}};\Delta t)$ depends on the path length variation from the second gateway antenna to the satellite. It is common to all channel entries and does not modify the structure of the MIMO channel matrix. Thus, it does not contribute to the aging of the CSI. On the contrary, the non-zero differential phase rotation $\delta\kappa^{\nu}(t_{\mathrm{CSI}};\Delta t)$ leads to a CSI mismatch. As shown in (2.37), it is expressed as a function of the different path length variation that has been introduced in (2.16). Its value is proportional to Δt.

The impact of the satellite motion in the radial, tangential and orthogonal di-

rections on $\delta\kappa^{\nu}\left(t_{\mathrm{CSI}};\Delta t\right)$ can be investigated by resorting to the decomposition of the differential path length variation from (2.18). In Fig. 2-12, the result of such an

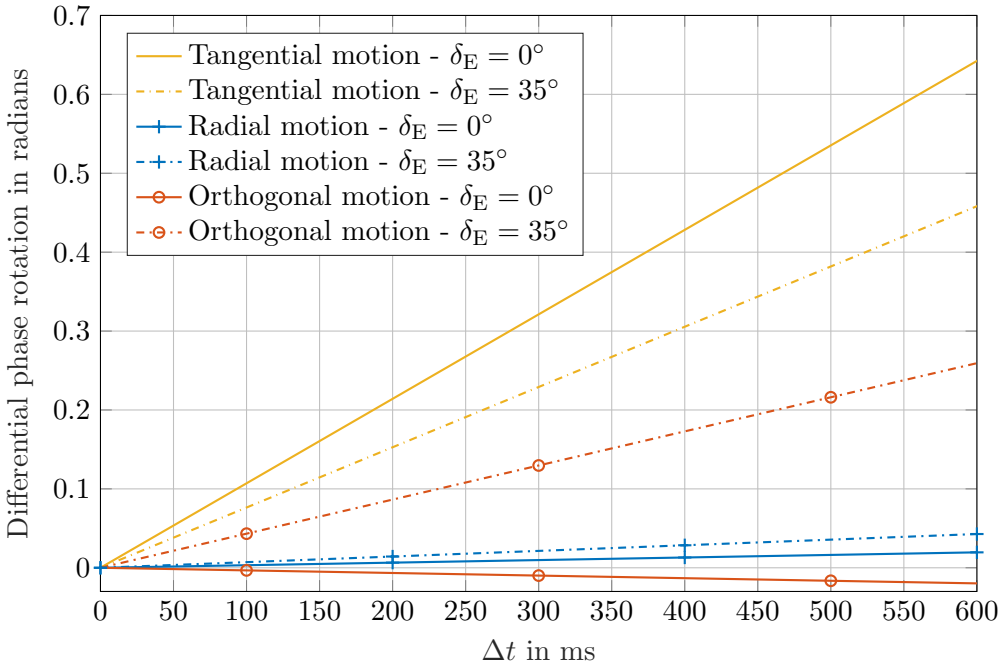

Figure 2-12: Differential phase rotation as a function of the delay Δt for a gateway array positioned in Mandra (Greece) with $d_{\mathrm{E}} = 40\,\mathrm{km}$, $f_{\mathrm{c}} = 50\,\mathrm{GHz}$ and velocity components $V_{\mathrm{r}}\left(t_{\mathrm{CSI}}\right) = V_{\mathrm{t}}\left(t_{\mathrm{CSI}}\right) = V_{\mathrm{o}}\left(t_{\mathrm{CSI}}\right) = 1\,\mathrm{m/s}$

analysis is shown at $f_{\mathrm{c}} = 50\,\mathrm{GHz}$ again for a gateway array in Mandra (Greece) and a satellite at 9° E. The velocity components of the satellite have all been set to 1 m/s. When $\delta_{\mathrm{E}} = 0°$, only the tangential motion of the satellite significantly contributes to the differential phase rotation. This is in accordance with the fact that the differential path length variation is maximum when the satellite moves in a direction parallel to the gateway array as explained in Section 2.2.1. After 300 ms, a difference of 0.32 rad is for example observed. The radial and the orthogonal motions have a negligible impact for $\delta_{\mathrm{E}} = 0°$. On the contrary, with $\delta_{\mathrm{E}} = 35°$, the orthogonal motion of the satellite also plays a substantial role in the aging of the CSI. A motion of the satellite in the north-south direction is, in this case, not quasi-orthogonal to the gateway array orientation, and the resulting phase shift cannot be ignored anymore.

To put it in a nutshell, even though a differential phase rotation of the MIMO channel coefficients is unavoidable, its predictable behavior over time enables to over-

come its impact on the CSI outdating. The MIMO channel for blocks of symbols that will be received at a time instant t_{B} can indeed be determined from a channel estimation performed a few hundreds of milliseconds earlier at $t_{\mathrm{CSI}} = t_{\mathrm{B}} - \Delta t$. To this end, the following procedure should be applied:

1. Estimation of the MIMO channel $\mathbf{H}^{\nu\nu}\left(t_{\mathrm{CSI}}\right)$ at time instant t_{CSI}
2. Determination of the differential phase rotation $\delta\kappa^{\nu}\left(t_{\mathrm{CSI}}; \Delta t\right)$ entailed by the motion of the satellite during the delay Δt
3. Phase rotation of the first column of $\mathbf{H}^{\nu\nu}\left(t_{\mathrm{CSI}}\right)$ with $\delta\kappa^{\nu}\left(t_{\mathrm{CSI}}; \Delta t\right)$

According to (2.36), the corrected channel state corresponds to the effective MIMO channel at $t_{\mathrm{B}} = t_{\mathrm{CSI}} + \Delta t$ up to a phase shift common to all entries. For the MIMO processing strategies introduced in Chapter 3, it will be implicitly assumed that this phase corrected CSI is used.

Chapter 3

Transmission Strategies

MIMO processing strategies are required to enable the spatial multiplexing of different data streams in a MIMO feeder link. In this chapter, the model used to represent a data transmission over a noisy channel with ground and on-board digital processing is first provided. The presented transmission chain model is exploited to design digital processing schemes. Here, a ground-limited and a joint ground/on-board processing approach are considered. The performance of a MIMO-based feeder link architecture is then analyzed in terms of uplink CINR. It is especially emphasized that a MIMO feeder link can be reliably exploited for a large range of gateway antennas separations and orbital slots. The role of on-board MIMO processing in improving the link robustness against strong tropospheric attenuations, particularly in the Q/V-band, is also discussed.

3.1 Transmission Chain Model

For the sake of notational simplicity, the continuous-time index t used in Chapter 2 is omitted in the following. Similarly, the discrete-time index ξ for the symbol sequences is discarded. A V/HTS system with a ground segment composed of N MIMO feeder links is here considered. In the ν-th MIMO feeder link, a vector of data symbols $\mathbf{s}^{\nu} = [s_1^{\nu}, \ldots, s_K^{\nu}]^{\mathrm{T}} \in \mathbb{C}^{K\times 1}$ must be transmitted at a specific time instant. Spatial multiplexing in $L = K/2$ non-interfering frequency channels will be used for this

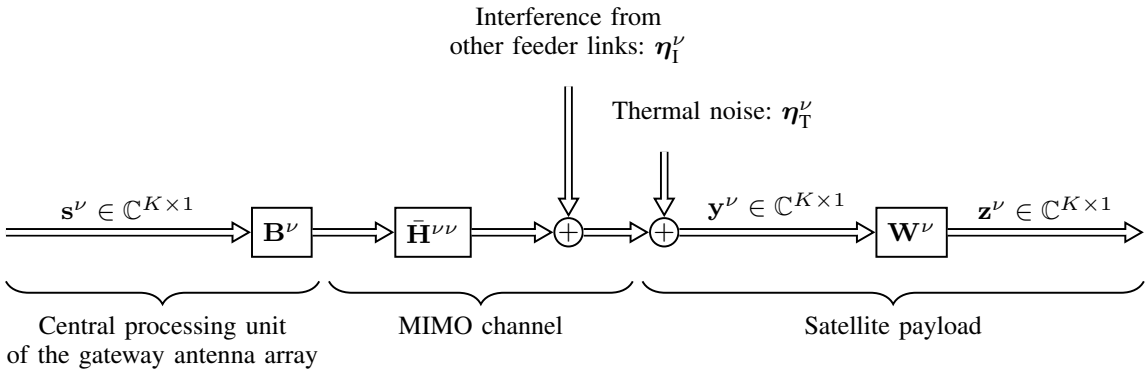

Figure 3-1: Transmission chain of a MIMO feeder link

purpose. The symbols in $\mathbf{s}^{\nu}$ are such that $\mathbb{E}\left[\mathbf{s}^{\nu}\left(\mathbf{s}^{\nu}\right)^{\mathrm{H}}\right] = \mathbf{I}_K$ and $\mathbb{E}\left[\mathbf{s}^{\nu'}\left(\mathbf{s}^{\nu}\right)^{\mathrm{H}}\right] = \mathbf{0}_K$, $\nu' \neq \nu$. As illustrated by the block diagram of the transmission chain in Fig. 3-1, the vector $\mathbf{s}^{\nu}$ is first pre-processed in the central processing unit of the gateway array with the help of a precoding matrix $\mathbf{B}^{\nu} \in \mathbb{C}^{K\times K}$. It must be designed under the constraint that the transmit power per gateway antenna in a given frequency channel should not exceed a threshold value. The ground stations are indeed equipped with high power amplifiers (HPAs) whose specification do not allow to overstep a certain transmit power. Moreover, power flux density threshold limits are imposed by regulatory authorities to avoid undesirable interference to other networks operating in the same frequency band. To formulate the per-antenna and per-carrier power constraint, the following partitioning of the precoder is considered:

$$\mathbf{B}^{\nu} = \left[\begin{array}{c} \mathbf{B}_1^{\nu} \\ \hline \vdots \\ \hline \mathbf{B}_L^{\nu} \end{array}\right] . \tag{3.1}$$

The matrix $\mathbf{B}_l^{\nu} \in \mathbb{C}^{2\times K}$ is the part of the precoding matrix which maps the content of the vector $\mathbf{s}^{\nu}$ to the inputs of the MIMO channel at carrier frequency $f_{\mathrm{c},l}$. Denoting $P_{\mathrm{u},l}^{\nu}$ the maximum EIRP per antenna in the l-th channel, the condition that must be fulfilled is given by:

$$\left[\mathbf{B}_l^{\nu}\left(\mathbf{B}_l^{\nu}\right)^{\mathrm{H}}\right]_{n,n} \leq P_{\mathrm{u},l}^{\nu} , \quad n = 1, 2 . \tag{3.2}$$

After the precoding operation, the symbols are distributed to the gateway antennas for their transmission in the feeder link. If $\mathbf{H}_l^{\nu\nu} \in \mathbb{C}^{2\times 2}$ is the MIMO channel in the l-th uplink frequency channel, the link including the L frequency channels is represented by the following block diagonal structure:

$$\bar{\mathbf{H}}^{\nu\nu} = \mathrm{diag}\left\{\mathbf{H}_1^{\nu\nu}, \ldots, \mathbf{H}_L^{\nu\nu}\right\} \ . \tag{3.3}$$

The vector of symbols received at the satellite then writes as:

$$\mathbf{y}^{\nu} = \begin{bmatrix} y_1^{\nu} \\ \vdots \\ y_K^{\nu} \end{bmatrix} = \bar{\mathbf{H}}^{\nu\nu}\mathbf{B}^{\nu}\mathbf{s}^{\nu} + \sum_{\substack{\nu'=1 \\ \nu'\neq\nu}}^{N} \bar{\mathbf{H}}^{\nu\nu'}\mathbf{B}^{\nu'}\mathbf{s}^{\nu'} + \boldsymbol{\eta}_{\mathrm{T}}^{\nu} = \bar{\mathbf{H}}^{\nu\nu}\mathbf{B}^{\nu}\mathbf{s}^{\nu} + \boldsymbol{\eta}_{\mathrm{I}}^{\nu} + \boldsymbol{\eta}_{\mathrm{T}}^{\nu} \ . \tag{3.4}$$

The matrix $\bar{\mathbf{H}}^{\nu\nu'}$ for $\nu' \neq \nu$ has the same structure as $\bar{\mathbf{H}}^{\nu\nu}$ in (3.3) with the difference that it models the interference experienced in the considered link ν from the ν'-th MIMO feeder link. In Section 3.3.1, it will be shown through numerical simulations that the interference term in (3.4) can be assumed to be spatially white. As a consequence, its autocorrelation matrix $\mathbf{R}_{\boldsymbol{\eta}_{\mathrm{I}}^{\nu}} \in \mathbb{C}^{K\times K}$ is diagonal. The diagonal entries associated to the l-th frequency channel are equal to the interference power $P_{\mathrm{I},l}^{\nu}$. The vector $\boldsymbol{\eta}_{\mathrm{T}}^{\nu} \in \mathbb{C}^{K\times 1}$ represents the thermal noise from the satellite payload. It contains realizations of zero-mean circularly symmetric complex Gaussian random variables, and its autocorrelation matrix is the diagonal matrix $\mathbf{R}_{\boldsymbol{\eta}_{\mathrm{T}}^{\nu}} \in \mathbb{C}^{K\times K}$. The diagonal entries of $\mathbf{R}_{\boldsymbol{\eta}_{\mathrm{T}}^{\nu}}$ associated to the thermal noise contributions for the l-th carrier frequency are equal and given by $P_{\mathrm{T},l}^{\nu}$.

Finally, if a digital transparent payload is considered, the received symbols from $\mathbf{y}^{\nu}$ can be post-processed in the satellite. This on-board processing is represented by the matrix $\mathbf{W}^{\nu} \in \mathbb{C}^{K\times K}$ such that the symbols obtained at the output of the processor are given by:

$$\mathbf{z}^{\nu} = \begin{bmatrix} z_1^{\nu} \\ \vdots \\ z_K^{\nu} \end{bmatrix} = \left(\mathbf{W}^{\nu}\right)^{\mathrm{H}} \mathbf{y}^{\nu} \ . \tag{3.5}$$

Here, the objective will be to null the spatial interference between the different data streams transmitted through the MIMO feeder link. Therefore, the pre-processing and the post-processing will be designed under a zero-forcing (ZF) constraint. According to the strategy adopted in the downlink and the payload architecture, further digital processing may be applied to $\mathbf{z}^{\nu}$ but this is out of the scope of this work. However, we recall that the design of a V/HTS system using the MIMO LOS concept both in its feeder links and its user links is for example possible [84].

3.2 Signal Processing

In the following, the design of the processing performed in the gateway antenna arrays and in the satellite payload is discussed. Since the considered strategies require the knowledge of the CSI, a possible CSI acquisition scheme is first shortly reviewed. Both a ground-limited processing and a joint ground/on-board processing approach based on the ZF criterion are then introduced to ensure a reliable transmission of the data symbols.

3.2.1 Channel State Information

In the ν-th feeder link, the matrix $\bar{\mathbf{H}}^{\nu\nu}$ has to be estimated i.e., the amplitude and the phase of the channel coefficients have to be determined. As already emphasized in Chapter 2, the differential phase rotation of the coefficients due to the motion of the satellite must also be evaluated to avoid the use of outdated CSI[1]. Similar challenges are encountered in the context of ground-based beamforming for multibeam satellites [124] or coherent uplink arraying [89]. In such scenarios, an accurate calibration of the uplink frequency channels is indeed needed. Even though CSI will be exploited differently in the proposed MIMO feeder link architecture, existing channel sounding strategies can be applied to the estimation of the matrix $\bar{\mathbf{H}}^{\nu\nu}$. A solution consists for example in the transmission within the uplink frequency spectrum of calibration

[1]It has to be noted that, in the case where the signal processing is done jointly on several frequency channels, the differential phase shift between the frequency channels should be compensated as well.

signals from the satellite. Different types of waveforms can be used for this purpose (e.g., pseudo-noise sequences, single tone carriers in the guard bands, ...) [125]. In the proof-of-concept of MIMO LOS for satellite communications of [52], constant amplitude zero autocorrelation (CAZAC) sequences and a best linear unbiased estimator (BLUE) have been used to determine the channel state with a minimum estimation error variance. The capacity obtained with the measured MIMO channel was perfectly complying with the results predicted by theory. The interested reader is also referred to the research works that have especially been conducted in the last years by NASA to enable coherent uplink arraying with a real-time estimation and compensation of atmospheric impairments [89]. First tests with commercial off-the-shelf (COTS) equipment have proved the ability of such systems to reach close-to-optimum performance. An abstract view of a potential CSI acquisition scheme for the proposed

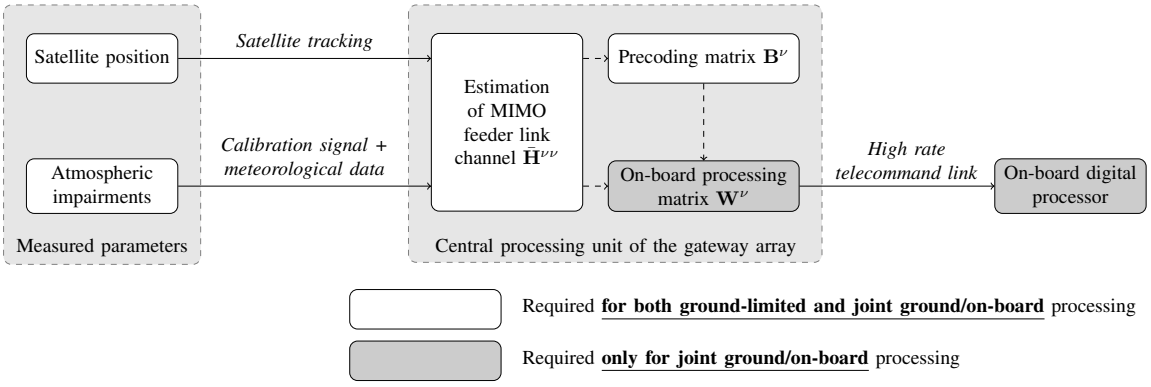

Figure 3-2: CSI acquisition scheme for MIMO feeder links

MIMO feeder link system is shown in Fig. 3-2. After the estimation of the MIMO channel $\bar{\mathbf{H}}^{\nu\nu}$, the precoding and on-board processing matrices $\mathbf{B}^{\nu}$ and $\mathbf{W}^{\nu}$ can both be computed in the central processing unit of the gateway antenna array. The on-board processing matrix is then transferred to the satellite through a high-speed payload configuration link. Future V/HTS systems will support telecommand connections with low latency requirements to control in quasi real-time the digital payload [126].

3.2.2 Ground-Limited Processing

With a ground-limited solution, the on-board processing matrix is set to the identity matrix, and only the precoder $\mathbf{B}^{\nu}$ is optimized. Based on the block-diagonal structure of the MIMO feeder link channel matrix, the ZF condition that must be fulfilled is formulated as [127]:

$$\bar{\mathbf{H}}^{\nu\nu}\mathbf{B}^{\nu} = \operatorname{diag}\left\{\sqrt{\mu_1^{\nu}}\cdot\mathbf{I}_2,\ldots,\sqrt{\mu_L^{\nu}}\cdot\mathbf{I}_2\right\}\ , \tag{3.6}$$

where μ_l^{ν}, $1\leq l\leq L$, are non-negative numbers. This constraint guarantees that the two parallel MIMO subchannels that are available for each uplink carrier frequency have equal amplitude gains. The precoder $\mathbf{B}^{\nu}$ satisfying (3.6) is given by:

$$\mathbf{B}^{\nu} = \operatorname{diag}\left\{\sqrt{\mu_1^{\nu}}\cdot\mathbf{H}_1^{\nu\nu,+},\ldots,\sqrt{\mu_L^{\nu}}\cdot\mathbf{H}_L^{\nu\nu,+}\right\}\ . \tag{3.7}$$

The matrix $\mathbf{H}_l^{\nu\nu,+}$ stands for the inverse of $\mathbf{H}_l^{\nu\nu}$, and the coefficients μ_l^{ν} are determined to satisfy the power constraint in (3.2) as an equality for at least one of the gateway antenna. They are thus obtained as:

$$\mu_l^{\nu} = \frac{P_{\mathrm{u},l}^{\nu}}{\max\limits_{n}\left[\mathbf{H}_l^{\nu\nu,+}\cdot\left(\mathbf{H}_l^{\nu\nu,+}\right)^{\mathrm{H}}\right]_{n,n}}\ . \tag{3.8}$$

The effective uplink CINR for the k-th data sequence follows as:

$$\rho_{\mathrm{u},k}^{\nu} = \frac{\mu_{\lceil\frac{k}{2}\rceil}^{\nu}}{P_{\mathrm{I},\lceil\frac{k}{2}\rceil}^{\nu}+P_{\mathrm{T},\lceil\frac{k}{2}\rceil}^{\nu}}\ . \tag{3.9}$$

Since the data sequences are not guaranteed to experience the same effective uplink CINR, the performance will be characterized in the simulation results with the help of the minimum CINR among all data streams $\rho_{\mathrm{u}}^{\nu} = \min\limits_{k}\rho_{\mathrm{u},k}^{\nu}$.

With ground-limited processing, the power allocation in the gateways is influenced

by the tropospheric attenuations. It can indeed be shown that:

$$\left[\mathbf{B}_l^{\nu}\left(\mathbf{B}_l^{\nu}\right)^{\mathrm{H}}\right]_{n,n} = \min\left\{\left(\frac{\alpha_1^{\nu}}{\alpha_2^{\nu}}\right)^{2(-1)^n}, 1\right\} \cdot P_{\mathrm{u},l}^{\nu} \,. \tag{3.10}$$

As detailed in Chapter 2, the variables α_1^{ν} and α_2^{ν} are the amplitude attenuations due to the troposphere for the first and the second gateway antenna, respectively. The result from (3.10) is demonstrated in Appendix A. It implies that, if the gateway antenna 1 (or 2) experiences better weather conditions than the gateway antenna 2 (or 1) i.e., $\alpha_1^{\nu} > \alpha_2^{\nu}$ (or $\alpha_2^{\nu} > \alpha_1^{\nu}$), it uses only $\left(\frac{\alpha_2^{\nu}}{\alpha_1^{\nu}}\right)^2 \cdot 100\%$ (or $\left(\frac{\alpha_1^{\nu}}{\alpha_2^{\nu}}\right)^2 \cdot 100\%$) of its available power. The gateway with the worse attenuation, on the other hand, fully exploits its available power. A direct consequence of this power allocation is that, if $\tilde{\rho}_{\mathrm{u},k}^{\nu}$ is the effective CINR in clear-sky conditions, the following relation is fulfilled:

$$\rho_{\mathrm{u},k}^{\nu} = \min\left\{\left(\alpha_1^{\nu}\right)^2, \left(\alpha_2^{\nu}\right)^2\right\} \cdot \tilde{\rho}_{\mathrm{u},k}^{\nu} \,. \tag{3.11}$$

In other words, the effective CINR degradation is equal to the maximum of the tropospheric attenuations experienced by the gateway antennas. The impact of this CINR reduction on the outage probability of a feeder link using the ground-limited processing strategy will be analyzed in Chapter 4.

3.2.3 Joint Ground/On-Board Processing

An improved robustness against weather attenuations can be expected if a post-processing of the signals is performed on-board the satellite. For this purpose, the precoder $\mathbf{B}^{\nu}$ and the on-board processing matrix $\mathbf{W}^{\nu}$ are jointly optimized using a Max-Min CINR fairness strategy under a ZF constraint i.e., $\left(\mathbf{W}^{\nu}\right)^{\mathrm{H}} \bar{\mathbf{H}}^{\nu\nu} \mathbf{B}^{\nu} = \mathbf{I}_L$. With this constraint, the effective uplink CINR for the k-th data sequence is expressed as:

$$\rho_{\mathrm{u},k}^{\nu} = \left[\left(\mathbf{w}_k^{\nu}\right)^{\mathrm{H}} \left(\mathbf{R}_{\boldsymbol{\eta}_{\mathrm{I}}^{\nu}} + \mathbf{R}_{\boldsymbol{\eta}_{\mathrm{T}}^{\nu}}\right) \mathbf{w}_k^{\nu}\right]^{+} \,, \tag{3.12}$$

where $\mathbf{w}_k^\nu$ is the k-th column of $\mathbf{W}^\nu$. The optimization problem to be solved is then formulated as:

$$\begin{aligned} \max_{\mathbf{B}^\nu, \mathbf{W}^\nu} \quad & \min_k \ \rho_{\mathrm{u},k}^\nu \\ \text{s.t.} \quad & \mathbf{B}^\nu \left(\mathbf{B}^\nu\right)^{\mathrm{H}} \leq \operatorname{diag}\left\{P_{\mathrm{u},1}^\nu \mathbf{I}_2, \ldots, P_{\mathrm{u},L}^\nu \mathbf{I}_2\right\} = \mathbf{P}^\nu \\ & \left(\mathbf{W}^\nu\right)^{\mathrm{H}} \bar{\mathbf{H}}^{\nu\nu} \mathbf{B}^\nu = \mathbf{I}_L \ . \end{aligned} \tag{3.13}$$

The power constraint in (3.13) enables to limit the diagonal elements of $\mathbf{B}^\nu \left(\mathbf{B}^\nu\right)^{\mathrm{H}}$ as expected from the condition in (3.2). The diagonal matrix $\mathbf{P}^\nu$ is one solution from an infinite set of matrices that can be used to upper bound $\mathbf{B}^\nu \left(\mathbf{B}^\nu\right)^{\mathrm{H}}$ [128].

The optimization of $\mathbf{B}^\nu$ and $\mathbf{W}^\nu$ according to (3.13) can be done using convex optimization tools [129]. Two block diagonal matrices $\mathbf{V}^\nu \in \mathbb{C}^{K\times K}$ and $\mathbf{\Gamma}^\nu \in \mathbb{R}^{K\times K}$ are defined to formulate a closed-form solution. These matrices are expressed as:

$$\mathbf{V}^\nu = \operatorname{diag}\left\{\mathbf{V}_1^\nu, \ldots, \mathbf{V}_L^\nu\right\} \ , \qquad \mathbf{\Gamma}^\nu = \operatorname{diag}\left\{\mathbf{\Gamma}_1^\nu, \ldots, \mathbf{\Gamma}_L^\nu\right\} \ , \tag{3.14}$$

with $\mathbf{V}_l^\nu \in \mathbb{C}^{2\times 2}$ and $\mathbf{\Gamma}_l^\nu \in \mathbb{R}^{2\times 2}$, $1 \leq l \leq L$, the matrices of eigenvectors and eigenvalues of $\left(\mathbf{H}_l^{\nu\nu}\right)^{\mathrm{H}} \mathbf{H}_l^{\nu\nu}$ such that:

$$\left(\mathbf{H}_l^{\nu\nu}\right)^{\mathrm{H}} \mathbf{H}_l^{\nu\nu} = \mathbf{V}_l^\nu \mathbf{\Gamma}_l^\nu \left(\mathbf{V}_l^\nu\right)^{\mathrm{H}} = \mathbf{V}_l^\nu \begin{bmatrix} \gamma_{l,1}^\nu & 0 \\ 0 & \gamma_{l,2}^\nu \end{bmatrix} \left(\mathbf{V}_l^\nu\right)^{\mathrm{H}} \ . \tag{3.15}$$

The eigenvalues $\gamma_{l,1}^\nu$ and $\gamma_{l,2}^\nu$ correspond to the gains of the MIMO eigenmodes at frequency $f_{\mathrm{c},l}$. When no rain attenuation impairs the signals, an antenna arrangement allowing a maximization of the data rate in $\mathbf{H}_l^{\nu\nu}$ is such that $\gamma_{l,1}^\nu = \gamma_{l,2}^\nu$ [38]. Relying on the definition of the matrix $\mathbf{V}^\nu$, an optimal solution to (3.13) is given by:

$$\mathbf{B}^\nu = \mathbf{P}^{\nu,\frac{1}{2}} \mathbf{V}^\nu \mathbf{\Omega} \ , \qquad \left(\mathbf{W}^\nu\right)^{\mathrm{H}} = \left(\bar{\mathbf{H}}^{\nu\nu} \mathbf{B}^\nu\right)^+ \ , \tag{3.16}$$

where $\mathbf{\Omega} \in \mathbb{C}^{K\times K}$ is the unitary discrete Fourier transform (DFT) matrix, and the diagonal matrix $\mathbf{P}^{\nu,\frac{1}{2}}$ contains the square roots of the entries of $\mathbf{P}^\nu$. The mathematical

reasoning used to obtain the solutions in (3.16) is provided in Appendix B.1. It has to be noted that $\mathbf{B}^{\nu}\left(\mathbf{B}^{\nu}\right)^{\mathrm{H}} = \mathbf{P}^{\nu}$ which implies that, contrary to the ground-limited processing approach, the maximum available power is always exploited.

Introducing the optimal solution from (3.16) in the cost function of (3.13), it appears that the effective uplink CINR is equal for all data streams and writes as:

$$\rho_{\mathrm{u},k}^{\nu} = K \cdot \left\{ \sum_{l=1}^{L} \frac{P_{\mathrm{T},l}^{\nu} + P_{\mathrm{I},l}^{\nu}}{P_{\mathrm{u},l}^{\nu}} \cdot \left(\frac{1}{\gamma_{l,1}^{\nu}} + \frac{1}{\gamma_{l,2}^{\nu}} \right) \right\}^{+} . \tag{3.17}$$

It can also be expressed as a function of the CINR in clear-sky conditions $\tilde{\rho}_{\mathrm{u}}^{\nu}$ as follows:

$$\rho_{\mathrm{u},k}^{\nu} = 2 \cdot \frac{\left(\alpha_1^{\nu}\alpha_2^{\nu}\right)^2}{\left(\alpha_1^{\nu}\right)^2 + \left(\alpha_2^{\nu}\right)^2} \cdot \tilde{\rho}_{\mathrm{u}}^{\nu} \geq \min\left\{ \left(\alpha_1^{\nu}\right)^2, \left(\alpha_2^{\nu}\right)^2 \right\} \cdot \tilde{\rho}_{\mathrm{u}}^{\nu} . \tag{3.18}$$

This result is demonstrated in Appendix B.2. It shows that the effective uplink CINR loss is always lower or equal than the maximum of the weather attenuations experienced by the gateway antennas.

3.3 System Analysis

A system analysis is now conducted to emphasize the fundamental trade-offs required for an effective design of MIMO feeder links. First, the interference is analyzed in order to validate the model from Section 3. The antenna arrangement that can be accepted in a practical system and the impact of tropospheric attenuations on the achievable uplink CINR are then discussed.

3.3.1 Interference

In this section, the spatial correlation of the interference and the carrier to interference ratio (CIR) are analyzed based on the transmission chain model introduced in Section 3.1. Results will be provided for a satellite at 9° E and gateways installed in Europe. The deployment scenario is the same as the one that was shown in Fig. 2-1c in Chapter 2. For the sake of convenience, this illustration is displayed again in Fig. 3-3.

A total of 15 MIMO feeder links is considered, and the parameters $d_{\mathrm{S}} = 3\,\mathrm{m}$, $\delta_{\mathrm{E}} = 0°$

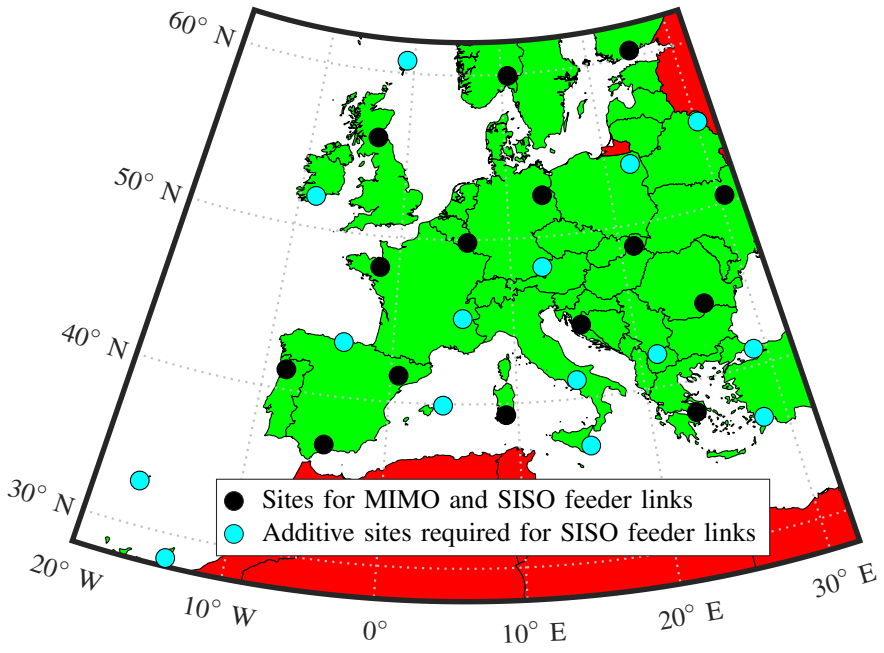

Figure 3-3: Deployment of the feeder links in Europe

and $d_{\mathrm{E}} = 40\,\mathrm{km}$ are used for all the links. It will be shown in Section 3.3.2 that this is an antenna arrangement that provides a close to maximum effective CINR for a Q/V-band link. The diameter of the receive antennas is set to $\Delta_{\mathrm{a}} = 1.4\,\mathrm{m}$, and their edge taper equals $T_{\mathrm{e}} = 12\,\mathrm{dB}$. The transmit power per frequency channel is equal for all gateway antennas in the system i.e., $P^{\nu}_{\mathrm{u},l} = P_{\mathrm{u},l}$, $1 \leq \nu \leq N$. Clear-sky conditions are assumed at all sites, and simulations have been run for links with ground-limited processing (Ground-P) and with joint ground/on-board processing (Joint-P). A scenario with 30 SISO feeder links and identical antenna characteristics is also considered to enable a CIR comparison between MIMO feeder links and the state-of-the-art. As already explained in Chapter 2, two gateway antennas per site are activated for the MIMO links whereas only one antenna per site is used in the case of SISO links.

The autocorrelation matrix $\mathbf{R}_{\boldsymbol{\eta}^{\nu}_{\mathrm{I}}}$ of the interference term from (3.4) is first analyzed for each MIMO feeder link to confirm the assumption made in Section 3.1 that it is a diagonal matrix. For this purpose, we observe that this matrix writes in its general

form as:

$$\mathbf{R}_{\boldsymbol{\eta}_{\mathrm{I}}^{\nu}} = \sum_{\substack{\nu'=1 \\ \nu' \neq \nu}}^{N} \bar{\mathbf{H}}^{\nu\nu'} \mathbf{B}^{\nu'} \left(\mathbf{B}^{\nu'}\right)^{\mathrm{H}} \left(\bar{\mathbf{H}}^{\nu\nu'}\right)^{\mathrm{H}} . \tag{3.19}$$

Obviously, $\mathbf{R}_{\boldsymbol{\eta}_{\mathrm{I}}^{\nu}}$ has at least a block diagonal structure. The matrix $\bar{\mathbf{H}}^{\nu\nu'}$ is indeed block diagonal whereas $\mathbf{B}^{\nu'}\left(\mathbf{B}^{\nu'}\right)^{\mathrm{H}}$ is block diagonal with ground-limited processing or simply diagonal with joint ground/on-board processing. Relying on this observation, $\mathbf{R}_{\boldsymbol{\eta}_{\mathrm{I}}^{\nu}}$ can be expressed as:

$$\mathbf{R}_{\boldsymbol{\eta}_{\mathrm{I}}^{\nu}} = \mathrm{diag}\left\{\mathbf{R}_{\mathrm{I},1}^{\nu}, \ldots, \mathbf{R}_{\mathrm{I},L}^{\nu}\right\} , \tag{3.20}$$

with $\mathbf{R}_{\mathrm{I},l}^{\nu}$ the 2×2 spatial correlation matrix of the interference signals in the l-th frequency channel of the ν-th feeder link. The level of spatial correlation can be characterized with the eigenvalue spread of $\mathbf{R}_{\mathrm{I},l}^{\nu}$. If $\lambda_{l,1}^{\nu}$ and $\lambda_{l,2}^{\nu}$ are the eigenvalues of $\mathbf{R}_{\mathrm{I},l}^{\nu}$ with $\lambda_{l,1}^{\nu} \geq \lambda_{l,2}^{\nu}$, the eigenvalue spread is defined as:

$$\chi_{l}^{\nu} = \frac{\lambda_{l,1}^{\nu}}{\lambda_{l,2}^{\nu}} . \tag{3.21}$$

A small χ_{l}^{ν} corresponds to a limited spatial correlation. On the other hand, a large χ_{l}^{ν} means that most of the interference power is concentrated on one eigendirection or, equivalently, that spatial correlation is important [130]. In Fig. 3-4, the distribution of the eigenvalue spreads in the considered Western Europe scenario is shown at the frequencies $f_{\mathrm{c}} = 43\,\mathrm{GHz}$ and $f_{\mathrm{c}} = 50\,\mathrm{GHz}$. It can be seen that, in all cases, half of the MIMO feeder links have an interference autocorrelation matrix whose eigenvalue spread is lower than 1.2 whereas the maximum value remains below 2.2. As a consequence, the approximation of always modeling the interference term in (3.4) as spatially white is accurate.

The CIR in the MIMO feeder links is now investigated and compared to a state-of-the-art SISO solution. The CIR $(C/I)_{l}^{\nu}$ in the ν-th MIMO feeder link at the l-th carrier frequency is defined as the ratio of the sum carrier to the sum interference

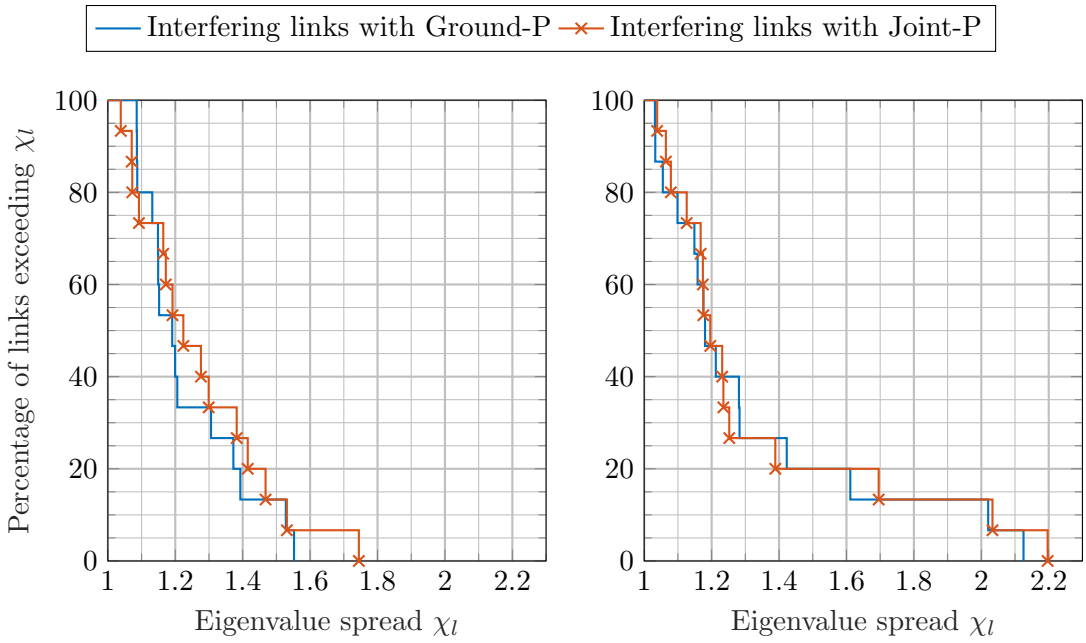

(a) $f_c = 43\,\text{GHz}$ (b) $f_c = 50\,\text{GHz}$

Figure 3-4: Percentage of links where the eigenvalue spread of the interference auto-correlation matrix exceeds a given value for $\Delta_a = 1.4\,\text{m}$ and $T_e = 12\,\text{dB}$

power such that:

$$(C/I)_l^{\nu} = \frac{\|\mathbf{H}_l^{\nu\nu}\mathbf{B}_l^{\nu}\|_F^2}{\sum_{\substack{\nu'=1 \\ \nu'\neq\nu}}^{N} \|\mathbf{H}_l^{\nu\nu'}\mathbf{B}_l^{\nu'}\|_F^2} \,. \tag{3.22}$$

In Fig. 3-5, the CIR distribution is shown for MIMO and SISO links, and non-negligible gains are observed with the proposed MIMO solution. Part of these gains are the consequence of the higher carrier power received in a MIMO feeder link due to the use of two gateway antennas. Moreover, better angular separations reduce the risk that the highest sidelobes or even the edge of the main lobe of a given link capture interference from a neighboring link. As a consequence, the interference power density in some SISO links can be significantly higher than in the case of MIMO links. This drawback is particularly obvious in Fig. 3-5a when comparing the lowest CIRs for the MIMO- and the SISO-based architectures. It should be noted that, in the specific scenario considered here, the deployment area for the SISO feeder links is larger than for the MIMO links. A few SISO deployment sites were indeed placed in remote locations (e.g. sites in Canary and Madeira Islands) to avoid a dramatic reduction of the CIR for some links. If the deployment region remains constrained to continental

Europe, the problem of beam isolation between the SISO links becomes critical. The superiority of MIMO feeder links is thus noticeable in this case.

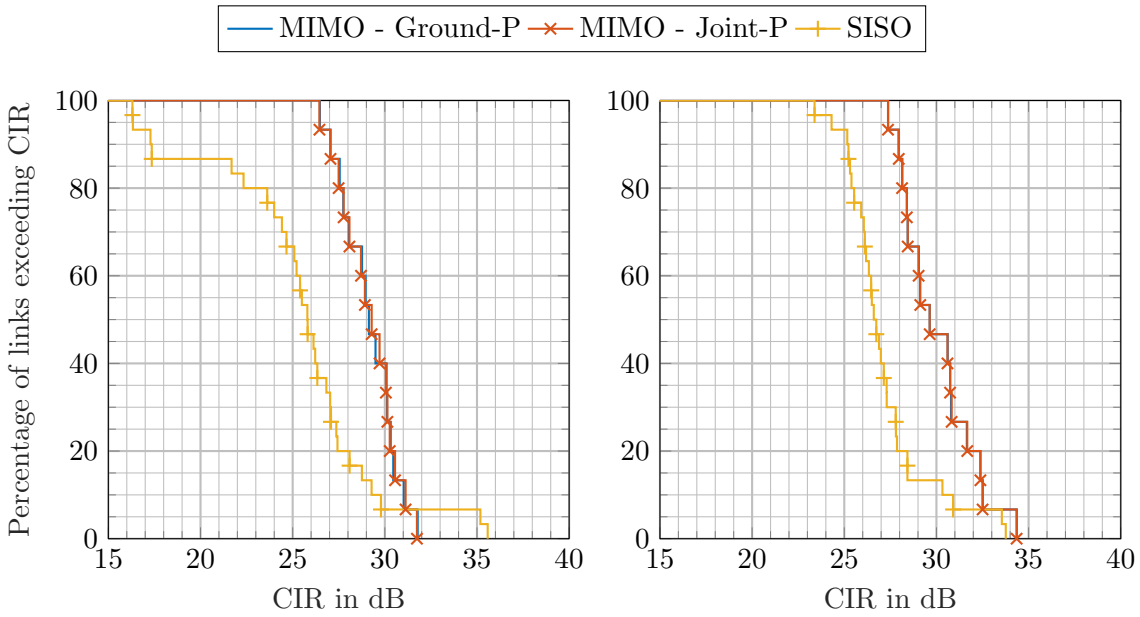

(a) $f_c = 43\,\text{GHz}$ (b) $f_c = 50\,\text{GHz}$

Figure 3-5: Percentage of links where the CIR exceeds a given value for $\Delta_a = 1.4\,\text{m}$ and $T_e = 12\,\text{dB}$

3.3.2 Antenna Arrangement and Weather

The influence of the antennas location, the satellite position and the weather attenuations on the effective uplink CINRs of MIMO links are now scrutinized. A scenario where both gateway antennas have clear-sky conditions i.e., $A_1 = A_2 = 0\,\text{dB}$, as well as a scenario where the first gateway antenna experiences a strong rain attenuation of $10\,\text{dB}$ i.e., $A_1 = 10\,\text{dB}$ and $A_2 = 0\,\text{dB}$, will be considered. A comparison with a state-of-the-art SISO feeder link will also be provided[2]. The parameters considered for the system dimensioning are summarized in Table 3.1. The same EIRP is used in each frequency channel. The miscellaneous losses for the MIMO links are $0.5\,\text{dB}$ higher than for SISO links to account for their higher receive depointing loss. In the

[2]For the benchmark SISO link, only the clear-sky CINR will be displayed in the figures since, in the case of a rain event, the resulting CINR is trivially obtained by subtracting the rain attenuation from the clear-sky CINR.

Table 3.1: Dimensioning of the feeder links

	SISO	***MIMO***
Frequency band	Ka (27.5-30 GHz) Q/V (42.5-43.5 & 47.2-50.2 GHz)	
Bandwidth per carrier	250 MHz	
EIRP per antenna and carrier (with back-off)	72.4 dBW	
Miscellaneous losses (depointing, etc...)	0.5 dB	1 dB
Rx antenna diameter	1.4 m	
Rx antenna efficiency	60 %	
Rx antenna separation	–	3 m
Noise temperature	600 K	
Interference power density	−142.59 dBW/MHz	

following results, this depointing loss is assumed to be constant for all the considered inter-antenna distances. We recall that, according to the results that were provided in Fig. 2-10, a penalty of 0.5 dB is a rather pessimistic assumption. Moreover, MIMO links are here not advantaged in terms of inter-link interference, and the same interference power density is assumed in both configurations. Unless otherwise mentioned, the satellite is again positioned at 9° E.

In Fig. 3-6a and Fig. 3-6b, the results for a Q/V-band system are shown as a function of the antenna separation d_{E} for two different locations (Luxembourg and Madrid). With $\delta_{\mathrm{E}} = 0°$, the maximum effective uplink CINR is reached for an antenna separation around 40 km. According to the analytical solution provided in [38], the optimal spacing for the carrier frequencies $f_{\mathrm{c},1} = 42.625$ GHz and $f_{\mathrm{c},L} = 50.075$ GHz and an antenna array located in Luxembourg equal 45 km and 38.2 km, respectively. It is hence obvious that a separation of 40 km offers a good compromise to obtain close to optimum MIMO links in all the frequency channels available in the Q/V-band. This nearly optimum separation is quasi-identical for all geographical positions in Europe. Moreover, a deviation of ±12.5 km can be accepted without entailing losses larger than 1.5 dB with ground-limited processing. When one of the antenna experiences a stronger rain fade than the other, the performance of ground-limited processing is more significantly affected than the joint ground/on-board processing scheme. A difference of 2.7 dB is observed between the two strategies for $A_1 = 10$ dB if $\delta_{\mathrm{E}} = 0°$

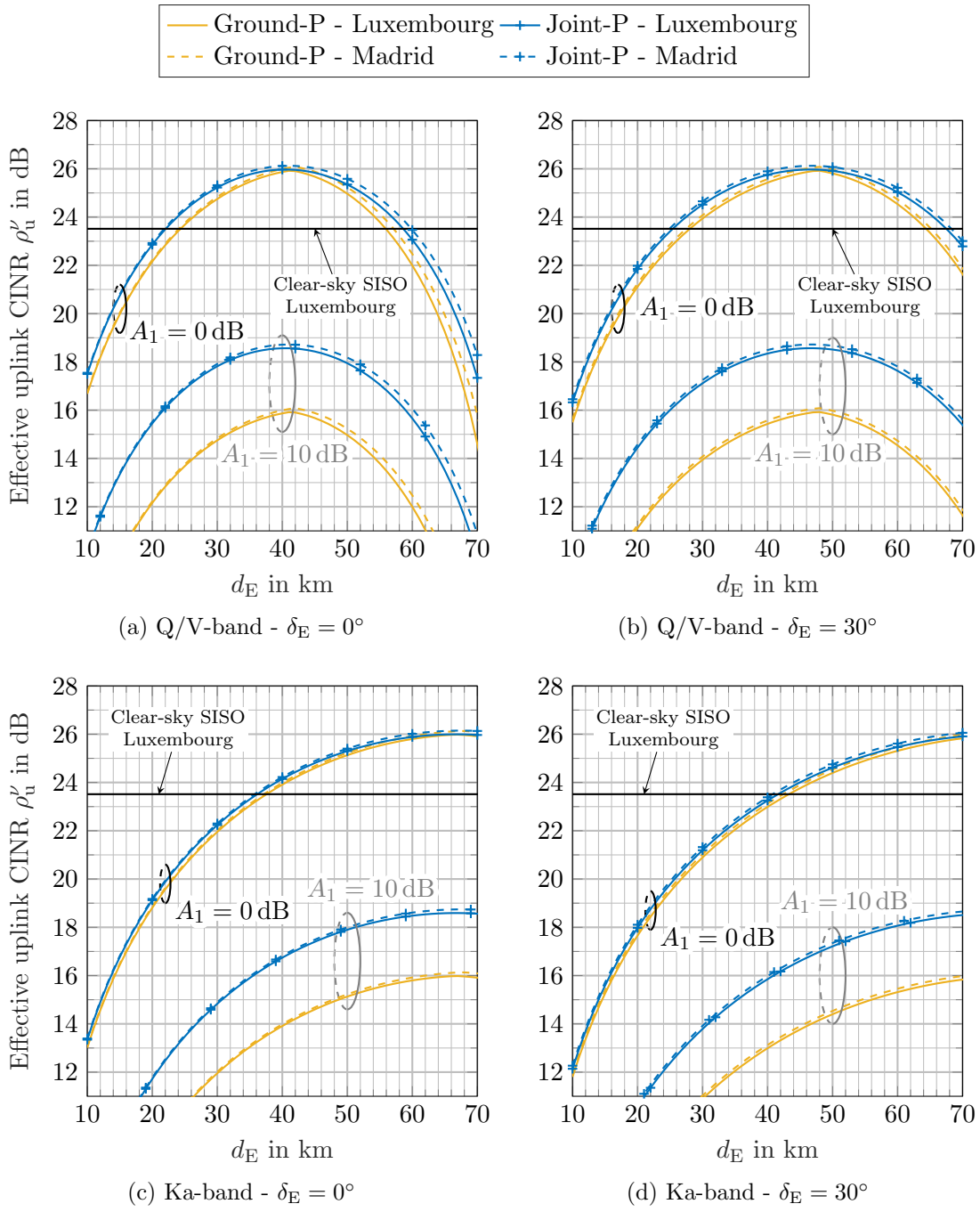

(a) Q/V-band - $\delta_E = 0°$

(b) Q/V-band - $\delta_E = 30°$

(c) Ka-band - $\delta_E = 0°$

(d) Ka-band - $\delta_E = 30°$

Figure 3-6: Effective uplink CINR as a function of d_E for $A_2 = 0$ dB and a satellite at 9° E

and $d_E = 40$ km. This observation is in accordance with the CINR losses predicted by (3.11) and (3.18). Similar conclusions can be drawn for $\delta_E = 30°$ except that, in this case, the optimal separation reaches 46 km. The optimal distance actually increases with δ_E and tends to infinity as δ_E tends to 90° [42]. For the Q/V-band system,

an orientation of up to $\delta_E = 35°$ can be allowed for an optimal antenna separation lower or equal to 50 km. A reduction of this optimal distance can be obtained by using a larger satellite antenna separation (e.g. $d_S = 4$ m instead of 3 m). However, this choice reduces the range of antenna distances for which the CINR degradation remains limited. Moreover, a smaller Earth antenna separation would entail a higher correlation between the rain fades at the gateway antennas. It will be emphasized in Chapter 4 that this stronger correlation impacts the system availability. Finally, since an operation of feeder links in both the Q/V- and the Ka-bands can sometimes be considered, results in the case of an exploitation of the system in the Ka-band is also provided in Fig. 3-6c and Fig. 3-6d. It comes out that, due to the lower carrier frequencies used, the optimal antenna separation for a Ka-band system is higher than for the Q/V-band system. Meanwhile, an exploitation in both frequency bands is principally possible since a region of antenna separations where a satisfactory CINR is observed in the Q/V- and the Ka-bands can be identified. In the case $\delta_E = 0°$, a separation around 50 km would for example be desired.

To put it in a nutshell, the results from Fig. 3-6 have shown that, for a given satellite orbital position, an antenna arrangement can be found to achieve a high effective uplink CINR with spatial multiplexing. The stability of the system performance for a large range of antenna separations and array orientations offers enough degrees of freedom for a satellite operator to deploy its ground stations as illustrated in Fig. 3-7. In this later figure, the eligible deployment areas for a second gateway antenna given that the first one is located in Luxembourg at 49.82° N 5.78° E are shown both for a Q/V-band and a Ka-band system. The distance between the two gateway antennas is constrained to a maximum of 60 km to avoid a too large receive depointing loss. Moreover, the CINR reduction due to an imperfect antenna positioning has been constrained to a maximum of 1.5 dB with ground-limited processing. For the Q/V-band system, two areas of 25 km in width and around 100 km in height can for example be identified on the map. It has also to be noted that part of these areas are eligible for an exploitation of the system in both the Ka- and the Q/V-band. These subareas are 8.9 km wide and reach a maximum of 80.3 km in height.

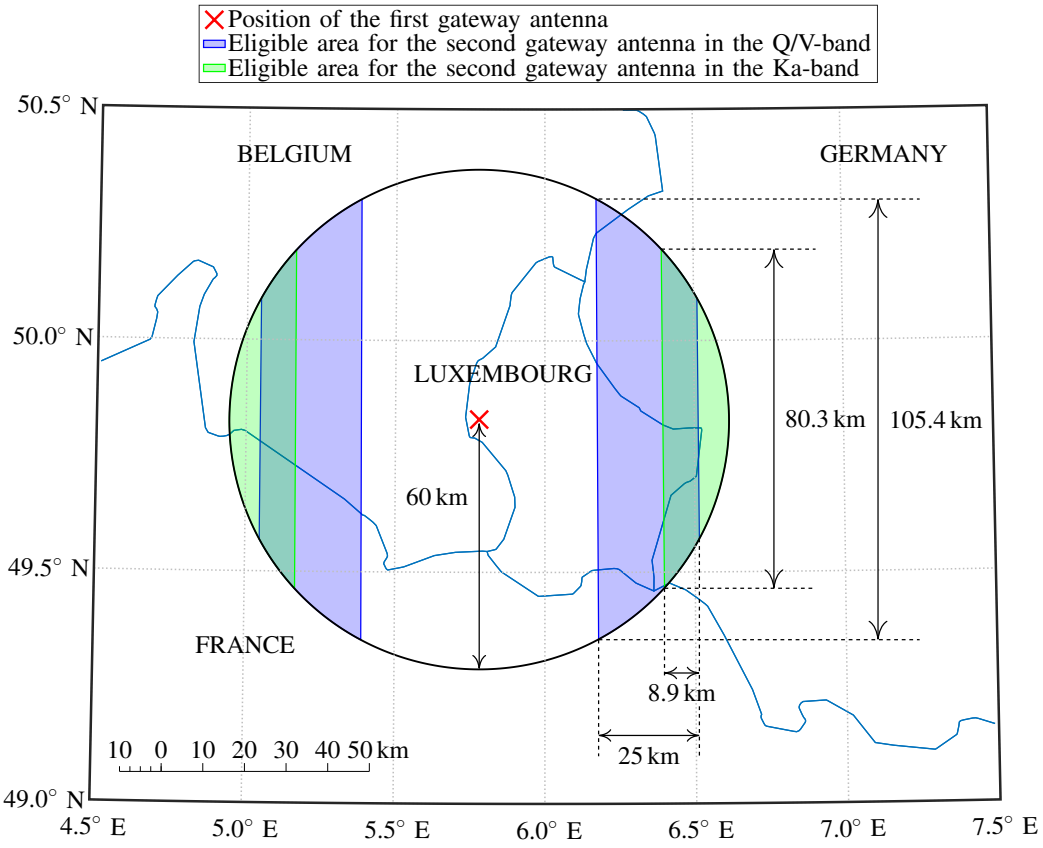

Figure 3-7: Possible locations for a second gateway antenna up to 60 km from a first antenna at 49.82° N 5.78° E and given that the CINR loss due to an imperfect antenna positioning should not exceed 1.5 dB with ground-limited processing

In practice, operators deploy ground facilities that deliver data to satellites on different orbital positions to maximize their return on investment. As a consequence, cost effective MIMO feeder links are only feasible if this can be ensured. To address this question, the effective uplink CINR of a Q/V-band system is shown in Fig. 3-8 as a function of the satellite orbital position for a gateway antenna array located in Luxembourg, $\delta_{\mathrm{E}} = 0°$, $d_{\mathrm{E}} = 40\,\mathrm{km}$ and $A_2 = 0\,\mathrm{dB}$. Here, the effective uplink CINR for the joint ground/on-board processing approach does not vary by more than 0.7 dB for a satellite longitude between 27° W and 39° E. A similar behavior would be obtained for other gateway locations in Europe. In a practical system design, the antenna arrangement on Earth should thus be optimized for the satellite position with subsatellite point at the center of the gateway antenna array. In this way, MIMO feeder links can be exploited for a large range of orbital positions if a standardized

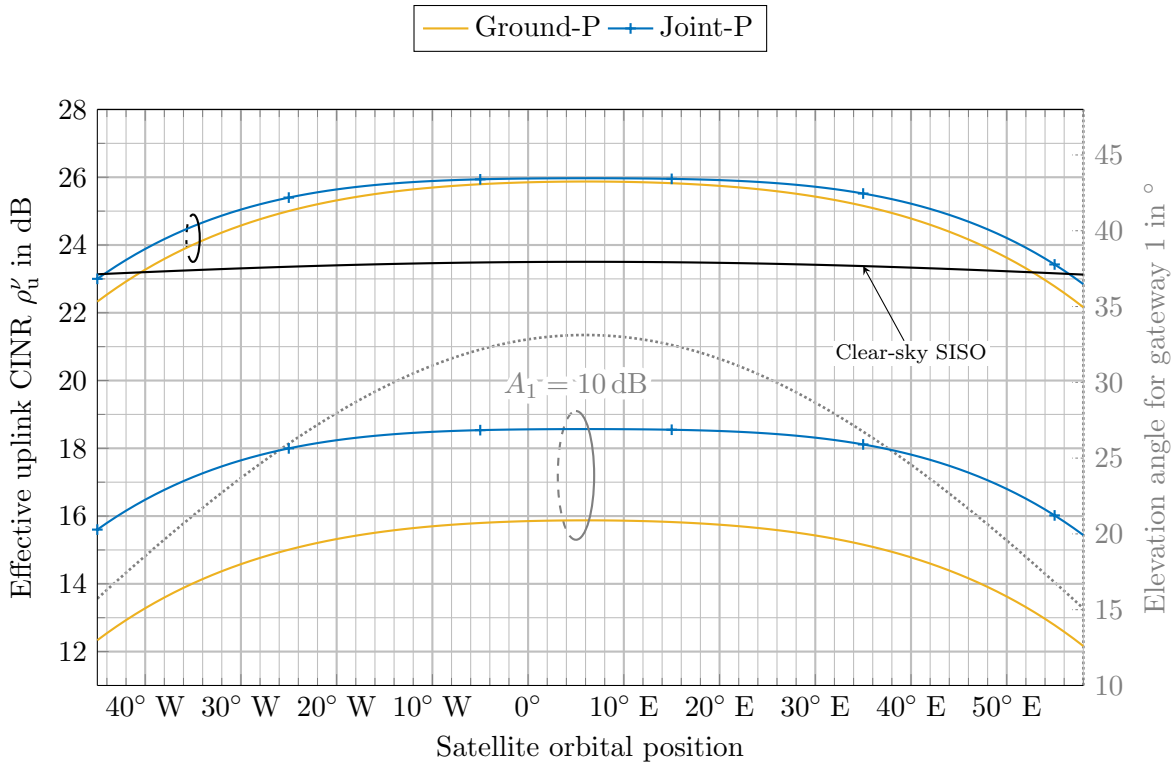

Figure 3-8: Effective uplink CINR of a Q/V-band system as a function of the satellite orbital position for a gateway array in Luxembourg, $\delta_E = 0°$, $d_E = 40\,\mathrm{km}$, $A_2 = 0\,\mathrm{dB}$

separation is used for the satellite receive antennas (3 m in our system design but up to 10 m are feasible today).

3.4 Summary and Future Works

MIMO transmission strategies with ground-limited and joint ground/on-board processing have been presented in this chapter. An interference analysis has shown that, with the considered transmission schemes, the interference between MIMO feeder links can reasonably be assumed spatially uncorrelated. Moreover, using the uplink CINR as a performance criterion, it has been enlightened that the inter-antenna distance and the array orientation of a feeder link can deviate from the optimal parameters without entailing strong degradations. Relying on this robustness against an imperfect antenna arrangement, it is even possible to design a MIMO feeder link operating in both the Ka- and the Q/V-band. Lastly, the presented results have also

shed light on the fact that the ground equipment of a MIMO feeder link can serve satellites on different orbital slots.

The research works reported in this chapter pave the way for further investigations on the following aspects:

CSI acquisition scheme: Possible strategies for the estimation of a MIMO feeder link channel (e.g., downlink beacon or loopback signal from uplink) should be thoroughly studied. In particular, the time and frequency resources required by the different approaches to obtain an accurate CSI should be assessed. Not only the tropospheric impairments but also the hardware imperfections (e.g., oscillators) must be taken into account for this analysis. To limit the aging effects, some tropospheric impairments could be predicted using weather data (e.g., fade slope).

Imperfect CSI: The efficiency of the MIMO processing strategies must be analyzed in the case where only an imperfect channel estimation is available. If necessary, more advanced schemes could be designed to limit the performance losses due to an inexact CSI. This study should be conducted in parallel with the design of the CSI acquisition scheme to find the optimal trade-off between the update rate and the accuracy of the CSI.

Finally, it has to be noted that, even though the transmit strategies considered in this chapter focused solely on the uplink, the preliminary evaluation of an end-to-end design relying on MIMO feeder links and a MU-MIMO downlink has also been provided in [84]. This paves the way for further research efforts on MIMO relaying schemes for V/HTS systems.

Chapter 4

Advanced Smart Diversity

Rain attenuation in the Ka- and in the Q/V-bands can reach more than 10 dB such that smart diversity strategies are required to ensure a sufficient availability. Other attenuation effects from clouds and gases remain, on the other hand, limited to a maximum of a few decibels and can be compensated by conventional uplink power control schemes. In this chapter, a rain attenuation prediction model is first introduced to enable an outage analysis of MIMO feeder links. An advanced smart diversity approach is also introduced to cope with heavy rain events at a system level. Numerical results emphasize the ability of a MIMO-based feeder link architecture to surpass SISO links in terms of availability.

4.1 Rain Attenuation Statistics

Under the assumption that all sources of tropospheric attenuation except rain are compensated by a control of the uplink power, only rainfalls can impact the CINR in a given feeder link. Therefore, the outage analysis performed in this chapter will resort to a prediction model of rain attenuation. Statistics for an average year are here considered. Accurate closed-form expressions can be obtained under the assumption that the long-term distribution of rain attenuation is log-normal. The probability that the rain attenuation A_n^ν at the n-th gateway antenna in the ν-th feeder link

exceeds a certain non-zero threshold a_n is defined as:

$$\mathrm{P}\left\{A_n^\nu \geq a_n\right\} = \mathrm{P}_n\left\{\mathrm{Rain}\right\} \cdot \mathrm{P}\left\{A_n^\nu \geq a_n \mid \mathrm{Rain}\right\} \ , \tag{4.1}$$

where $\mathrm{P}_n\left\{\mathrm{Rain}\right\}$ is the probability that it rains at the location of the considered antenna. It is obtained from the recommendation ITU-R P.837-7 [131]. Moreover, the conditional probability $\mathrm{P}\left\{A_n^\nu \geq a_n \mid \mathrm{Rain}\right\}$ represents the likelihood that $A_n^\nu \geq a_n$ if a rain event occurs. Following the recommendation ITU-R P.618-13 [96], it is determined as:

$$\mathrm{P}\left\{A_n^\nu \geq a_n \mid \mathrm{Rain}\right\} = \mathrm{Q}\left(\frac{\log\left(a_n\right) - \mu_{\log\left(A_n^\nu\right)}}{\sigma_{\log\left(A_n^\nu\right)}}\right) \tag{4.2}$$

with

$$\mathrm{Q}\left(x\right) = \frac{1}{\sqrt{2\pi}} \int_x^{+\infty} e^{-\frac{t^2}{2}}\, dt \ . \tag{4.3}$$

The variables $\mu_{\log\left(A_n^\nu\right)}$ and $\sigma_{\log\left(A_n^\nu\right)}$ are the mean and the variance of the random variable $\log\left(A_n^\nu\right)$, respectively. They are determined by performing a log-normal fit to the rain attenuation distribution. This distribution is obtained from the knowledge of the long-term rainfall rate statistics, the carrier frequency and the elevation angle of the antenna. Rainfall rate statistics from the map provided in [131] or from local measurements can be used. For the sake of illustration, the annual exceedance probability of rain attenuation for an antenna located in different European cities and pointing to a satellite at 9° E is shown in Fig. 4-1. Circular polarized waves and a carrier frequency of 50 GHz were assumed in this example. Obviously, the rain attenuation statistics can significantly vary according to the site selected for the antenna deployment. For example, a feeder link has a lower probability to experience strong rain fades if its ground equipment is installed in the region of Madrid rather than in Palma. This result sheds light on another advantage of MIMO feeder links. Instead of deploying spatially separated SISO feeder links in regions where rain attenuation statistics might not be favorable, gateway antennas can be clustered in sites where the probability of a deep rain fade is reduced. In the latter example, the choice would

be to install two antennas next to Madrid rather than one antenna in Madrid and one antenna in Palma.

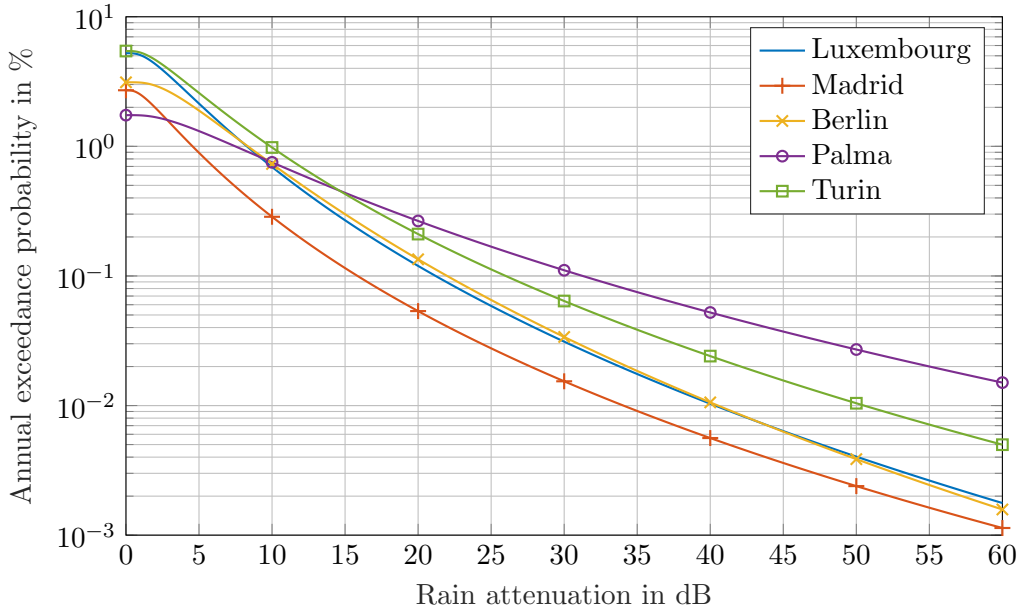

Figure 4-1: Annual exceedance probability of rain attenuation for an antenna in different European cities and pointing to a satellite at 9° E

An outage analysis of MIMO feeder links also requires the knowledge of the annual joint probability $\mathrm{P}\left\{A_1^\nu \geq a_1, A_2^\nu \geq a_2\right\}$ which is given by:

$$\mathrm{P}\left\{A_1^\nu \geq a_1, A_2^\nu \geq a_2\right\} = \ldots$$
$$\begin{cases} \mathrm{P}\left\{A_n^\nu \geq a_n\right\} & \text{if } a_n \geq 0,\ a_{n' \neq n} = 0 \\ \mathrm{P}_{1\&2}\left\{\text{Rain}\right\} \cdot \mathrm{P}\left\{A_1^\nu \geq a_1, A_2^\nu \geq a_2 \mid \text{Rain 1\&2}\right\} & \text{if } a_1 \geq 0,\ a_2 \geq 0. \end{cases} \tag{4.4}$$

$\mathrm{P}_{1\&2}\left\{\text{Rain}\right\}$ is the joint probability that rain events occur on the paths of both transmit antennas. Moreover, $\mathrm{P}\left\{A_1^\nu \geq a_1, A_2^\nu \geq a_2 \mid \text{Rain 1\&2}\right\}$ is the conditional joint probability that $A_1^\nu \geq a_1$ and $A_2^\nu \geq a_2$ if it is raining at both antenna locations. Following the recommendation ITU-R P.1815-1 [132], $\mathrm{P}_{1\&2}\left\{\text{Rain}\right\}$ is determined as:

$$\mathrm{P}_{1\&2}\left\{\text{Rain}\right\} = \frac{1}{2\pi\sqrt{1-\left(c_{\mathrm{R}}^\nu\right)^2}} \cdot \int_{R_1}^{+\infty}\int_{R_2}^{+\infty} \exp\left\{-\left(\frac{r_1^2 + r_2^2 - 2c_{\mathrm{R}}^\nu r_1 r_2}{2\left\{1-\left(c_{\mathrm{R}}^\nu\right)^2\right\}}\right)\right\} dr_1 dr_2\ , \tag{4.5}$$

with $R_n = \mathrm{Q}^{-1}\left\{\mathrm{P}_n\left\{\mathrm{Rain}\right\}\right\}$. The parameter c_{R}^{ν} is the correlation of the rain events in the ν-th feeder link and is obtained as:

$$c_{\mathrm{R}}^{\nu} = 0.7 \cdot \exp\left\{-\frac{d_{\mathrm{E}}^{\nu}}{60}\right\} + 0.3 \cdot \exp\left\{-\left(\frac{d_{\mathrm{E}}^{\nu}}{700}\right)^2\right\} . \tag{4.6}$$

The distance d_{E}^{ν} is in km. On the other hand, $\mathrm{P}\left\{A_1^{\nu} \geq a_1, A_2^{\nu} \geq a_2 \mid \text{Rain 1\&2}\right\}$ writes as:

$$\begin{aligned}\mathrm{P}\left\{A_1^{\nu} \geq a_1, A_2^{\nu} \geq a_2 \mid \text{Rain 1\&2}\right\} = \ldots \\ \frac{1}{2\pi\sqrt{1-\left(c_{\mathrm{A}}^{\nu}\right)^2}} \cdot \int_{U_1}^{+\infty}\int_{U_2}^{+\infty} \exp\left\{-\left(\frac{u_1^2+u_2^2-2c_{\mathrm{A}}^{\nu}u_1u_2}{2\left\{1-\left(c_{\mathrm{A}}^{\nu}\right)^2\right\}}\right)\right\} du_1 du_2 ,\end{aligned} \tag{4.7}$$

where

$$U_n = \frac{\log(a_n) - \mu_{\log(A_n^{\nu})}}{\sigma_{\log(A_n^{\nu})}} . \tag{4.8}$$

The correlation c_{A}^{ν} of the rain attenuations when both antennas experience a rain event is given by:

$$c_{\mathrm{A}}^{\nu} = 0.94 \cdot \exp\left\{-\frac{d_{\mathrm{E}}^{\nu}}{30}\right\} + 0.06 \cdot \exp\left\{-\left(\frac{d_{\mathrm{E}}^{\nu}}{500}\right)^2\right\} . \tag{4.9}$$

The value d_{E}^{ν} is again in km. The correlation values are shown in Fig. 4-2. It can be seen that, in a MIMO feeder link, the rain events are significantly correlated since, for antennas separated by up to 50 km, c_{R} is greater than 0.6. In other words, the probability that it rains in the transmission path of a gateway antenna is relatively high if the other antenna, which is distant by a few tens of kilometers, also experiences a rain fading. Meanwhile, the correlation c_{A} of the rain attenuation values decreases more steeply than c_{R}. It is only equal to 0.24 for an inter-antenna distance of 50 km. As a matter of fact, even though the probability that it simultaneously rains at both antennas is not negligible, the risk that the rain attenuations are equally strong remains limited. This is the reason why important diversity gains can be achieved with state-of-the-art single-site diversity schemes [80]. Meanwhile, single-site diversity is

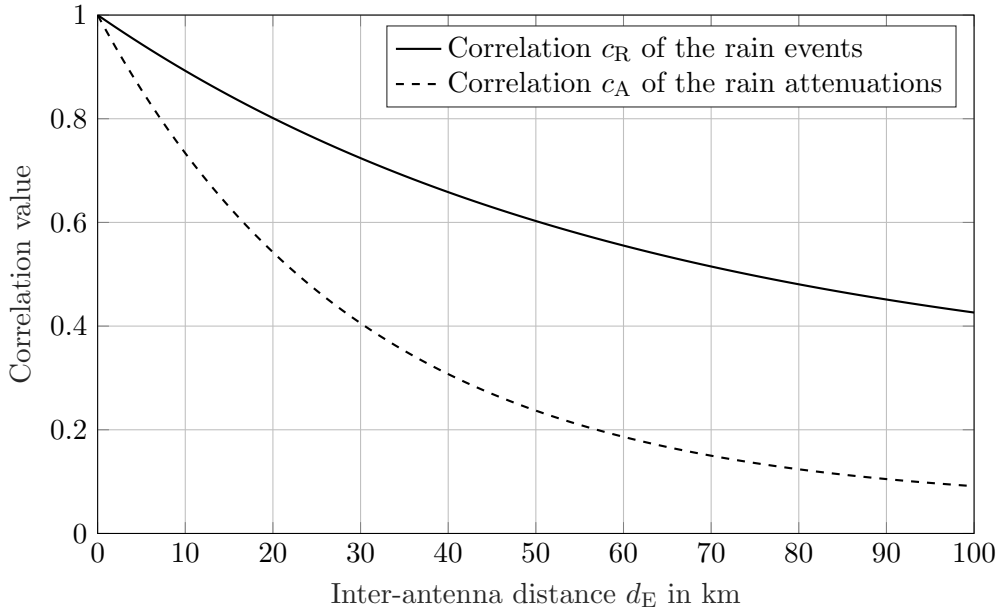

Figure 4-2: Correlation coefficients c_R and c_A as a function of the inter-antenna distance d_E

not cost-efficient since it only considers the activation of one of the antennas whereas the other stays idle. The redundant hardware is thus unused for most of the time. With the proposed MIMO feeder links, the antennas deployed in a given site can both be activated to enable spatial multiplexing. A diversity mode can also be used in case the rain attenuation for one of the gateway antennas is too strong to guarantee a sufficiently high effective CINR for spatially multiplexed data streams. This degraded operation mode is discussed in the following section.

4.2 Diversity Mode

A MIMO feeder link can be operated in a diversity mode when the effective uplink CINR with the spatial multiplexing mode becomes too low for a reliable transmission. Only the antenna with the smallest rain attenuation remains in this case operational, and a single data stream per frequency channel, instead of 2 with the MIMO approach, is transmitted. Obviously, no on-ground signal processing is required with this mode. On the other hand, on-board digital processing can be used to coherently

combine the signals received by the satellite antennas and, hence, achieve a diversity gain[1]. Whereas the MIMO channel for a given carrier frequency was modeled in Chapters 2 and 3 with a 2×2 matrix, a column vector is now sufficient to represent the propagation channel between the active gateway antenna and the two satellite reflectors. If the feeder link of index ν uses the diversity mode, its channel at time instant t and for carrier frequency f_c can be modeled in the equivalent baseband as:

$$\mathbf{h}_n^{\nu\nu}(t) = \begin{bmatrix} h_{1n}^{\nu\nu}(t) \\ h_{2n}^{\nu\nu}(t) \end{bmatrix} = \alpha_n^{\nu}(t) \cdot G_n(t) \cdot \begin{bmatrix} e^{j\frac{2\pi f_c}{c_0}\left\{r_{2n}^{\nu}(t) - r_{1n}^{\nu}(t)\right\}} \\ 1 \end{bmatrix} . \tag{4.10}$$

The index n is the index of the active gateway antenna in the considered link. The last term of (4.10) was obtained after some trivial manipulations using the expression of the channel coefficients provided in (2.30). In particular, $G_n(t)$ takes the tropospheric phase impairments, the antenna gains and the path loss[2] into account. It also includes the phase shift induced by the LOS signal propagation towards the second satellite antenna. We recall that $r_{1n}^{\nu}(t)$ and $r_{2n}^{\nu}(t)$ are the distances from the ground station to the first and the second satellite antenna, respectively. Even though the satellite moves in its station-keeping box, an analysis of the slant path geometry shows that the difference $r_{1n}^{\nu}(t) - r_{2n}^{\nu}(t)$ remains constant over time. This property is a consequence of the large distance between the gateway antenna and the satellite. Based on this characteristic, the uplink channel is finally expressed as:

$$\mathbf{h}_n^{\nu\nu}(t) = \alpha_n^{\nu}(t) \cdot G_n(t) \cdot \begin{bmatrix} e^{j\Delta\varphi} \\ 1 \end{bmatrix} , \tag{4.11}$$

where the time-invariant phase shift $\Delta\varphi$ can be determined from the slant path geometry assuming that the satellite is exactly at its desired orbital location. It clearly appears from (4.11) that a coherent combining of the received signals can be realized

[1]Diversity combining is not feasible with state-of-the-art SISO feeder links. As explained in Chapter 2, the same number of receive RF chains (feeds, low noise amplifiers, etc...) are required for MIMO-based and SISO-based architectures. However, with SISO links, each chain is dedicated to a different feeder link whereas MIMO links have one RF chain per reflector. These two chains can here be used as diversity branches.

[2]The approximation $\frac{c_0}{4\pi f_c r_{1n}^{\nu}(t)} \approx \frac{c_0}{4\pi f_c r_{2n}^{\nu}(t)}$ has been used.

in the on-board processor by first carrying out a phase correction of the first diversity branch with $e^{-j\Delta\varphi}$. To illustrate this, let's s_n^ν be a symbol to be transmitted with an EIRP of P_u^ν in the considered feeder link. Omitting the time indices for the sake of notational simplicity, the symbols received by the satellite antennas are given by[3]:

$$\mathbf{y}^\nu = \mathbf{h}_n^{\nu\nu} \cdot s_n^\nu + \boldsymbol{\eta}_\mathrm{I}^\nu + \boldsymbol{\eta}_\mathrm{I}^\nu \ . \tag{4.12}$$

Similarly to (3.4), $\boldsymbol{\eta}_\mathrm{I}^\nu \in \mathbb{C}^{2\times 1}$ and $\boldsymbol{\eta}_\mathrm{T}^\nu \in \mathbb{C}^{2\times 1}$ represent the interference from adjacent feeder links and the thermal noise. Again, these impairments are spatially uncorrelated. The diagonal elements of their autocorrelation matrices are equal to P_I^ν and P_T^ν, respectively. In the on-board processor, diversity combining is performed such that the following symbol is obtained:

$$z^\nu = \left(\mathbf{w}^\nu\right)^\mathrm{H} \mathbf{y}^\nu = 2 \cdot \alpha_n^\nu \cdot G_n \cdot s_n^\nu + \left(\mathbf{w}^\nu\right)^\mathrm{H} \boldsymbol{\eta}_\mathrm{I}^\nu + \left(\mathbf{w}^\nu\right)^\mathrm{H} \boldsymbol{\eta}_\mathrm{I}^\nu \ , \tag{4.13}$$

with $\mathbf{w}^\nu = \begin{bmatrix} e^{j\Delta\varphi} & 1 \end{bmatrix}^\mathrm{T}$. As a consequence, the effective uplink CINR with the diversity mode writes as:

$$\rho_\mathrm{u}^\nu = 2 \cdot \left(\alpha_n^\nu\right)^2 \cdot |G_n|^2 \cdot \frac{P_\mathrm{u}^\nu}{P_\mathrm{I}^\nu + P_\mathrm{T}^\nu} = \left(\alpha_n^\nu\right)^2 \cdot \tilde{\rho}_\mathrm{u}^\nu \ . \tag{4.14}$$

The constant $\tilde{\rho}_\mathrm{u}^\nu$ is the uplink CINR achieved if the active antenna experiences clear-sky conditions.

4.3 Link-Level Outage Analysis

With the knowledge of the rain attenuation statistics, the outage probability of a single MIMO feeder link i.e., the probability that the effective uplink CINR is below a given threshold, can be determined. The outage probability is actually different according to the transmission scheme used to operate the link. As a consequence, an

[3]Contrary to the MIMO approach, the performance of the diversity mode will not be influenced by the frequency-dependent phase relationships between the LOS channel coefficients. Thus, given a fixed link budget, its performance can be analyzed for an arbitrary carrier frequency f_c.

expression for the outage probability of the spatial multiplexing modes with ground-limited processing and joint ground/on-board processing introduced in Chapter 3 as well as the diversity mode from Section 4.2 are provided in the following. In the numerical results, these outage probabilities are compared to the outage probability of a state-of-the-art SISO link.

4.3.1 Outage Probabilities

If ρ_{o} is the outage CINR, the outage probability in the ν-th link $\mathrm{P}\left\{\rho_{\mathrm{u}}^{\nu} \leq \rho_{\mathrm{o}}\right\}$ is obtained from the definition, for each of the considered scheme, of the effective uplink CINR ρ_{u}^{ν} as a function of the clear-sky uplink CINR $\tilde{\rho}_{\mathrm{u}}^{\nu}$ and the rain fading values α_1^{ν} and α_2^{ν}. For spatial multiplexing with ground-limited processing (Ground-P) and joint ground/on-board processing (Joint-P), these expressions were provided in (3.11) and (3.18), respectively. Moreover, the result for the diversity mode is given in (4.14) in the previous section.

Multiplexing Mode - Ground-P

With ground-limited processing, the CINR loss due to rain is equal to the maximum of the attenuation values experienced by the gateway antennas. In this case, the outage probability is expressed as:

$$\mathrm{P}\left\{\rho_{\mathrm{u}}^{\nu} \leq \rho_{\mathrm{o}}\right\} = \mathrm{P}\left\{A_1^{\nu} \geq A_{\mathrm{lb}}^{\nu}\right\} + \mathrm{P}\left\{A_2^{\nu} \geq A_{\mathrm{lb}}^{\nu}\right\} - \mathrm{P}\left\{A_1^{\nu} \geq A_{\mathrm{lb}}^{\nu}, A_2^{\nu} \geq A_{\mathrm{lb}}^{\nu}\right\} \ , \quad (4.15)$$

with $A_{\mathrm{lb}}^{\nu} = \min\left\{ A \mid 10^{-\frac{A}{10}} \cdot \tilde{\rho}_{\mathrm{u}}^{\nu} \leq \rho_{\mathrm{o}} \right\}$. The expression of $\mathrm{P}\left\{\rho_{\mathrm{u}}^{\nu} \leq \rho_{\mathrm{o}}\right\}$ takes into account the fact that the events $A_1^{\nu} \geq A_{\mathrm{lb}}^{\nu}$ and $A_2^{\nu} \geq A_{\mathrm{lb}}^{\nu}$ are not mutually exclusive events due to the correlation existing between the rain attenuations at the first and at the second gateway antenna.

Multiplexing Mode - Joint-P

The determination of the outage probability for the joint processing approach is more complex than in the case of ground-limited processing. In fact, as observed in

(3.18), the CINR loss is not simply equal to the maximum of the rain attenuations anymore. Here, the outage region has to be defined in a more general way as $\mathcal{A}_{\mathrm{o}}^{\nu} = \left\{ (A_1^{\nu}, A_2^{\nu}) \in \mathbb{R}_{\geq 0}^2 \mid \rho_{\mathrm{u}}^{\nu} \leq \rho_{\mathrm{o}} \right\}$. Based on the fact that, if A_2^{ν} (or A_1^{ν}) is fixed, an increase of A_1^{ν} (or A_2^{ν}) leads to a reduction of the CINR, the outage probability computes as:

$$\mathrm{P}\left\{\rho_{\mathrm{u}}^{\nu} \leq \rho_{\mathrm{o}}\right\} = \lim_{\zeta \to 0} \sum_{q=1}^{+\infty} \left[\mathrm{P}\left\{ A_1^{\nu} \geq A_{\mathrm{lb},q}^{\nu}, A_2^{\nu} \geq A_{2,q}^{\nu} - \frac{\zeta}{2} \right\} - \mathrm{P}\left\{ A_1^{\nu} \geq A_{\mathrm{lb},q}^{\nu}, A_2^{\nu} \geq A_{2,q}^{\nu} + \frac{\zeta}{2} \right\} \right], \quad (4.16)$$

with $A_{2,q}^{\nu} = (q-1) \cdot \zeta$ and $A_{\mathrm{lb},q}^{\nu} = \min\left\{ A_1^{\nu} \mid \left(A_1^{\nu}, A_{2,q}^{\nu}\right) \in \mathcal{A}_{\mathrm{o}}^{\nu} \right\}$. The method, which

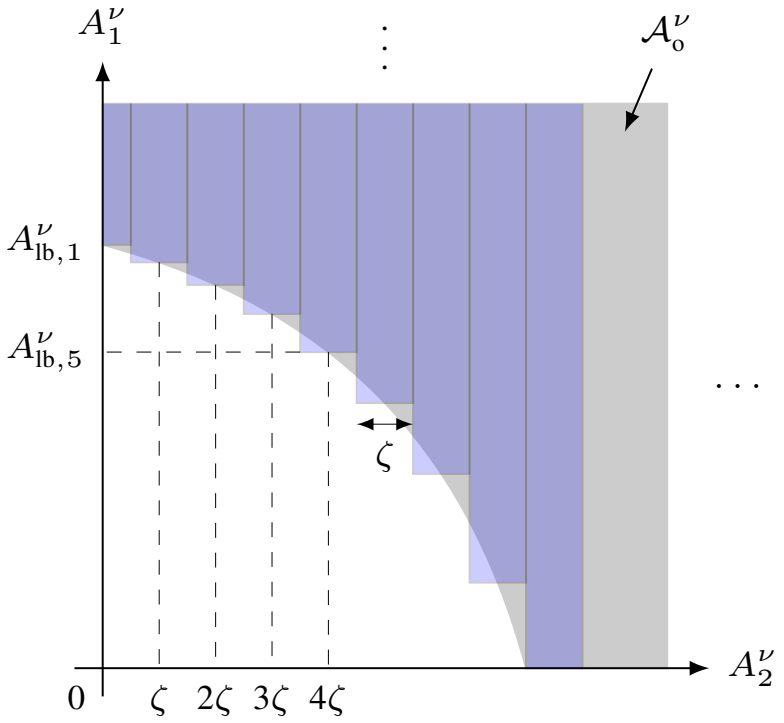

Figure 4-3: Stepwise approximation of the outage probability for the joint ground/on-board processing approach

is illustrated in Fig. 4-3, is inspired by the stepwise approximation of a desired joint probability distribution described in the recommendation ITU-R P.1815-1 [132]. A satisfying accuracy is obtained with a sufficiently small step size ζ. In this work, a step size of 0.01 dB is used.

Diversity Mode

Finally, the outage probability of the diversity mode is obviously the probability that the rain attenuations at both gateway locations are too high to guarantee an effective CINR higher than the outage CINR ρ_{o}. As a consequence, $\mathrm{P}\left\{\rho_{\mathrm{u}}^{\nu} \leq \rho_{\mathrm{o}}\right\}$ is in this case given by:

$$\mathrm{P}\left\{\rho_{\mathrm{u}}^{\nu} \leq \rho_{\mathrm{o}}\right\} = \mathrm{P}\left\{A_1^{\nu} \geq A_{\mathrm{lb}}^{\nu}, A_2^{\nu} \geq A_{\mathrm{lb}}^{\nu}\right\} \ , \tag{4.17}$$

with $A_{\mathrm{lb}}^{\nu} = \min\left\{ A \mid 10^{-\frac{A}{10}} \cdot \tilde{\rho}_{\mathrm{u}}^{\nu} \leq \rho_{\mathrm{o}} \right\}$.

4.3.2 Numerical Results

The outage probability of a Q/V-band MIMO link whose ground equipment is in Luxembourg and points to a satellite at 9° E are determined for all the possible operating modes. Rain attenuation statistics for circularly polarized waves at a carrier frequency of 50 GHz are considered. This latter frequency belongs to the upper frequencies of the Q/V-band where rain attenuation can be the most severe. The link budget is the same as the one used in Chapter 3 to analyze the effective uplink CINR as a function of the antenna arrangement in MIMO feeder links. It was provided in Table 3.1. If the antennas are optimally separated, the clear-sky uplink CINR reaches a maximum of 26 dB with spatial multiplexing. The same clear-sky CINR is reached with the diversity mode. Even though one of the antenna is deactivated, maximum ratio combining in the satellite brings a 3 dB diversity gain. On the other hand, the link budget from Table 3.1 leads to a clear-sky CINR of 23.5 dB for a state-of-the-art SISO link.

The results of the link-level outage analysis are shown in Fig. 4-4. Different antenna separations d_{E} have been used to observe their impact on the outage probability. The joint ground/on-board MIMO processing strategy guarantees a superior availability than a SISO approach. Even with an antenna separation of 30 km, a CINR improvement of 1 dB is observed at a target availability of 99 %. Two factors contribute to the availability gain with joint ground/on-board processing:

1. The use of two gateway antennas per link leads to an increase of the receive

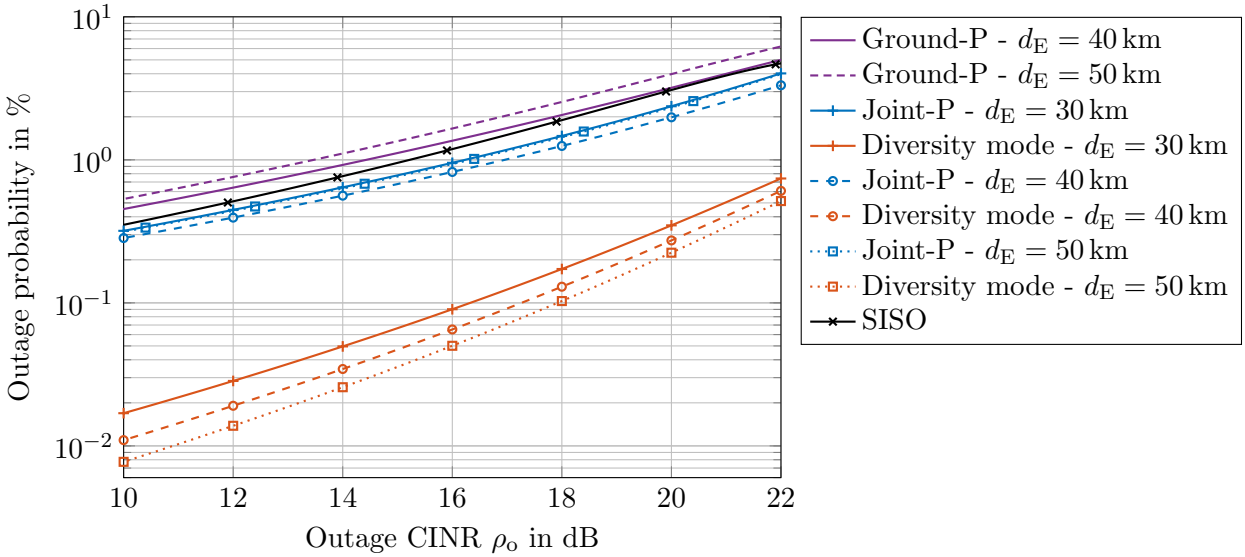

Figure 4-4: Link outage probability as a function of the outage CINR for a gateway array in Luxembourg with $\delta_E = 0°$ and a satellite at 9° E

carrier power.

2. In case of a heavy rainfall at one of the gateway antennas, the effective CINR loss is lower than the rain attenuation experienced by this antenna. This property was shown in (3.18).

On the contrary, the ground-limited processing approach does not provide an availability gain compared to a SISO link. This degraded performance is a consequence of the ineffective use of the available transmit power in case of a rain event. As already shown in (3.11), the effective CINR loss with ground-limited processing is always equal to the maximum of the rain attenuations. To limit the power consumption in the satellite payload, ground-limited processing should be used when the gateway antennas experience clear-sky or a moderate amount of rain attenuation. In the scenario under study, the ground-limited processing guarantees for example a CINR higher than 20 dB as long as the rain attenuations do not exceed 5.9 dB when $d_E = 40$ km or 5 dB when $d_E = 50$ km. If the weather conditions become too adverse, the spatial multiplexing mode then switches to the joint ground/on-board processing scheme as long as the guaranteed CINR is not below the outage CINR. Concerning the diversity mode, the results from Fig. 4-4 confirm the superior robustness of the

approach at the expense of a division of the supported downlink channels by two. As expected, the outage probability is lower for increased antenna separations due to the improved decorrelation of the rain events.

4.4 Robust Link Design

Based on the fact that the proposed architecture can be used for spatial multiplexing or diversity purposes, a MIMO feeder link is seen as a set of two virtual transmitters supporting $K/2$ data sequences each. The principle and the outage probability of these transmitters can be defined as follows:

Virtual transmitter 1: It guarantees the transmission of $K/2$ data streams if the spatial multiplexing mode is not in outage. As soon as spatial multiplexing is not feasible anymore, this transmitter is in outage. As mentioned in Section 4.3.2, a solution to maximize the link availability while limiting power consumption in the satellite is to resort to the joint ground/on-board processing approach only if ground-limited processing is not able to guarantee a sufficient CINR anymore. For the ν-th MIMO feeder link, the outage probability $p_{\mathrm{o},1}^{\nu}$ of its virtual transmitter 1 corresponds in this case to the outage probability of the joint ground/on-board processing which was defined in (4.16).

Virtual transmitter 2: The $K/2$ streams allocated to this transmitter are supported by the spatial multiplexing mode if no outage is encountered. In this case, virtual transmitters 1 and 2 share the K parallel channels available in the uplink. As soon as spatial multiplexing is not operational anymore, the streams are transferred to the diversity mode. Hence, in the ν-th MIMO feeder link, the outage probability $p_{\mathrm{o},2}^{\nu}$ of the virtual transmitter 2 is the probability defined in (4.17) that the diversity mode is in outage.

A graphical description of the resource allocation to virtual transmitters 1 and 2 is provided in Fig. 4-5.

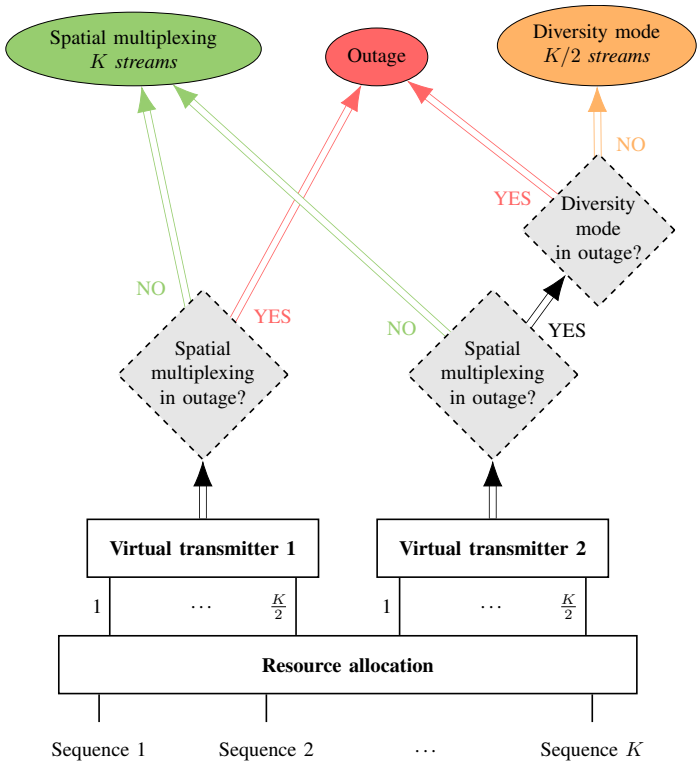

Figure 4-5: Resource allocation in a MIMO feeder link

4.5 System-Level Outage Analysis

The sufficient availability of a V/HTS system relying on feeder links in higher frequency bands can only be ensured if a smart diversity strategy is used at a system level. As a matter of fact, the extension of the well-known concepts of $N + P$ and $N + 0$ diversity developed for state-of-the-art SISO feeder links [15] are extended in this section to a MIMO-based architecture. First, a closed-form expression for the probability that a certain number of virtual transmitters in the system are in outage is determined. This result is then exploited to conduct an outage analysis of the proposed smart diversity strategies for MIMO feeder links.

4.5.1 Theoretical Background

Let's Q_ν be a discrete random variable with sample space $\{0, 1, 2\}$ that models the number of virtual transmitters in outage in the ν-th element of a set of N MIMO

feeder links. The separation between the feeder links is large enough[4] (hundreds of kilometers) to assume that their rain events and, hence, the random variables $Q_1, \ldots, Q_N$ are statistically independent. The total number of virtual transmitters in outage in the system is defined as $Q = \sum_{\nu=1}^{N} Q_\nu$. Here, the objective of the system outage analysis is first to determine $\mathrm{P}\{Q = q; N\}$ i.e., the probability that q virtual transmitters within N MIMO links are in outage. The distribution of Q is the convolution $*$ of the distributions of the independent random variables Q_ν such that:

$$\begin{aligned}\left[\mathrm{P}\{Q=0;N\}\ \mathrm{P}\{Q=1;N\}\ \ldots\ \mathrm{P}\{Q=2N;N\}\right] &= \left[\mathrm{P}\{Q_1=0\}\ \ldots\ \mathrm{P}\{Q_1=2\}\right] \\ &* \left[\mathrm{P}\{Q_2=0\}\ \ldots\ \mathrm{P}\{Q_2=2\}\right] * \ldots * \left[\mathrm{P}\{Q_N=0\}\ \ldots\ \mathrm{P}\{Q_N=2\}\right],\end{aligned} \tag{4.18}$$

with $\left[\mathrm{P}\{Q=0;N\}\ \ldots\ \mathrm{P}\{Q=2N;N\}\right]$ and $\left[\mathrm{P}\{Q_\nu=0\}\ \ldots\ \mathrm{P}\{Q_\nu=2\}\right]$ the distribution vectors of Q and Q_ν, respectively. Since the diversity mode cannot be in outage if the spatial multiplexing mode is not, it is easily established that $Q_\nu = 0$ if the virtual transmitter 1 of feeder link ν is not in outage. On the other hand, $Q_\nu = 2$ if its virtual transmitter 2 is in outage. Hence, the following relations are fulfilled:

$$\mathrm{P}\{Q_\nu=0\} = 1 - p_{\mathrm{o},1}^{\nu}, \quad \mathrm{P}\{Q_\nu=1\} = p_{\mathrm{o},1}^{\nu} - p_{\mathrm{o},2}^{\nu}, \quad \mathrm{P}\{Q_\nu=2\} = p_{\mathrm{o},2}^{\nu}\,. \tag{4.19}$$

The probability of $Q_\nu = 1$ was obtained using the property that $\sum_{q=0}^{2} \mathrm{P}\{Q_\nu = q\} = 1$. Relying on (4.18) and (4.19), the method from [133] is extended to obtain a closed-form expression for the probability density function (PDF) of the Poisson-multinomial distribution followed by the random variable Q. It is given by:

$$\mathrm{P}\{Q=q;N\} = \frac{\sum_{p=0}^{2N} e^{-j\frac{2\pi pq}{2N+1}} \prod_{\nu=1}^{N} \left\{\left(1-p_{\mathrm{o},1}^{\nu}\right) + p_{\mathrm{o},2}^{\nu}\cdot e^{-j\frac{4\pi p}{2N+1}} + \left(p_{\mathrm{o},1}^{\nu} - p_{\mathrm{o},2}^{\nu}\right)\cdot e^{-j\frac{2\pi p}{2N+1}}\right\}}{2N+1}\,. \tag{4.20}$$

[4] What is meant here is the separation between the sites of different links and not between the antennas within a single link.

This result is demonstrated in Appendix C. The knowledge of $\mathrm{P}\{Q = q; N\}$ can now be used to analyze the performance of the extension of the $N + 0$ and $N + P$ smart diversity strategies to the MIMO-based architecture.

4.5.2 $N + 0$ Diversity

Instead of supporting the data traffic for a given downlink channel with a single virtual transmitter, the uplink channel resources of several links are shared in time. The principle of the approach is similar to the satellite switched time division multiple access (SS-TDMA) scheme [134]. A symbol sequence intended for a downlink channel is decomposed into time slices which are allocated to slots within the time division multiple access (TDMA) frames of several virtual transmitters. It is assumed that the rain attenuations remain constant during the duration of a TDMA frame. Here, time slices of equal duration are considered. However, more advanced resource allocation strategies can be used to maximize the system throughput according to the traffic demands in the downlink channels [15]. For each MIMO feeder link whose part of the traffic is allocated to, one time slice is assigned to its virtual transmitter 1 and another to its virtual transmitter 2. If a cluster of N MIMO links is considered, time slices are thus spread between a total of $2N$ virtual transmitters. Since no redundant resources are available, part of the traffic is lost if an outage occurs for a virtual transmitter. The principle of this $N + 0$ smart diversity is illustrated in Fig. 4-6 for a cluster of $N = 2$ MIMO feeder links. The symbol sequences for $2N = 4$ downlink channels are equally spread between 4 virtual transmitters. In the considered example, the virtual transmitter 1 of one of the links is in outage because a gateway antenna experiences a heavy rain fade. Hence, the spatial multiplexing mode cannot be used anymore in this latter link. One fourth of the data traffic supported by the cluster is in this case lost. The second virtual transmitter of the degraded link would be in outage if its other antenna also suffers from a heavy rain fade.

To characterize the performance of the $N + 0$ smart diversity approach with a cluster of N MIMO feeder links, the cumulative distributive function (CDF) of the normalized throughput $\bar{T} = 1 - Q/(2N)$ is determined. $\bar{T}$ is equal to 1 if none of

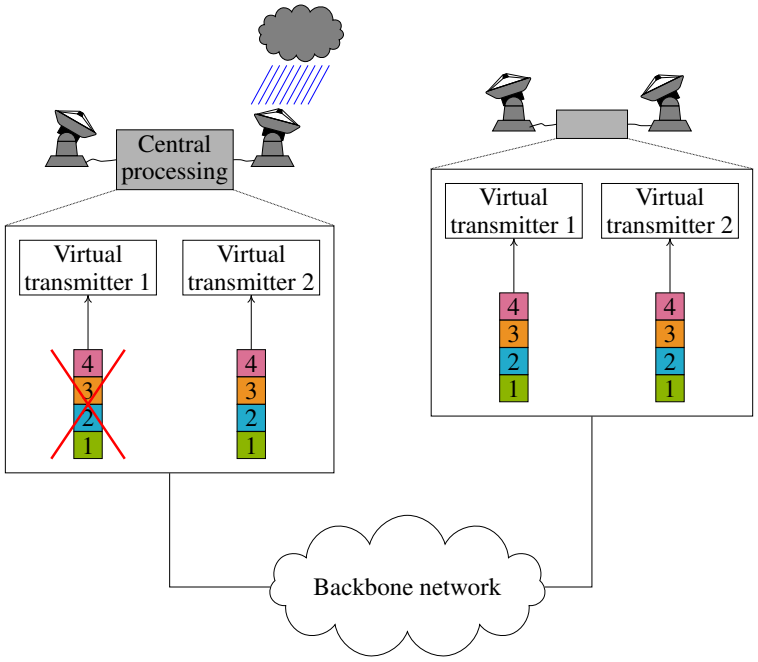

Figure 4-6: Principle of $N + 0$ smart diversity

the transmitters is in outage, and it is equal to 0 if all transmitters are in outage. Its CDF computes as:

$$\mathrm{P}\left\{\bar{T} \leq 1 - \frac{q}{2N}\right\} = \mathrm{P}\left\{Q \geq q; N\right\} = \sum_{q'=q}^{2N} \mathrm{P}\left\{Q = q'; N\right\} . \tag{4.21}$$

4.5.3 $N + P$ Diversity

With the $N + P$ smart diversity strategy, N active MIMO feeder links and $P < N$ redundant links are deployed. Contrary to the $N + 0$ approach, a data sequence is now supported by a single virtual transmitter in the system. If an outage occurs, the virtual transmitter of a redundant MIMO link is switched on to take over the data traffic. A system outage is encountered only if at least $2P+1$ virtual transmitters are in outage. In Fig. 4-7, the $N+P$ smart diversity strategy is illustrated for a scenario with $N = 2$ and $P = 1$. Due to heavy rainfalls, the first virtual transmitters of two of the links are in outage. As a consequence, their data streams have been reallocated to the two virtual transmitters of the redundant link in the system. Here, a data stream would be lost if a further gateway antenna in the system experiences a heavy

rain fade.

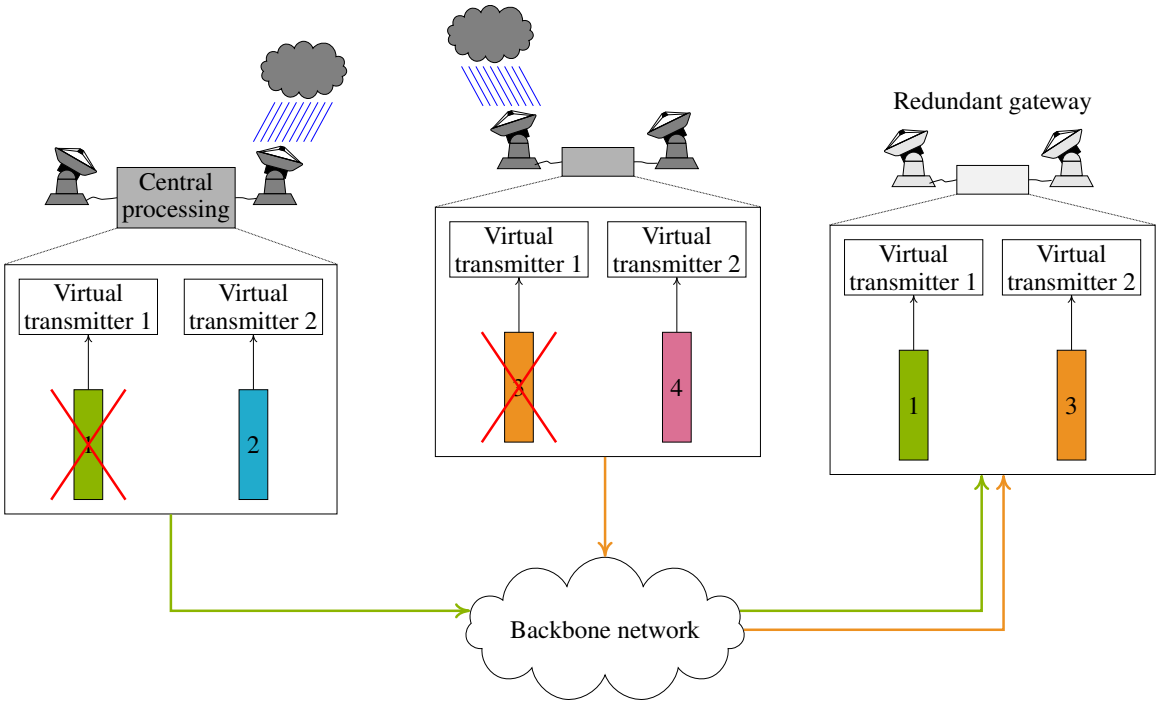

Figure 4-7: Principle of $N + P$ smart diversity

An availability analysis of the $N+P$ scheme is done by considering the probability that a given data stream experiences an outage. It is given by:

$$P_{\mathrm{o}}^{N+P} = \sum_{q=1}^{2N} \frac{q}{2N} \cdot \mathrm{P}\left\{Q = q + 2P; N + P\right\} \ . \tag{4.22}$$

Each term of the sum from (4.22) corresponds to the joint probability that $q + 2P$ transmitters are in outage and that a specific data stream is assigned to one of these transmitters.

4.5.4 Numerical Results

Similarly to the results presented in Section 4.3.2 for the link-level outage analysis, a Q/V-band system is considered. A satellite positioned at 9° E and rain attenuation statistics for circularly polarized waves at a carrier frequency of 50 GHz are used. The system-level outage analysis is here performed under the assumption that all

links in a given system have identical outage probabilities. For the MIMO links, this means that $p_{\mathrm{o},1}^{\nu} = p_{\mathrm{o},1}$ and $p_{\mathrm{o},2}^{\nu} = p_{\mathrm{o},2}$, $1 \leq \nu \leq N$. These outage probabilities are computed for different antenna separations of an array positioned in Luxembourg with $\delta_{\mathrm{E}} = 0°$. We note that, as shown in Fig. 3-6 in Chapter 3, the influence of the antenna separation on the effective uplink CINR is quasi-identical wherever the antenna array is positioned in Europe. Moreover, rain attenuation statistics in Luxembourg are a good approximation of long-term European weather conditions [16]. Thus, outage probabilities determined for an antenna array in Luxembourg are representative of MIMO links deployed in Europe. The system availabilities for the benchmark SISO-based system are determined as in [15]. To bring additional insights into the benefits of MIMO feeder links, the availability of the state-of-the-art system is not only evaluated with the rain attenuation statistics of Luxembourg. Since SISO feeder links require a higher number of gateway sites, some gateway antennas might have to be installed in regions where strong rain fades have a significantly higher probability. In such a case, the system performance is impacted. To take this aspect into account, the SISO-based architecture is also analyzed under the assumption that the rain attenuation statistics are those observed in the city of Turin (Italy). According to the annual exceedance probabilities from Fig. 4-1, strong rain fades indeed occur more frequently in Turin than in Luxembourg. Results determined with these less favorable weather conditions will be labeled *SISO - Unfavorable weather*. Lastly, the link budgets for the MIMO and the SISO feeder links are identical to those from Table 3.1. We recall that the clear-sky effective uplink CINR can reach in this case a maximum of 26 dB for a MIMO feeder link with optimally separated antennas. On the other hand, the clear-sky uplink CINR for a SISO link is only 23.5 dB.

In Fig. 4-8, the CDF of the normalized throughput with the $N + 0$ diversity and an outage CINR $\rho_{\mathrm{o}} = 20\,\mathrm{dB}$ is presented for clusters of 4 and 10 gateway antennas. It corresponds to $N_{\mathrm{MIMO}} = 2$ and $N_{\mathrm{MIMO}} = 5$ MIMO feeder links, respectively. The MIMO-based solution offers in almost all cases a higher or at least an equivalent normalized throughput than a SISO solution. For example, in a SISO-based system with $N_{\mathrm{SISO}} = 4$ and the rain statistics of Luxembourg, the throughput is lower or

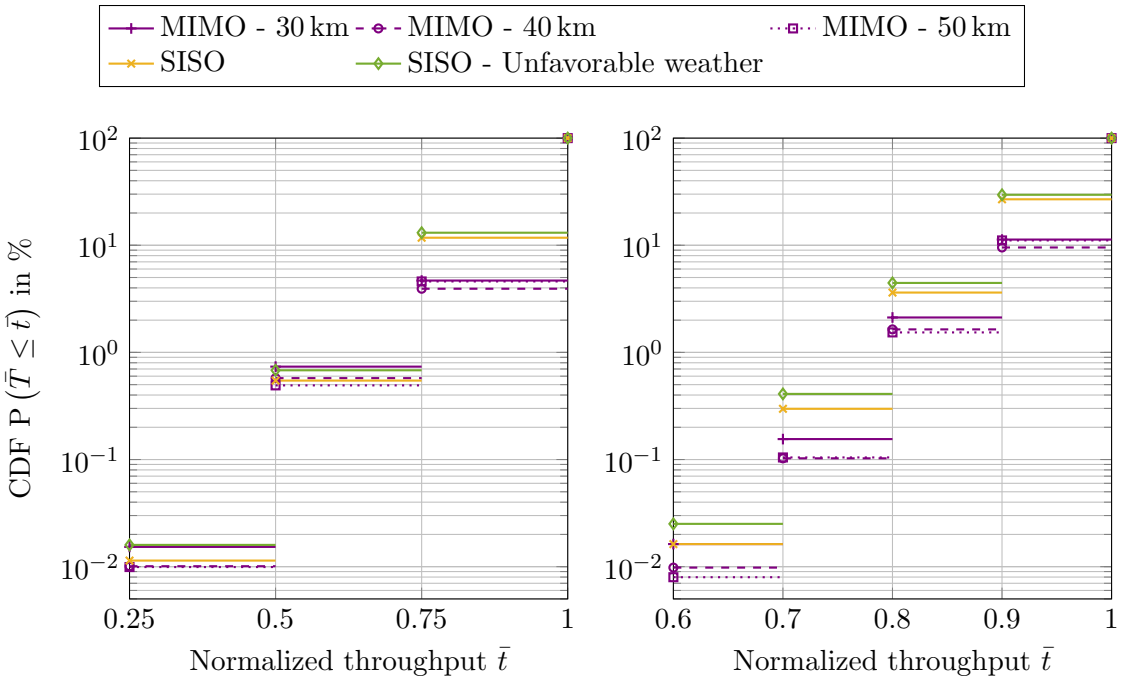

(a) $N_{\mathrm{MIMO}} = 2$ and $N_{\mathrm{SISO}} = 4$ (b) $N_{\mathrm{MIMO}} = 5$ and $N_{\mathrm{SISO}} = 10$

Figure 4-8: Cumulative distribution function of the normalized throughput with $N+0$ smart diversity for $\delta_{\mathrm{E}} = 0°$ and $\rho_{\mathrm{o}} = 20\,\mathrm{dB}$

equal to 75 % of its maximum during 11.8 % of an average year. On the other hand, this situation occurs only during 4.7 % of the time in a MIMO-based system with $N_{\mathrm{MIMO}} = 2$ and $d_{\mathrm{E}} = 30\,\mathrm{km}$. Slightly better availabilities are achieved with higher antenna separations of $d_{\mathrm{E}} = 40\,\mathrm{km}$ or $d_{\mathrm{E}} = 50\,\mathrm{km}$ due to a better decorrelation of the rain events at the gateway antennas.

In Fig. 4-9, the system outage probability for the $N+P$ smart diversity is shown for architectures composed of $N_{\mathrm{MIMO}} = 15$ MIMO feeder links and $N_{\mathrm{SISO}} = 30$ SISO links. Results with 2 and 4 redundant transmit antennas are displayed. This corresponds to $P_{\mathrm{MIMO}} = 1$, $P_{\mathrm{SISO}} = 2$ and $P_{\mathrm{MIMO}} = 2$, $P_{\mathrm{SISO}} = 4$, respectively. For a target system availability of 99.99 %, the MIMO-based system with 2 redundant links and $d_{\mathrm{E}} = 40\,\mathrm{km}$ guarantees an effective uplink CINR of at least 22 dB. On the other hand, the considered benchmark SISO systems only ensure minimum CINR values of 19.7 dB and 19.1 dB. This corresponds to CINR differences of 2.3 dB and 2.9 dB, respectively. With $P_{\mathrm{MIMO}} = 1$ and $P_{\mathrm{SISO}} = 2$, MIMO links bring a CINR gain of 4.3 dB compared to SISO links with unfavorable weather at the same target availability of 99.99 %.

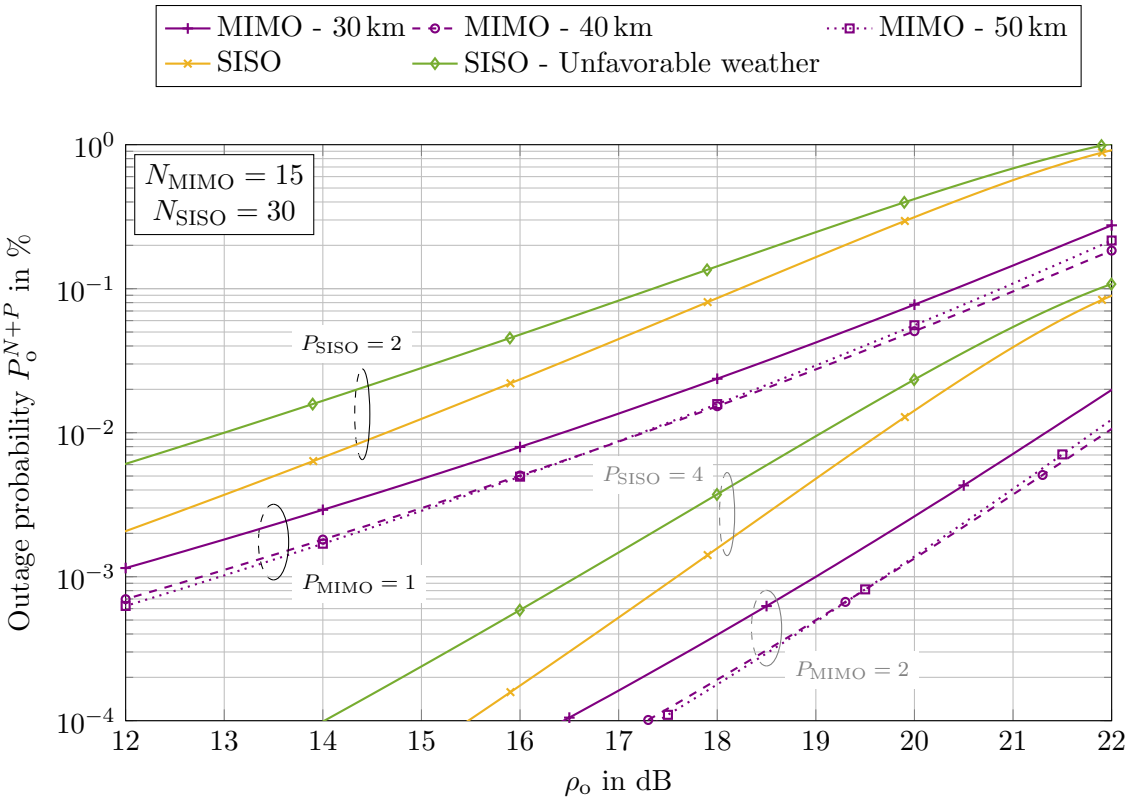

Figure 4-9: System outage probability as a function of the outage CINR with $N + P$ smart diversity for $\delta_{\text{E}} = 0°$

To strengthen the previous results, link and system level availabilities in an average year are provided in Table 4.1 for different values of the outage CINR ρ_{o}. The

Table 4.1: Link and system level annual availabilities in % for different outage CINRs (Rain attenuation statistics of Luxembourg - MIMO with $d_{\text{E}} = 40\,\text{km}$ and $\delta_{\text{E}} = 0°$)

	Link-level analysis			***System-level analysis with*** $N + P$ ***approach***			
	SISO	MIMO		SISO - $N_{\text{SISO}} = 30$		MIMO - $N_{\text{MIMO}} = 15$	
		Spatial multiplexing	Diversity mode	$P_{\text{SISO}} = 2$	$\mathbf{P_{SISO} = 4}$	$P_{\text{MIMO}} = 1$	$\mathbf{P_{MIMO} = 2}$
ρ_{o} = 20 dB	96.920 %	98.016 %	99.727 %	**99.686 %**	**99.986 %**	**99.949 %**	**99.999 %**
ρ_{o} = 18 dB	98.104 %	98.749 %	99.870 %	**99.914 %**	**99.998 %**	**99.985 %**	**> 99.999 %**
ρ_{o} = 16 dB	98.810 %	99.177 %	99.935 %	**99.977 %**	**> 99.999 %**	**99.995 %**	**> 99.999 %**

parameters $d_{\text{E}} = 40\,\text{km}$ and $\delta_{\text{E}} = 0°$ are assumed for the MIMO links. Moreover, only the values obtained with the rain attenuation statistics of Luxembourg i.e., with the same weather conditions than for the MIMO-based system, are shown for the SISO configuration. Even though the MIMO feeder links are here not advantaged in terms of rain attenuation statistics, it clearly appears, as already observed in Fig. 4-4 and

Fig. 4-9, that a significant improvement of the link and system level availabilities is obtained with the proposed concept.

4.6 Summary and Future Works

Strategies to ensure a high system availability with MIMO feeder links have been presented. First, a diversity mode that supports only half of the data traffic when a heavy rain attenuation occurs at one of the gateway antennas of a link has been introduced. A link-level outage analysis has then been conducted for both the spatial multiplexing and the diversity modes to assess their robustness. The advantage of a joint ground/on-board processing strategy to maximize the availability of the spatial multiplexing mode has especially been emphasized. Relying on the results of the link-level outage analysis, advanced smart diversity strategies that extend the $N+0$ and $N+P$ diversity concepts to MIMO-based feeder link architectures have been designed. These strategies share the resources of different MIMO feeder links to maximize the system availability. Numerical results have demonstrated the significant availability gains that can be obtained with MIMO feeder links compared to the state-of-the art.

Future research works on smart diversity for MIMO feeder links should concentrate on the design of switching algorithms for the $N+P$ approach. The system-level outage analysis of the $N+P$ smart diversity scheme has been done under the hypothesis of a perfect traffic switching from a link in outage to a redundant link. However, in a practical system, gateway handover mechanisms supervised from a network control center are required to manage the data traffic. An accurate prediction of link outages is here of paramount importance to reroute the traffic before an outage occurs and, hence, avoid the loss of data. Some studies have already investigated this challenging network management problem for state-of-the-art SISO links [13], [135]. However, these solutions cannot be directly applied to MIMO-based feeder links. In particular, strategies able to predict the outage of a given MIMO link based on the knowledge of the rain fade slopes experienced by its ground antennas must be developed.

Chapter 5

Conclusion

5.1 Summary

Communication networks of fifth generation (5G) and beyond will retain a significant role to satellite systems. Major technological advancements have indeed made satellites able to support services that could not be procured in a cost-effective manner by terrestrial alternatives. This includes among others the delivery of broadband services in planes, ships and regions without fiber optic broadband access as well as the distribution of data contents to the network edges. Such services can be provided by geostationary V/HTS systems that use hundreds of narrow spot beams to reuse the frequency resources in the user links and, thus, maximize the sum throughput. With the Ka-band (20/30 GHz), an aggregate user link bandwidth of several hundreds of GHz is reached. The design of the feeder links, that provide the data from the gateway earth stations to the satellite, becomes in that case an extremely challenging engineering problem since a tremendous amount of bandwidth must be supported. In current systems, it is necessary to have a large number of spatially separated feeder beams that fully reuse the uplink frequency resources in the Q/V-band (40/50 GHz). With state-of-the-art solutions, this requires to conceive a ground segment with tens of stations separated by several hundreds of kilometers. Hence, the search for gateway deployment sites and the design of the backbone network are significantly complicated. In addition to geographical and political constraints, re-

strictions in the selection of the gateway locations apply due to radio regulations. The Q/V-band is not an exclusive band and necessitates coordination with other services such as fixed service. Weather impairments, especially rain attenuation, represent also an important issue due to their impact on the system availability. Thus far, the use of higher frequency bands (W-band or optical bands) with a larger available bandwidth has been proposed in the literature as a solution to reduce the number of gateway sites. However, this comes at the cost of a degraded performance during unfavorable weather. An innovative solution based on the MIMO LOS technology has been proposed in this doctoral thesis to facilitate the search for gateway sites while improving at the same time the system robustness against rain fades. The considered approach, which increases the supported data traffic without changing the frequency band used, is called *MIMO feeder links*. The research works have focused on the system requirements and the signal processing needed for a reliable operation of such links.

Chapter 1 gave an overview of the development of satellite communications over the last decades and underlined the importance of upcoming V/HTS systems. A thorough literature review on the MIMO LOS concept, which is a major building block of the proposed feeder link solution, has also been carried out. Moreover, the basic design rules for the optimization of the antenna positions in a MIMO LOS satellite system have been recalled. Chapter 1 is concluded by an enumeration of the original contributions of this work and the associated publications.

The architecture of MIMO feeder links have been thoroughly described at the beginning of Chapter 2. Contrary to current solutions, two time- and phase-synchronized antennas separated by a few tens of kilometers are activated in each link. Using two satellite antennas within a few meters distance and with identical beam coverages, spatial multiplexing can then be exploited to double the throughput per feeder link. Instead of deploying U antennas hundreds of kilometers away from each other to reach a given target sum throughput, the ground segment now consists of $U/2$ 2-element antenna arrays. Even though the total number of ground antennas is not decreased with this novel architecture, the required number of gateway sites is, on the other

hand, halved.

The second part of Chapter 2 has been focused on the channel modeling of the obtained MIMO feeder links. The considered effects included the depointing loss of the receive antennas, the tropospheric impairments and the impact of the satellite movement in its station-keeping box. It has been emphasized how this latter phenomena must be accurately predicted and corrected to avoid the use of an outdated MIMO channel information. The importance of a time-alignment to compensate for the different propagation delays has also been discussed.

In Chapter 3, an equivalent baseband model of the transmission chain for MIMO feeder links has been introduced. This model includes especially pre- and post-processing matrices that represent a linear combination of the transmit and receive signals in the central processing unit of the gateway and the satellite on-board processor, respectively. These matrices have been optimized to completely cancel the spatial interference between the data streams. Since CSI is required for this purpose, a candidate architecture for the CSI acquisition has been first discussed. Two different spatial interference cancellation strategies based on the ZF criterion have been introduced for the computation of the processing matrices: a ground-limited and a joint ground/on-board processing approach. Whereas interference cancellation is entirely supported by the pre-processing matrix with the first scheme, the second one relies on a distributed processing between the gateway and the satellite. The superiority of joint ground/on-board processing in the case where the weather conditions at the gateway antennas differ significantly has been highlighted. The results have also illustrated that a separation mismatch of more than $\pm 10\,\mathrm{km}$ between the ground antennas can be accepted for both approaches without entailing a strong CINR loss.

Finally, to improve the link availability in the case of strong rain fades, an innovative smart gateway solution based on the specific architecture of MIMO feeder links has been developed in Chapter 4. The proposed scheme enables to exploit a MIMO feeder link either in a spatial multiplexing mode with one of the interference cancellation strategy introduced in Chapter 3 or in a diversity mode supporting only half of the data traffic when the weather conditions become too adverse. This unique

feature of MIMO feeder links has been exploited to improve the $N + 0$ and $N + P$ smart diversity strategies and guarantees a significantly higher system availability than state-of-the-art solutions.

To summarize, the theoretical framework of a completely novel MIMO-based architecture for the feeder links of next-generation V/HTS systems has been developed in this doctoral work. The channel modeling, the MIMO signal processing and the required diversity strategies have been addressed. Moreover, the fundamental design trade-offs and the expected performance gains have been thoroughly discussed.

5.2 Future perspectives

Whereas this work has enabled to formulate the technology concept for MIMO feeder links, which corresponds to a technology readiness level (TRL) 2 according to NASA and ESA, specific aspects related to practical deployment considerations should be addressed. The following topics must in particular be considered to reach higher TRLs and favor the transfer of the technology in next-generation systems:

Low-cost time- and phase synchronization: The advent of widely-spaced antenna arrays with strict synchronization requirements for applications ranging from radio science to power efficient deep space communication has led to the development of novel time- and frequency distribution schemes with reduced costs. The ability of such approaches to fulfill the synchronization requirements of MIMO feeder links in terms of maximum tolerable phase drift and time-delay compensation errors must be carefully assessed. If necessary, modifications to cope with the particularities of the considered application must be undertaken to further reduce the technology costs and/or improve its accuracy.

On-board processing capabilities: As emphasized in this thesis, the use of an advanced on-board processor is necessary to get full benefit of MIMO feeder links. Future research and development studies must hence focus on the detailed specification of such a processor.

CSI acquisition schemes: Since an accurate CSI is necessary to enable the spatial interference cancellation, the design of the CSI acquisition will play a key role in the system reliability. Further research efforts will help finding the best compromise between the costs of the equipment required to conduct the channel estimation (radiometers, beacon receivers, etc.) and the achieved precision. Another important issue are the design requirements for a high-speed configuration link to regularly update the on-board processor according to the CSI changes.

Transport-layer issues: Whereas this work has mainly concentrated on the physical layer aspects, the transport layer must also be optimized to enable an efficient use of the network resources. In this context, the management of the traffic flows in the ground network must be appropriately designed to avoid congestion and packet losses. This is especially important when packets have to be re-routed due to a gateway outage. These transport-layer issues, which have been addressed in the literature for state-of-the-art smart gateway solutions, must be adapted to MIMO-based feeder link architectures.

Appendix A

Per-Antenna Transmit Power with Ground-Limited Processing

The entries of $\mathbf{H}_l^{\nu\nu}$ and those of the ZF precoder $\mathbf{B}_l^{\nu}$ fulfill the following condition:

$$h_{m1}^{\nu\nu} b_{1h}^{\nu} = -h_{m2}^{\nu\nu} b_{2h}^{\nu},\ m, h \in \{1, 2\}\,,\ m \neq h\ . \tag{A.1}$$

This relation ensures that the anti-diagonal elements of $\mathbf{H}_l^{\nu\nu}\mathbf{B}_l^{\nu}$ are equal to 0. Resorting to the model from (2.30), it implies that:

$$|b_{1h}^{\nu}| = \frac{\alpha_2^{\nu}}{\alpha_1^{\nu}} \cdot |b_{2h}^{\nu}|\ . \tag{A.2}$$

Here, the fact that the path losses for each transmit-receive antenna pair in a given MIMO feeder link are quasi-identical has been used. A relation between the diagonal elements of the matrix $\mathbf{B}_l^{\nu}\left(\mathbf{B}_l^{\nu}\right)^{\mathrm{H}}$ can then be formulated as:

$$\left[\mathbf{B}_l^{\nu}\left(\mathbf{B}_l^{\nu}\right)^{\mathrm{H}}\right]_{1,1} = \left(\frac{\alpha_2^{\nu}}{\alpha_1^{\nu}}\right)^2 \cdot \left[\mathbf{B}_l^{\nu}\left(\mathbf{B}_l^{\nu}\right)^{\mathrm{H}}\right]_{2,2}\ . \tag{A.3}$$

Since $\mathbf{B}_l^{\nu}$ is normalized to guarantee that at least one of the gateway antennas uses the maximum transmit power $P_{\mathrm{u},l}^{\nu}$, (3.10) is finally obtained.

Appendix B

Joint Ground/On-Board Processing

B.1 Optimization

Under the ZF constraint, the mean squared error (MSE) for the k-th data stream is given by:

$$\mathrm{MSE}_k^\nu = \mathbb{E}\left[|z_k^\nu - s_k^\nu|^2\right] = (\mathbf{w}_k^\nu)^{\mathrm{H}} \left(\mathbf{R}_{\boldsymbol{\eta}_{\mathrm{I}}^\nu} + \mathbf{R}_{\boldsymbol{\eta}_{\mathrm{T}}^\nu}\right) \mathbf{w}_k^\nu = \frac{1}{\rho_{\mathrm{u},k}^\nu} \,. \tag{B.1}$$

The optimization problem from (3.13) is thus equivalent to the following one:

$$\begin{aligned} \min_{\mathbf{B}^\nu, \mathbf{W}^\nu} \quad & \max_k \ \mathrm{MSE}_k^\nu \\ \text{s.t.} \quad & \mathbf{B}^\nu (\mathbf{B}^\nu)^{\mathrm{H}} \leq \mathrm{diag}\left\{P_{\mathrm{u},1}^\nu \mathbf{I}_2, \ldots, P_{\mathrm{u},L}^\nu \mathbf{I}_2\right\} = \mathbf{P}^\nu \\ & (\mathbf{W}^\nu)^{\mathrm{H}} \bar{\mathbf{H}}^{\nu\nu} \mathbf{B}^\nu = \mathbf{I}_L \,. \end{aligned} \tag{B.2}$$

As seen in (B.1), the k-th column of $\mathbf{W}^\nu$ only influences the MSE of the k-th stream. Therefore, assuming in a first step that the precoder $\mathbf{B}^\nu$ is fixed, each $\mathbf{w}_k^\nu$ can be

optimized separately as the solution of:

$$\begin{aligned} \min_{\mathbf{w}_k^\nu} \quad & \mathrm{MSE}_k^\nu \\ \text{s.t.} \quad & \left(\mathbf{w}_k^\nu\right)^{\mathrm{H}} \bar{\mathbf{H}}^{\nu\nu} \mathbf{B}^\nu = \mathbf{e}_k^{\mathrm{H}} \ , \end{aligned} \tag{B.3}$$

where $\mathbf{e}_k$ is a column vector with only zeros except for its k-th entry which is equal to one. To this end, the Lagrangian function $L\left(\mathbf{w}_k^\nu\right)$ is defined as:

$$L\left(\mathbf{w}_k^\nu\right) = \left(\mathbf{w}_k^\nu\right)^{\mathrm{H}} \left(\mathbf{R}_{\boldsymbol{\eta}_{\mathrm{I}}^\nu} + \mathbf{R}_{\boldsymbol{\eta}_{\mathrm{T}}^\nu}\right) \mathbf{w}_k^\nu - \left\{ \left(\mathbf{w}_k^\nu\right)^{\mathrm{H}} \bar{\mathbf{H}}^{\nu\nu} \mathbf{B}^\nu - \mathbf{e}_k^{\mathrm{H}} \right\} \boldsymbol{\lambda} \ . \tag{B.4}$$

The vector $\boldsymbol{\lambda}$ is the vector of Lagrangian multipliers. Taking the derivative of (B.4) with respect to $\left(\mathbf{w}_k^\nu\right)^{\mathrm{H}}$ and setting it to zero, the following expression is obtained:

$$\mathbf{w}_k^\nu = \left(\mathbf{R}_{\boldsymbol{\eta}_{\mathrm{I}}^\nu} + \mathbf{R}_{\boldsymbol{\eta}_{\mathrm{T}}^\nu}\right)^+ \bar{\mathbf{H}}^{\nu\nu} \mathbf{B}^\nu \boldsymbol{\lambda} \ . \tag{B.5}$$

Introducing this result in the ZF constraint of (B.3), it comes out that the vector of Lagrangian multipliers is given by:

$$\boldsymbol{\lambda} = \left[\left(\mathbf{B}^\nu\right)^{\mathrm{H}} \left(\bar{\mathbf{H}}^{\nu\nu}\right)^{\mathrm{H}} \left(\mathbf{R}_{\boldsymbol{\eta}_{\mathrm{I}}^\nu} + \mathbf{R}_{\boldsymbol{\eta}_{\mathrm{T}}^\nu}\right)^+ \bar{\mathbf{H}}^{\nu\nu} \mathbf{B}^\nu \right]^+ \mathbf{e}_k \ . \tag{B.6}$$

Using (B.5) and (B.6), it finally becomes obvious that:

$$\left(\mathbf{w}_k^\nu\right)^{\mathrm{H}} = \mathbf{e}_k^{\mathrm{H}} \left(\bar{\mathbf{H}}^{\nu\nu} \mathbf{B}^\nu\right)^+ \ . \tag{B.7}$$

The optimal precoder $\mathbf{B}^\nu$ can now be determined. Based on the expression from (B.7), the MSE for the k-th data stream in (B.1) can be reformulated as a function of $\mathbf{B}^\nu$ such that the optimization problem in (B.2) is equivalent to:

$$\begin{aligned} \min_{\mathbf{B}^\nu} \quad & \max_k \ \mathbf{e}_k^{\mathrm{H}} \left[\left(\mathbf{B}^\nu\right)^{\mathrm{H}} \left(\bar{\mathbf{H}}^{\nu\nu}\right)^{\mathrm{H}} \left(\mathbf{R}_{\boldsymbol{\eta}_{\mathrm{I}}^\nu} + \mathbf{R}_{\boldsymbol{\eta}_{\mathrm{T}}^\nu}\right)^+ \bar{\mathbf{H}}^{\nu\nu} \mathbf{B}^\nu \right]^+ \mathbf{e}_k \\ \text{s.t.} \quad & \mathbf{B}^\nu \left(\mathbf{B}^\nu\right)^{\mathrm{H}} \leq \mathrm{diag}\left\{ P_{\mathrm{u},1}^\nu \mathbf{I}_2, \ldots, P_{\mathrm{u},L}^\nu \mathbf{I}_2 \right\} = \mathbf{P}^\nu \ . \end{aligned} \tag{B.8}$$

As shown in Appendix D of [129], the objective function $q_0(f_1, \ldots, f_K) = \max_k f_k$ is a Schur-convex function. In this case, a direct application of the result from [128] leads to:

$$\mathbf{B}^{\nu} = \mathbf{P}^{\nu,\frac{1}{2}} \mathbf{V}^{\nu} \mathbf{\Omega} \, . \tag{B.9}$$

B.2 Effective CINR

Relying on the model from (2.30) and (3.15), the two following relations can be established:

$$\mathrm{tr}\left\{ \left(\mathbf{H}_l^{\nu\nu}\right)^{\mathrm{H}} \mathbf{H}_l^{\nu\nu} \right\} = \gamma_{l,1}^{\nu} + \gamma_{l,2}^{\nu} = 2C_l \cdot \left\{ \left(\alpha_1^{\nu}\right)^2 + \left(\alpha_2^{\nu}\right)^2 \right\} \, , \tag{B.10}$$

$$\det\left\{ \left(\mathbf{H}_l^{\nu\nu}\right)^{\mathrm{H}} \mathbf{H}_l^{\nu\nu} \right\} = \gamma_{l,1}^{\nu} \gamma_{l,2}^{\nu} = 4C_l^2 \cdot \left(\alpha_1^{\nu} \alpha_2^{\nu}\right)^2 \left(1 - D_l\right) \, , \tag{B.11}$$

where C_l is a constant depending on the free-space loss and the antenna gains in the l-th frequency channel. On the other hand, $D_l \in [0, 1]$ depends on the phase relationships between the MIMO channel coefficients. The fact that, for a given carrier frequency, the free-space path losses are quasi-identical has been used to obtain (B.10) and (B.11). Including these expressions in (3.17), the effective uplink CINR can then be rewritten as:

$$\rho_{\mathrm{u},k}^{\nu} = 2 \cdot \frac{\left(\alpha_1^{\nu} \alpha_2^{\nu}\right)^2}{\left(\alpha_1^{\nu}\right)^2 + \left(\alpha_2^{\nu}\right)^2} \cdot K \cdot \left\{ \sum_{l=1}^{L} \frac{P_{\mathrm{T},l}^{\nu} + P_{\mathrm{I},l}^{\nu}}{P_{\mathrm{u},l}^{\nu}} \cdot \frac{1}{C_l \left(1 - D_l\right)} \right\}^{+} \, . \tag{B.12}$$

Defining $\tilde{\rho}_{\mathrm{u}}^{\nu}$ as the CINR in clear-sky conditions, i.e. when $\alpha_1^{\nu} = \alpha_2^{\nu} = 1$, the result from (3.18) becomes obvious.

Appendix C

Poisson-Multinomial Distribution

Following a reasoning similar to [133], a polynomial representation of (4.18) is considered. With the notations introduced in (4.19), it is given by:

$$\mathrm{P}\left\{Q=0;N\right\}+\mathrm{P}\left\{Q=1;N\right\}z+\ldots+\mathrm{P}\left\{Q=2N;N\right\}z^{2N}= \prod_{\nu=1}^{N}\left\{1-p_{\mathrm{o},1}^{\nu}+\left(p_{\mathrm{o},1}^{\nu}-p_{\mathrm{o},2}^{\nu}\right)z+p_{\mathrm{o},2}^{\nu}z^{2}\right\}. \quad \text{(C.1)}$$

This relation can be exploited to determine a closed-form expression of $\mathrm{P}\left\{Q=q;N\right\}$ as a function of $p_{\mathrm{o},1}^{\nu}, p_{\mathrm{o},2}^{\nu}$ with $1 \leq \nu \leq N$. To this end, a method of polynomial interpolation based on the inversion of a Vandermonde matrix is used. It requires the evaluation of the product on the right-hand side of (C.1) for $2N+1$ different values $z_0, \ldots, z_{2N}$ of z. This operation can be represented in a matrix form as:

$$\begin{bmatrix} 1 & z_0 & z_0^2 & \cdots & z_0^N \\ 1 & z_1 & z_1^2 & \cdots & z_1^N \\ & & \vdots & & \\ 1 & z_{2N} & z_{2N}^2 & \cdots & z_{2N}^{2N} \end{bmatrix} \begin{bmatrix} \mathrm{P}\left\{Q=0;N\right\} \\ \mathrm{P}\left\{Q=1;N\right\} \\ \vdots \\ \mathrm{P}\left\{Q=2N;N\right\} \end{bmatrix} = \begin{bmatrix} \prod_{\nu=1}^{N}\left\{1-p_{\mathrm{o},1}^{\nu}+\left(p_{\mathrm{o},1}^{\nu}-p_{\mathrm{o},2}^{\nu}\right)z_0+p_{\mathrm{o},2}^{\nu}z_0^2\right\} \\ \prod_{\nu=1}^{N}\left\{1-p_{\mathrm{o},1}^{\nu}+\left(p_{\mathrm{o},1}^{\nu}-p_{\mathrm{o},2}^{\nu}\right)z_1+p_{\mathrm{o},2}^{\nu}z_1^2\right\} \\ \vdots \\ \prod_{\nu=1}^{N}\left\{1-p_{\mathrm{o},1}^{\nu}+\left(p_{\mathrm{o},1}^{\nu}-p_{\mathrm{o},2}^{\nu}\right)z_{2N}+p_{\mathrm{o},2}^{\nu}z_{2N}^2\right\} \end{bmatrix}. \quad \text{(C.2)}$$

Obviously, expressions for $\mathrm{P}\{Q = q; N\}$, $1 \leq q \leq 2N$, can be obtained if the Vandermonde matrix on the left-hand side of (C.2) is invertible. This property is guaranteed when $z_p = e^{j\frac{2\pi p}{2N+1}}/\sqrt{2N+1}$, $0 \leq p \leq 2N$. In this case, the considered Vandermonde matrix is indeed a unitary DFT matrix. Multiplying both sides of (C.2) on the left by the inverse DFT matrix, the result from (4.20) is finally obtained.

Bibliography

[1] J. Logsdon, *Exploring the Unknown: Using space*, ser. Exploring the Unknown: Selected Documents in the History of the U.S. Civilian Space Program. NASA, 1998 (cit. on pp. 1, 3).

[2] A. Clarke, "Extra-terrestrial relays: Can rocket stations give world wide radio coverage?", *Wireless World*, pp. 305–308, Oct. 1945 (cit. on p. 1).

[3] J. Pelton, "The start of commercial satellite communications [History of communications]", *IEEE Commun. Mag.*, vol. 48, no. 3, pp. 24–31, Mar. 2010 (cit. on pp. 1–3).

[4] G. Senn and P. Siglin, "Courier satellite communication system", *IRE Trans. Mil. Electron.*, vol. MIL-4, no. 4, pp. 407–413, Oct. 1960 (cit. on p. 2).

[5] G. W. Beakley, "Overview of commercial satellite communications", *IEEE Trans. Aerosp. Electron. Syst.*, vol. 20, no. 4, pp. 455–464, Jul. 1984 (cit. on p. 3).

[6] G. Maral, M. Bousquet, and Z. Sun, *Satellite Communications Systems: Systems, Techniques and Technology*, ser. Wiley Series in Communication and Distributed Systems. Wiley, 2011 (cit. on pp. 3, 9, 24, 25, 27, 30, 36).

[7] S. I. Association. (Sep. 2018). State of the satellite industry report, [Online]. Available: http://www.sia.org/ (cit. on p. 3).

[8] P. Inigo, O. Vidal, B. Roy, E. Alberty, N. Metzger, D. Galinier, J. Anzalchi, G. Huggins, and S. Stirland, "Review of terabit/s satellite, the next generation of HTS systems", in *Proc. IEEE 7th Advanced Satellite Multimedia Systems Conference and 13th Signal Processing for Space Communications Workshop (ASMS/SPSC'08)*, Sep. 2014, pp. 318–322 (cit. on p. 4).

[9] B. Palacin, N. J. G. Fonseca, M. Romier, R. Contreres, J. C. Angevain, G. Toso, and C. Mangenot, "Multibeam antennas for very high throughput satellites in Europe: Technologies and trends", in *Proc. IEEE 11th European Conference on Antennas and Propagation (EUCAP'17)*, Mar. 2017, pp. 2413–2417 (cit. on pp. 4, 24, 38).

[10] P. Angeletti, R. D. Gaudenzi, and M. Lisi, "From bent pipes to software defined payloads: Evolution and trends of satellite communications systems", in *Proc. AIAA 26th International Communications Satellite Systems Conference (ICSSC'08)*, Jun. 2008, pp. 1–10 (cit. on pp. 5, 25, 26).

[11] G. Giambene, S. Kota, and P. Pillai, "Satellite-5G integration: A network perspective", *IEEE Network*, vol. 32, no. 5, pp. 25–31, Sep. 2018 (cit. on pp. 5, 6).

[12] J. Pérez-Trufero, B. Evans, A. Kyrgiazos, M. Dervin, B. Garnier, and C. Baudoin, "High throughput satellite system with Q/V-band gateways and its integration with terrestrial broadband communication networks", in *Proc. AIAA 32nd International Communications Satellite Systems Conference (ICSSC'14)*, Aug. 2014, pp. 1–10 (cit. on p. 6).

[13] J. Liu, Y. Shi, Z. M. Fadlullah, and N. Kato, "Space-air-ground integrated network: A survey", *IEEE Commun. Surveys Tuts.*, vol. 20, no. 4, pp. 2714–2741, May 2018 (cit. on pp. 6, 89).

[14] *Final Acts WRC-15*, World Radiocommunication Conference, Geneva, Switzerland, 2015 (cit. on p. 6).

[15] A. Kyrgiazos, B. G. Evans, and P. Thompson, "On the gateway diversity for high throughput broadband satellite systems", *IEEE Trans. Wireless Commun.*, vol. 13, no. 10, pp. 5411–5426, Oct. 2014 (cit. on pp. 7, 34, 81, 83, 86).

[16] A. Gharanjik, B. Shankar, P. D. Arapoglou, and B. Ottersten, "Multiple gateway transmit diversity in Q/V band feeder links", *IEEE Trans. Commun.*, vol. 63, no. 3, pp. 916–926, Mar. 2015 (cit. on pp. 7, 33, 34, 86).

[17] C. Riva, C. Capsoni, L. Luini, M. Luccini, R. Nebuloni, and A. Martellucci, "The challenge of using the W band in satellite communication", *Int. J. Satell. Commun. Netw.*, vol. 32, no. 3, pp. 187–200, May 2014 (cit. on pp. 7, 33, 34).

[18] A. Mody and E. Gonzalez, "An operator's view: The medium-term feasibility of an optical feeder link for VHTS", in *Proc. IEEE International Conference on Space Optical Systems and Applications (ICSOS'17)*, Nov. 2017, pp. 278–285 (cit. on p. 7).

[19] G. Foschini and M. Gans, "On limits of wireless communications in a fading environment when using multiple antennas", *Wireless Personal Communications*, vol. 6, no. 3, pp. 311–335, Mar. 1998 (cit. on p. 8).

[20] E. Telatar, "Capacity of multi-antenna Gaussian channels", *Eur. Trans. Telecommun.*, vol. 10, no. 6, pp. 585–595, Nov. 1999 (cit. on p. 8).

[21] F. Boccardi, B. Clerckx, A. Ghosh, E. Hardouin, G. Jöngren, K. Kusume, E. Onggosanusi, and Y. Tang, "Multiple-antenna techniques in LTE-advanced", *IEEE Commun. Mag.*, vol. 50, no. 3, pp. 114–121, Mar. 2012 (cit. on p. 8).

[22] P. Zhang, J. Chen, X. Yang, N. Ma, and Z. Zhang, "Recent research on massive MIMO propagation channels: A survey", *IEEE Commun. Mag.*, vol. 56, no. 12, pp. 22–29, Dec. 2018 (cit. on p. 8).

[23] P. F. Driessen and G. J. Foschini, "On the capacity formula for multiple input-multiple output wireless channels: A geometric interpretation", *IEEE Trans. Commun.*, vol. 47, no. 2, pp. 173–176, Feb. 1999 (cit. on p. 8).

[24] A. A. Hutter, F. Platbrood, and J. Ayadi, "Analysis of MIMO capacity gains for indoor propagation channels with LOS component", in *Proc. 13th IEEE International Symposium on Personal, Indoor and Mobile Radio Communications (PIMRC'2002)*, vol. 3, Sep. 2002, pp. 1337–1341 (cit. on p. 9).

[25] T. Haustein and U. Kruger, "Smart geometrical antenna design exploiting the LOS component to enhance a MIMO system based on Rayleigh-fading in indoor scenarios", in *Proc. 14th IEEE International Symposium on Personal, Indoor and Mobile Radio Communications (PIMRC'2003)*, vol. 2, Sep. 2003, pp. 1144–1148 (cit. on p. 9).

[26] A. K. M. Chouayakh and B. Lankl, "On the boundaries of the MIMO-channel-capacity with a focus on line-of-sight-connections", *Facta Universitatis, Ser.: Elec. Energ.*, vol. 17, pp. 185–197, Aug. 2004 (cit. on p. 9).

[27] D. Gesbert, H. Bolcskei, D. A. Gore, and A. J. Paulraj, "Outdoor MIMO wireless channels: Models and performance prediction", *IEEE Trans. Commun.*, vol. 50, no. 12, pp. 1926–1934, Dec. 2002 (cit. on p. 9).

[28] I. Sarris and A. R. Nix, "A line-of-sight optimised MIMO architecture for outdoor environments", in *Proc. IEEE Vehicular Technology Conference (VTC'06)*, Sep. 2006, pp. 1–5 (cit. on p. 9).

[29] F. Bohagen, P. Orten, and G. E. Oien, "Design of optimal high-rank line-of-sight MIMO channels", *IEEE Trans. Wireless Commun.*, vol. 6, no. 4, pp. 1420–1425, Apr. 2007 (cit. on p. 9).

[30] I. Sarris and A. R. Nix, "Design and performance assessment of high-capacity MIMO architectures in the presence of a line-of-sight component", *IEEE Trans. Veh. Technol.*, vol. 56, no. 4, pp. 2194–2202, Jul. 2007 (cit. on p. 9).

[31] A. Knopp, M. Chouayakh, and B. Lankl, "Capacity optimization and modeling of frequency selective WLAN indoor MIMO channels based on measured data", in *Proc. 3rd IEEE International Conference on Systems, Signals and Devices (SSD'2005)*, vol. 23, Mar. 2005, pp. 1–6 (cit. on p. 9).

[32] J.-S. Jiang and M. A. Ingram, "Spherical-wave model for short-range MIMO", *IEEE Trans. Commun.*, vol. 53, no. 9, pp. 1534–1541, Sep. 2005 (cit. on p. 9).

[33] A. Knopp, R. T. Schwarz, C. A. Hofmann, M. Chouayakh, and B. Lankl, "Measurements on the impact of sparse multipath components on the LOS MIMO channel capacity", in *Proc. 4th IEEE International Symposium on Wireless Communication Systems (ISWCS'18)*, Oct. 2007, pp. 55–60 (cit. on p. 9).

[34] A. Knopp, C. A. Hofmann, M. Chouayakh, and B. Lankl, "Measurement survey on the antenna configuration impact on the spectral efficiency of MIMO radio channels: Analyzed with a focus on low-mobility, indoor line-of-sight channels", *Wireless Personal Communications*, vol. 52, no. 1, p. 165, May 2008 (cit. on p. 9).

[35] C. A. Hofmann, D. Ogermann, and B. Lankl, "Measurement results for the comparison of multiple and single polarized MIMO channels in LOS, NLOS, indoor and outdoor scenarios", in *Proc. International ITG/IEEE Workshop on Smart Antennas (WSA'13)*, Mar. 2013, pp. 1–8 (cit. on p. 9).

[36] F. Bohagen, P. Orten, and G. E. Oien, "On spherical vs. plane wave modeling of line-of-sight MIMO channels", *IEEE Trans. Commun.*, vol. 57, no. 3, pp. 841–849, Mar. 2009 (cit. on p. 9).

[37] X. Song, T. Hälsig, D. Cvetkovski, W. Rave, B. Lankl, E. Grass, and G. Fettweis, "Design and experimental evaluation of equalization algorithms for line-of-sight spatial multiplexing at 60 GHz", *IEEE J. Select. Areas Commun.*, vol. 36, no. 11, pp. 2570–2580, Nov. 2018 (cit. on p. 9).

[38] R. T. Schwarz, A. Knopp, D. Ogermann, C. A. Hofmann, and B. Lankl, "Optimum-capacity MIMO satellite link for fixed and mobile services", in *Proc. International ITG/IEEE Workshop on Smart Antennas (WSA'08)*, Feb. 2008, pp. 209–216 (cit. on pp. 9–12, 22, 56, 62).

[39] A. Knopp, R. T. Schwarz, D. Ogermann, C. A. Hofmann, and B. Lankl, "Satellite system design examples for maximum MIMO spectral efficiency in LOS channels", in *Proc. IEEE Global Communications Conference (GLOBECOM'08)*, Nov. 2008, pp. 2890–2895 (cit. on pp. 9, 11, 12).

[40] C. Hofmann, R. T. Schwarz, and A. Knopp, "SOTM measurements for the characterization of the wideband mobile satellite channel at Ku-band", in *Proc. IEEE 10th International ITG Conference on Systems, Communications and Coding (SCC'16)*, Feb. 2015, pp. 1–8 (cit. on p. 9).

[41] V. Dantona, R. T. Schwarz, A. Knopp, and B. Lankl, "Uniform circular arrays: The key to optimum channel capacity in mobile MIMO satellite links", in *Proc. IEEE 4th Advanced Satellite Mobile Systems Conference (ASMS'10)*, Sep. 2010, pp. 421–428 (cit. on p. 10).

[42] R. T. Schwarz, A. Knopp, D. Ogermann, C. A. Hofmann, and B. Lankl, "On the prospects of MIMO SatCom systems: The tradeoff between capacity and practical effort", in *Proc. IEEE 6th International Multi-Conference on Systems, Signals and Devices (SSD'09)*, Mar. 2009, pp. 3–8 (cit. on pp. 11, 63).

[43] R. T. Schwarz, A. Knopp, and B. Lankl, "The channel capacity of MIMO satellite links in a fading environment: A probabilistic analysis", in *Proc. IEEE International Workshop on Satellite and Space Communications (IWSSC'09)*, Sep. 2009, pp. 78–82 (cit. on p. 11).

[44] A. Knopp, R. T. Schwarz, and B. Lankl, "On the capacity degradation in broadband MIMO satellite downlinks with atmospheric impairments", in *Proc. IEEE International Conference on Communications (ICC'10)*, May 2010, pp. 1–6 (cit. on p. 11).

[45] K. U. Storek, C. A. Hofmann, and A. Knopp, "Measurements of phase fluctuations for reliable MIMO space communications", in *Proc. IEEE Asia Pacific Conference on Wireless and Mobile (APWiMob'15)*, Aug. 2015, pp. 157–162 (cit. on p. 11).

[46] ——, "Interferometer for measurements of the MIMO satellite channel at Ku-band", in *Proc. IEEE 82nd Vehicular Technology Conference (VTC'15)*, Sep. 2015, pp. 1–5 (cit. on p. 11).

[47] ——, "Impact of the atmosphere on the signal phase and the channel capacity in EHF MIMO satellite links", in *Proc. IEEE Global Communications Conference (GLOBECOM'15)*, Dec. 2015, pp. 1–7 (cit. on p. 11).

[48] R. T. Schwarz, A. Knopp, and B. Lankl, "Performance of an SC-FDE SatCom system in block-time-invariant orthogonal MIMO channels", in *Proc. IEEE Global Communications Conference (GLOBECOM'11)*, Dec. 2011, pp. 1–6 (cit. on p. 11).

[49] ——, "SC-FDE V-BLAST system concept for MIMO over satellite with antenna misalignment", in *Proc. IEEE 9th International Multi-Conference on Systems, Signals and Devices (SSD'12)*, Mar. 2012, pp. 1–8 (cit. on p. 11).

[50] V. Dantona, T. Delamotte, G. Bauch, and B. Lankl, "Impact of nonlinear power amplifiers on the performance of precoded MIMO satellite systems", in *Proc. IEEE First AESS European Conference on Satellite Telecommunications (ESTEL'12)*, Oct. 2012, pp. 1–7 (cit. on p. 11).

[51] T. Delamotte, G. Bauch, V. Dantona, and B. Lankl, "Transmit precoding for MIMO-BICM-ID satellite systems with nonlinear power amplifiers", in *Proc. International ITG/IEEE Workshop on Smart Antennas (WSA'13)*, Mar. 2013, pp. 1–8 (cit. on p. 11).

[52] C. Hofmann, K. U. Storek, R. T. Schwarz, and A. Knopp, "Spatial MIMO over satellite: A proof of concept", in *Proc. IEEE International Conference on Communications (ICC'16)*, May 2016, pp. 1–6 (cit. on pp. 11, 53).

[53] B. Ramamurthy, R. T. Schwarz, W. G. Cowley, G. Bolding, and A. Knopp, "Passive channel orthogonality measurement technique for MIMO SATCOM", in *Proc. IEEE Military Communications Conference (MILCOM'18)*, Oct. 2018, pp. 1–6 (cit. on p. 11).

[54] A. Knopp, R. T. Schwarz, and B. Lankl, "Secure MIMO SATCOM transmission", in *Proc. IEEE Military Communications Conference (MILCOM'13)*, Nov. 2013, pp. 284–288 (cit. on p. 11).

[55] B. Ramamurthy, W. G. Cowley, and G. Bolding, "MIMO applicability to UHF SATCOM", in *Proc. IEEE Global Communications Conference (GLOBECOM '16)*, Dec. 2016, pp. 1–7 (cit. on p. 11).

[56] C. A. Hofmann, R. T. Schwarz, and A. Knopp, "Multisatellite UHF MIMO channel measurements", *IEEE Antennas Wireless Propagat. Lett.*, vol. 16, pp. 2481–2484, Jul. 2017 (cit. on p. 12).

[57] K. Storek and A. Knopp, "Fair user grouping for multibeam satellites with MU-MIMO precoding", in *Proc. IEEE Global Communications Conference (GLOBECOM'17)*, Dec. 2017, pp. 1–7 (cit. on pp. 12, 14).

[58] P. D. Arapoglou, K. Liolis, M. Bertinelli, A. Panagopoulos, P. Cottis, and R. D. Gaudenzi, "MIMO over satellite: A review", *IEEE Commun. Surveys Tuts.*, vol. 13, no. 1, pp. 27–51, 2011 (cit. on p. 13).

[59] M. A. Diaz, N. Courville, C. Mosquera, G. Liva, and G. E. Corazza, "Non-linear interference mitigation for broadband multimedia satellite systems", in *Proc. IEEE International Workshop on Satellite and Space Communications (IWSSC'07)*, Sep. 2007, pp. 61–65 (cit. on p. 14).

[60] M. Poggioni, M. Berioli, and P. Banelli, "BER performance of multibeam satellite systems with Tomlinson-Harashima precoding", in *Proc. IEEE International Conference on Communications (ICC'09)*, Jun. 2009, pp. 1–6 (cit. on p. 14).

[61] G. Gallinaro, G. Caire, M. Debbah, L. Cottatellucci, R. Mueller, and M. Neri, "Perspectives of adopting interference mitigation techniques in the context of broadband multimedia satellite systems", in *Proc. AIAA 23rd International Communications Satellite Systems Conference (ICSSC'05)*, Sep. 2005 (cit. on p. 14).

[62] L. Cottatellucci, M. Debbah, G. Gallinaro, R. Mueller, M. Neri, and R. Rinaldo, "Interference mitigation techniques for broadband satellite systems", in *Proc. AIAA 24th International Communications Satellite Systems Conference (ICSSC'06)*, Jun. 2006 (cit. on p. 14).

[63] S. Chatzinotas, G. Zheng, and B. Ottersten, "Joint precoding with flexible power constraints in multibeam satellite systems", in *Proc. IEEE Global Communications Conference (GLOBECOM'11)*, Dec. 2011, pp. 1–5 (cit. on p. 14).

[64] B. Devillers, A. Pérez-Neira, and C. Mosquera, "Joint linear precoding and beamforming for the forward link of multi-beam broadband satellite systems", in *Proc. IEEE Global Communications Conference (GLOBECOM'11)*, Dec. 2011, pp. 1–6 (cit. on p. 14).

[65] B. Devillers and A. Pérez-Neira, "Advanced interference mitigation techniques for the forward link of multi-beam broadband satellite systems", in *Proc. IEEE 45th Asilomar Conference on Signals, Systems and Computers (ASILOMAR'11)*, Nov. 2011, pp. 1810–1814 (cit. on p. 14).

[66] G. Zheng, S. Chatzinotas, and B. Ottersten, "Multi-gateway cooperation in multibeam satellite systems", in *Proc. IEEE International Symposium on Personal, Indoor and Mobile Radio Communications (PIMRC'12)*, Sep. 2012, pp. 1360–1364 (cit. on p. 14).

[67] V. Joroughi, M. Á. Vázquez, and A. I. Pérez-Neira, "Precoding in multigateway multibeam satellite systems", *IEEE Trans. Wireless Commun.*, vol. 15, no. 7, pp. 4944–4956, Jul. 2016 (cit. on p. 14).

[68] C. Mosquera, R. López-Valcarce, T. Ramírez, and V. Joroughi, "Distributed precoding systems in multi-gateway multibeam satellites: Regularization and coarse beamforming", *IEEE Trans. Wireless Commun.*, vol. 17, no. 10, pp. 6389–6403, Oct. 2018 (cit. on p. 14).

[69] G. Taricco, "Linear precoding methods for multi-beam broadband satellite systems", in *Proc. 20th European Wireless Conference (EW'14)*, May 2014, pp. 1–6 (cit. on p. 14).

[70] P.-D. Arapoglou, A. Ginesi, S. Cioni, S. Erl, F. Clazzer, S. Andrenacci, and A. Vanelli-Coralli, "DVB-S2X-enabled precoding for high throughput satellite systems", *Int. J. Satell. Commun. Netw.*, vol. 34, no. 3, pp. 439–455, Jun. 2016 (cit. on pp. 14, 25).

[71] D. Christopoulos, S. Chatzinotas, and B. Ottersten, "Multicast multigroup precoding and user scheduling for frame-based satellite communications", *IEEE Trans. Wireless Commun.*, vol. 14, no. 9, pp. 4695–4707, Sep. 2015 (cit. on p. 14).

[72] V. Joroughi, M. Á. Vázquez, and A. I. Pérez-Neira, "Generalized multicast multibeam precoding for satellite communications", *IEEE Trans. Wireless Commun.*, vol. 16, no. 2, pp. 952–966, Feb. 2017 (cit. on p. 14).

[73] P. R. King, *Modelling and measurement of the land mobile satellite MIMO radio propagation channel*, 2007 (cit. on p. 15).

[74] K. P. Liolis, J. Gomez-Vilardebo, E. Casini, and A. I. Perez-Neira, "Statistical modeling of dual-polarized MIMO land mobile satellite channels", *IEEE Trans. Commun.*, vol. 58, no. 11, pp. 3077–3083, Nov. 2010 (cit. on p. 15).

[75] P. Petropoulou, E. T. Michailidis, A. D. Panagopoulos, and A. G. Kanatas, "Radio propagation channel measurements for multi-antenna satellite communication systems: A survey", *IEEE Antennas Propagat. Mag.*, vol. 56, no. 6, pp. 102–122, Dec. 2014 (cit. on p. 15).

[76] V. Nikolaidis, N. Moraitis, P. S. Bithas, and A. G. Kanatas, "Multiple scattering modeling for dual-polarized MIMO land mobile satellite channels", *IEEE Trans. Antennas Propagat.*, vol. 66, no. 10, pp. 5657–5661, Oct. 2018 (cit. on p. 15).

[77] M. Sellathurai, P. Guinand, and J. Lodge, "Space-time coding in mobile satellite communications using dual-polarized channels", *IEEE Trans. Veh. Technol.*, vol. 55, no. 1, pp. 188–199, Jan. 2006 (cit. on p. 15).

[78] A. Perez-Neira, C. Ibars, J. Serra, A. del Coso, J. Gomez, and M. Caus, "MIMO applicability to satellite networks", in *Proc. IEEE 13th Signal Processing for Space Communications Workshop (SPSC'08)*, Oct. 2008, pp. 1–9 (cit. on p. 15).

[79] P.-D. Arapoglou, M. Zamkotsian, and P. Cottis, "Dual polarization MIMO in LMS broadcasting systems: Possible benefits and challenges", *Int. J. Satell. Commun. Netw.*, vol. 29, no. 4, pp. 349–366, 2011 (cit. on p. 15).

[80] A. Gharanjik, B. S. M. R. Rao, P. D. Arapoglou, and B. Ottersten, "Gateway switching in Q/V band satellite feeder links", *IEEE Commun. Lett.*, vol. 17, no. 7, pp. 1384–1387, Jul. 2013 (cit. on pp. 15, 72).

[81] T. Delamotte, R. T. Schwarz, K. U. Storek, and A. Knopp, "MIMO feeder links for high throughput satellites", in *Proc. International ITG/IEEE Workshop on Smart Antennas (WSA'18)*, Invited paper, Mar. 2018, pp. 1–8 (cit. on p. 17).

[82] T. Delamotte and A. Knopp, "Outage analysis of a MIMO-based smart gateway architecture", in *Proc. IEEE International Conference on Communications (ICC'18)*, May 2018, pp. 1–6 (cit. on p. 17).

[83] T. Delamotte and A. Knopp, "Smart diversity through MIMO satellite Q/V-band feeder links", *IEEE Trans. Aerosp. Electron. Syst.*, vol. 56, no. 1, pp. 285–300, Feb. 2020 (cit. on p. 17).

[84] R. T. Schwarz, T. Delamotte, K. Storek, and A. Knopp, "MIMO applications for multibeam satellites", *IEEE Trans. Broadcast.*, vol. 65, no. 4, pp. 664–681, Dec. 2019 (cit. on pp. 17, 21, 52, 67).

[85] M. Á. Vázquez, A. Pérez-Neira, D. Christopoulos, S. Chatzinotas, B. Ottersten, P. D. Arapoglou, A. Ginesi, and G. Tarocco, "Precoding in multibeam satellite communications: Present and future challenges", *IEEE Wireless Commun. Mag.*, vol. 23, no. 6, pp. 88–95, Dec. 2016 (cit. on p. 21).

[86] K. Y. Lau, G. F. Lutes, and R. L. Tjoelker, "Ultra-stable RF-over-fiber transport in NASA antennas, phased arrays and radars", *J. Lightwave Technol.*, vol. 32, no. 20, pp. 3440–3451, Oct. 2014 (cit. on p. 22).

[87] G. P. Martin, K. Minear, B. Geldzahler, and J. Soloff, "Large reflector uplink arraying", in *Proc. 10th International Conference on Space Operations (SpaceOps'10)*, Apr. 2010, pp. 1–52 (cit. on p. 23).

[88] F. Davarian, "Uplink arraying for solar system radar and radio science", *Proc. IEEE*, vol. 99, no. 5, pp. 783–793, May 2011 (cit. on p. 23).

[89] B. Geldzahler, C. Bershad, R. Brown, R. Hoblitzell, J. Kiriazes, B. Ledford, M. Miller, G. Woods, T. Cornish, L. D'Addario, F. Davarian, D. Lee, D. Morabito, P. Tsao, J. Soloff, K. Church, P. Deffenbaugh, K. Abernethy, W. Anderson, J. Collier, and G. Wellen, "A phased array of widely separated antennas for space communication and planetary radar", in *Proc. Advanced Maui Optical and Space Surveillance Technologies Conference (AMOS'17)*, Sep. 2017, pp. 1–19 (cit. on pp. 23, 52, 53).

[90] R. Roberts, P. Booth, G. Fox, S. Stirland, and M. Simeoni, "Q/V-band feed system development", in *Proc. IEEE 10th European Conference on Antennas and Propagation (EUCAP'16)*, Apr. 2016, pp. 1–5 (cit. on p. 24).

[91] V. Sulli, D. Giancristofaro, F. Santucci, M. Faccio, and G. Marini, "Design of digital satellite processors: From communications link performance to hardware complexity", *IEEE J. Select. Areas Commun.*, vol. 36, no. 2, pp. 338–350, Feb. 2018 (cit. on p. 25).

[92] B. Onillon, B. Benazet, and O. Llopis, "Advanced microwave optical links for LO distribution in satellite payloads", in *Proc. International Topical Meeting on Microwave Photonics (MWP'06)*, Oct. 2006, pp. 1–4 (cit. on p. 25).

[93] A. Hofmann, R. Glein, L. Frank, R. Wansch, and A. Heuberger, "Reconfigurable on-board processing for flexible satellite communication systems using FPGAs", in *Proc. IEEE Topical Workshop on Internet of Space (TWIOS'17)*, Jan. 2017, pp. 1–4 (cit. on p. 25).

[94] A. I. Perez-Neira, M. A. Vazquez, S. Maleki, M. R. B. Shankar, and S. Chatzinotas, "Signal processing for high throughput satellite systems: Challenges in new interference-limited scenarios", Feb. 2018. arXiv: 1802.03958 [cs.IT] (cit. on p. 26).

[95] E. Soop, *Handbook of geostationary orbits*, ser. Space Technology Library. Kluwer Academic Publishers, 1994 (cit. on pp. 26, 29).

[96] *Propagation data and prediction methods required for the design of Earth-space telecommunication systems*, ITU-R recommendation P.618-13, Geneva, Switzerland, 2017 (cit. on pp. 33, 34, 41, 70).

[97] G. A. Siles, J. M. Riera, and P. García-Del-Pino, "Atmospheric attenuation in wireless communication systems at millimeter and THz frequencies [Wireless Corner]", *IEEE Antennas Propagat. Mag.*, vol. 57, no. 1, pp. 48–61, Feb. 2015 (cit. on p. 33).

[98] *Attenuation by atmospheric gases*, ITU-R recommendation P.676-11, Geneva, Switzerland, 2016 (cit. on p. 33).

[99] K. Al-Ansafi, P. Garcia, J. M. Riera, and A. Benarroch, "One-year cloud attenuation results at 50 GHz", *Electronics Letters*, vol. 39, no. 1, pp. 136–137, Jan. 2003 (cit. on p. 34).

[100] *Attenuation due to clouds and fog*, ITU-R recommendation P.840-7, Geneva, Switzerland, 2017 (cit. on p. 34).

[101] P. Garcia-del-Pino, J. M. Riera, and A. Benarroch, "Fade slope statistics on a slant path at 50 GHz", *IEEE Antennas Wireless Propagat. Lett.*, vol. 9, pp. 1026–1028, Oct. 2010 (cit. on p. 34).

[102] E. Matricciani, "A relationship between phase delay and attenuation due to rain and its applications to satellite and deep-space tracking", *IEEE Trans. Antennas Propagat.*, vol. 57, no. 11, pp. 3602–3611, Nov. 2009 (cit. on p. 34).

[103] V. Fabbro, N. Jeannin, K. Djafri, J. Lemorton, and D. Vanhoenacker-Janvier, "Scintillation modelling in troposphere using multiple phase screen", *Space communications*, vol. 22, no. 2-4, pp. 51–57, Apr. 2013 (cit. on p. 34).

[104] A. D. Wheelon, *Electromagnetic Scintillation: Volume 2, Weak Scattering*. Cambridge University Press, 2003 (cit. on p. 35).

[105] J. Haddon and E. Vilar, "Scattering induced microwave scintillations from clear air and rain on earth space paths and the influence of antenna aperture", *IEEE Trans. Antennas Propagat.*, vol. 34, no. 5, pp. 646–657, May 1986 (cit. on p. 35).

[106] I. E. Otung, "Prediction of tropospheric amplitude scintillation on a satellite link", *IEEE Trans. Antennas Propagat.*, vol. 44, no. 12, pp. 1600–1608, Dec. 1996 (cit. on p. 35).

[107] C. E. Mayer, B. E. Jaeger, R. K. Crane, and X. Wang, "Ka-band scintillations: Measurements and model predictions", *Proc. IEEE*, vol. 85, no. 6, pp. 936–945, Jun. 1997 (cit. on p. 35).

[108] M. M. J. L. V. D. Kamp, C. Riva, J. K. Tervonen, and E. T. Salonen, "Frequency dependence of amplitude scintillation", *IEEE Trans. Antennas Propagat.*, vol. 47, no. 1, pp. 77–85, Jan. 1999 (cit. on p. 35).

[109] I. E. Otung and A. Savvaris, "Observed frequency scaling of amplitude scintillation at 20, 40, and 50 GHz", *IEEE Trans. Antennas Propagat.*, vol. 51, no. 12, pp. 3259–3267, Dec. 2003 (cit. on p. 35).

[110] P. Garcia-del-Pino, J. M. Riera, and A. Benarroch, "Tropospheric scintillation with concurrent rain attenuation at 50 GHz in Madrid", *IEEE Trans. Antennas Propagat.*, vol. 60, no. 3, pp. 1578–1583, Mar. 2012 (cit. on p. 35).

[111] M. J. Zemba, J. R. Morse, and J. A. Nessel, "Ka-band atmospheric phase stability measurements in Goldstone, CA; White Sands, NM; and Guam", in *Proc. IEEE 8th European Conference on Antennas and Propagation (EuCAP'14)*, Apr. 2014, pp. 503–506 (cit. on p. 35).

[112] A. M. Marziani, C. Riva, F. Consalvi, E. R. Restuccia, and F. S. Marzano, "Clear-air scintillation analysis of Q-band alphasat link at Spino d'Adda using radiosounding data", in *Proc. IEEE 11th European Conference on Antennas and Propagation (EUCAP'17)*, Mar. 2017, pp. 15–19 (cit. on p. 35).

[113] A. E. E. Rogers, A. T. Moffet, D. C. Backer, and J. M. Moran, "Coherence limits in VLBI observations at 3-millimeter wavelength", *Radio Science*, vol. 19, no. 06, pp. 1552–1560, Nov. 1984 (cit. on p. 35).

[114] J. Strohbehn, "Line-of-sight wave propagation through the turbulent atmosphere", *Proc. IEEE*, vol. 56, no. 8, pp. 1301–1318, Aug. 1968 (cit. on p. 35).

[115] R. E. Collin and F. J. Zucker, *Antenna Theory, Part 1*. McGraw-Hill, 1969 (cit. on p. 36).

[116] A. F. Sciambi, "The effect of the aperture illumination on the circular aperture antenna pattern characteristics", *Microwave J.*, vol. 8, pp. 79–84, Aug. 1965 (cit. on p. 36).

[117] K. Spies and E. Haakinson, *Calculation of geostationary satellite footprints for certain idealized antennas*, ser. NTIA report. U.S. Dept. of Commerce, National Telecommunications and Information Administration, 1980 (cit. on pp. 37, 38).

[118] A. Rudge, *The Handbook of Antenna Design*, ser. Electromagnetics and Radar Series v. 1. P. Peregrinus, 1982 (cit. on p. 37).

[119] S. K. Rao, "Design and analysis of multiple-beam reflector antennas", *IEEE Antennas Propagat. Mag.*, vol. 41, no. 4, pp. 53–59, Aug. 1999 (cit. on p. 37).

[120] E. K. Pfeiffer, T. Ernst, and A. Ihle, "Highly stable lightweight antennas for Ka/Q/V-band and other advanced telecom structure concepts", in *Proc. IEEE 3rd European Conference on Antennas and Propagation (EUCAP'09)*, Mar. 2009, pp. 745–749 (cit. on p. 38).

[121] European Telecommunications Standards Institute, *Digital Video Broadcasting (DVB); Second generation framing structure, channel coding and modulation system for Broadcasting, Interactive Services, News Gathering and other broadband satellite applications; Part 1: DVB-S2*, 2014 (cit. on p. 40).

[122] J. Proakis and S. M., *Digital Communications*. McGraw-Hill Education, 2008 (cit. on p. 40).

[123] E. Biglieri, J. Proakis, and S. Shamai, "Fading channels: Information-theoretic and communications aspects", *IEEE Trans. Inform. Theory*, vol. 44, no. 6, pp. 2619–2692, Oct. 1998 (cit. on p. 44).

[124] J. Tronc, P. Angeletti, N. Song, M. Haardt, J. Arendt, and G. Gallinaro, "Overview and comparison of on-ground and on-board beamforming techniques in mobile satellite service applications", *Int. J. Satell. Commun. Netw.*, vol. 32, no. 4, pp. 291–308, Oct. 2013 (cit. on p. 52).

[125] P. Angeletti, N. Alagha, and S. D'Addio, "Hybrid space/ground beamforming techniques for satellite telecommunications", in *Proc. 32nd ESA Antenna Workshop on Antennas for Space Applications*, vol. 21, Jan. 2010 (cit. on p. 53).

[126] R. R. Alvarez, A. A. Sanchez, E. B. Diaz, F. J. M. Carrillo, R. M. Ruano, and L. E. Tejero, "HILINK. High rate, flexible, command and monitoring equipment for digital telecom payloads", in *Proc. 4th ESA Workshop on Advanced Flexible Telecom Payloads*, Mar. 2019, pp. 1–5 (cit. on p. 53).

[127] A. Wiesel, Y. C. Eldar, and S. Shamai, "Zero-forcing precoding and generalized inverses", *IEEE Trans. Signal Processing*, vol. 56, no. 9, pp. 4409–4418, Sep. 2008 (cit. on p. 54).

[128] D. P. Palomar, "Unified framework for linear MIMO transceivers with shaping constraints", *IEEE Commun. Lett.*, vol. 8, no. 12, pp. 697–699, Dec. 2004 (cit. on pp. 56, 101).

[129] D. P. Palomar, J. M. Cioffi, and M. A. Lagunas, "Joint Tx-Rx beamforming design for multicarrier MIMO channels: a unified framework for convex optimization", *IEEE Trans. Signal Processing*, vol. 51, no. 9, pp. 2381–2401, Sep. 2003 (cit. on pp. 56, 101).

[130] E. Bjornson, E. Jorswieck, and B. Ottersten, "Impact of spatial correlation and precoding design in OSTBC MIMO systems", *IEEE Trans. Wireless Commun.*, vol. 9, no. 11, pp. 3578–3589, Nov. 2010 (cit. on p. 59).

[131] *Characteristics of precipitation for propagation modelling*, ITU-R recommendation P.837-7, Geneva, Switzerland, 2017 (cit. on p. 70).

[132] *Differential rain attenuation*, ITU-R recommendation P.1815-1, Geneva, Switzerland, 2009 (cit. on pp. 71, 77).

[133] M. Fernandez and S. Williams, "Closed-form expression for the Poisson-binomial probability density function", *IEEE Trans. Aerosp. Electron. Syst.*, vol. 46, no. 2, pp. 803–817, Apr. 2010 (cit. on pp. 82, 103).

[134] T. Inukai, "An efficient SS/TDMA time slot assignment algorithm", *IEEE Trans. Commun.*, vol. 27, no. 10, pp. 1449–1455, Oct. 1979 (cit. on p. 83).

[135] M. Muhammad, G. Giambene, and T. de Cola, "Channel prediction and network coding for smart gateway diversity in terabit satellite networks", in *Proc. IEEE Global Communications Conference (GLOBECOM'14)*, Dec. 2014, pp. 3549–3554 (cit. on p. 89).